Epidermal Growth Factor Receptor Extracellular Domain Mutations in Glioblastoma Present Opportunities for Clinical Imaging and Therapeutic Development

Binder, Zev A ; Thorne, Amy Haseley ; Bakas, Spyridon ; et al ; Weller, Michael

Abstract: We explored the clinical and pathological impact of epidermal growth factor receptor (EGFR) extracellular domain missense mutations. Retrospective assessment of 260 de novo glioblastoma patients revealed a significant reduction in overall survival of patients having tumors with EGFR mutations at alanine 289 (EGFR). Quantitative multi-parametric magnetic resonance imaging analyses indicated increased tumor invasion for EGFR mutants, corroborated in mice bearing intracranial tumors expressing EGFR and dependent on ERK-mediated expression of matrix metalloproteinase-1. EGFR tumor growth was attenuated with an antibody against a cryptic epitope, based on in silico simulation. The findings of this study indicate a highly invasive phenotype associated with the EGFR mutation in glioblastoma, postulating EGFR as a molecular marker for responsiveness to therapy with EGFR-targeting antibodies.

DOI: https://doi.org/10.1016/j.ccell.2018.06.006

Cancer Cell

Epidermal Growth Factor Receptor extracellular domain mutations in glioblastoma present opportunities for clinical imaging and therapeutic development

--Manuscript Draft--

Manuscript Number:	CANCER-CELL-D-17-00892R1
Full Title:	Epidermal Growth Factor Receptor extracellular domain mutations in glioblastoma present opportunities for clinical imaging and therapeutic development
Article Type:	Research Article
Keywords:	glioma; glioblastoma; GBM; EGFR; A289D/T/V; survival
Corresponding Author:	Frank B. Furnari, PhD Ludwig Institute-UCSD La Jolla, UNITED STATES
First Author:	Zev A. Binder, M.D., Ph.D.
Order of Authors:	Zev A. Binder, M.D., Ph.D.
	Amy Haseley Thorne, Ph.D.
	Spyridon Bakas, Ph.D.
	E. Paul Wileyto, Ph.D.
	Michel Bilello, M.D., Ph.D.
	Hamed Akbari, Ph.D.
	Saima Rathore, Ph.D.
	Sung Min Ha, MSE
	Logan Zhang
	Cole J. Ferguson, M.D., Ph.D.
	Sonika Dahiya, M.D.
	Wenya Linda Bi, Md, PhD
	David Reardon, MD
	Ahmed Idbaih, MD, PhD
	Joerg Felsberg, MD
	Bettina Hentschel, MS
	Michael Weller, MD
	Stephen J. Bagley, MD
	Jennifer J. D. Morrissette, Ph.D.
	Maclean P Nasrallah, MD, PhD
	Jianhui Ma, Ph.D.
	Ciro Zanca, PhD
	Laura Orellana, Ph.D.
	Andrew M. Scott, M.D.
	Christos Davatzikos, Ph.D.
	Frank B. Furnari, Ph.D.
	Donald M. O'Rourke, M.D.
Abstract:	We explored the clinical and pathological impact of EGFR extracellular domain

	missense mutations. Retrospective assessment of 260 de novo glioblastoma (GBM) patients revealed a significant reduction in overall survival of patients with EGFR mutations at alanine 289 (EGFRA289D/T/V). Quantitative multi-parametric MRI analyses indicated increased tumor invasion for EGFRA289D/T/V mutants, a finding corroborated in mice bearing intracranial tumors expressing EGFRA289V and dependent on ERK-mediated expression of matrix metalloproteinase-1 (MMP1). EGFRA289V tumor growth was attenuated with an EGFRvIII conformation-specific antibody based on a hypothesized structural convergence. Collectively, the findings of this study indicate a highly invasive and prognostic indicator for the EGFRA289V missense mutation in GBM, postulating EGFRA289V as a molecular marker for responsiveness to therapy with EGFR-targeting antibodies.
Suggested Reviewers:	Cameron Brennan, M.D. Memorial Sloan Kettering Cancer Center brennac2@mskcc.org Dr. Brennan is well-versed in GBMs and their clinical picture.
	Kristin Swanson, Ph.D. Professor, Mayo Clinic, Socttsdale, AZ swanson.kristin@mayo.edu Expert on glioma imaging
	Erik Sulman, Ph.D. Assistant Professor, MD Anderson Cancer Center epsulman@mdanderson.org Expert in GBM biology
	Olivier Gevaert, Ph.D. Assistant Professor, Stanford University ogevaert@stanford.edu Expert in glioma imaging and machine learning
	Shi-Yuan Cheng, Ph.D. Professor, Northwestern University shiyuan.cheng@northwestern.edu Expert in cancer signaling pathways
Opposed Reviewers:	Ingo Mellinghoff, M.D. Memorial Sloan Kettering Cancer Center Dr. Mellinghoff is involved in the Defeat GBM Research Collaborative, along with Dr. Furnari, Lead Contact of this submission.
	Terry Johns, Ph.D. Professor, Hudson Institute of Medical Research terry.hohns@hudson.org.au Direct competitor
	Mark Lemmon, Ph.D. Professor, Yale University mark.lemmon@yale.edu Direct competitor.
Additional Information:	
Question	**Response**
If your paper is accepted, we encourage you to publish the original, unprocessed data alongside your Cell Press paper through Mendeley Data. For more information, please refer to our detailed instructions.	I do not wish to publish my original data.

February 26, 2018

Cancer Cell
Editor-in-Chief
Dr. Li-Kuo Su
50 Hampshire St., 5th Floor
Cambridge, MA 02139

Dear Dr. Su:

Thank you for the opportunity to address the reviewers' concerns and questions. We feel that in doing so, we have strengthened the conclusions of the manuscript. A point-by-point explanation for the comments has been included. Of note, the latter half of Reviewer #2's comments addressed the radiomics portion of the manuscript. Those responses and edits, in combination with our response to Reviewer #1's second comment, have significantly strengthened the contributions of the radiomics to our work. Moreover, in response to the concerns raised by Reviewer #1, we believe these responses have validated the inclusion of the imaging data in the current manuscript.

We have also included two validation cohorts to address Reviewer #2's 1st and 2nd comments. The French cohort, from Hôpital Pitié-Salpêtrière, was obtained prior to 2009, so it fulfills the external requirement but is dated. The UPenn validation cohort was obtained from 2015-2017, so it is contemporary and a distinct cohort, but from our own institution. We feel the inclusion of these two cohorts both fully addresses the Reviewer's comments and strengthens the conclusions drawn.

There are no financial conflicts of interest or competing interests to report with this submitted manuscript. The work described has not been previously published or currently submitted elsewhere for your review. The targetability of glioblastoma missense mutations by mAb806 shown in our manuscript is now supported by a bioRxiv reference (DOI: 10.1101/009068) as the Cancer Cell submission, Orellana et al., CANCER-CELL-D-16-00999, is still under arbitration. Since this manuscript provided the structural basis for the therapeutic use of mAb806 against EGFR missense mutations, and here we demonstrate the feasibility of this approach *in vivo*, both manuscripts do not overlap in any way but are complementary pieces. We want to reaffirm that our manuscript and Orellana et al are completely separate and independent manuscripts. Thank you in advance for considering this submission, we hope you will find our work consistent with the aim and scope of *Cancer Cell*.

If we can provide any further information, please do not hesitate to contact us. We look forward to hearing from you soon.

Sincerely,

Donald M. O'Rourke, M.D
Associate Professor
Department of Neurosurgery
Abramson Cancer Center
Perelman School of Medicine
University of Pennsylvania
Philadelphia, PA 19104
donald.orourke@uphs.upenn.edu

Frank Furnari
Member and Head
Laboratory of Tumor Biology
Ludwig Institute for Cancer Research

Professor-Department of Pathology
University of California-San Diego
9500 Gilman Drive CMM-East Rm 3053
La Jolla CA 92093-0660
ffurnari@ucsd.edu

Reviewer's comments:
Reviewer #1: The authors examine the EGFR extracellular domain missense mutation at alanine 289 (EGFRA289D/T/V). They find that these mutations promote tumor invasion via ERK-mediated MMP1 expression. EGFRA289V tumor growth was attenuated with an EGFRvIII conformation-specific antibody. The authors may wish to consider the following points

1. The impact of this work would be enhanced if the authors could show that tumors that were responsive to ABT-414 in clinical trials were enriched to have the EGFR-A289 mutations. The section entitled " mAb806 is a potential therapeutic option for patients.." is perhaps optimistic in that patient data are not included. Given that there are patients who have been treated with ABT-414, testing whether the A289 mutation is predictive of response would be impactful

We agree with Reviewer #1 in that investigating the survival of EGFR A289 mutant patients on the ABT-414 trial would be very impactful. Unfortunately, the logistics involved in that sub-population analysis are prohibitive. Specifically, in the ABT-414 Stage IIb/III clinical trial, of the anticipated ~700 patients enrolled, approximately 35 patients will have an A289 mutation, based on a 5% occurrence rate. As the trial is randomized, we presume <20 patients with an A289 mutation will be receiving ABT-414. Additionally, the majority of enrolling locations do not sequence their tumors, so the identification of A289 mutant patients in the trial will be difficult, if not impossible. As an example, the University of Pennsylvania has enrolled 5 patients, of which none have had the mutation. Given the difficulty in identifying all of the mutant patients on the trial, we feel that running a sub-population analysis in the current trial is not feasible. Importantly, the clinical trial enrollment recently closed and the data have not been made available for review at this stage. We do, however, hope the conclusions in this manuscript will help inform future EGFR-targeting trials to include a sub-population analysis of the EGFR A289 mutant population.

2. The radiomics data lacks validation and is somewhat distracting, and takes away from the main message of the manuscript.

We appreciate the concerns raised by Reviewer #1 regarding the radiomics data. However, we feel that including the radiomics data is useful for ascertaining our underlying hypothesis and reasoning behind focusing on the further assessment and analysis of the A289 mutation. We also believe that the radiomics data offers an insight on imaging differences that are not apparent to standard MRI interpretation, only after advanced computational analysis. In order to better justify the use of the radiomics data and demonstrate their validity in various studies, we have included additional citations from the literature, both from our group and others (see below). In these studies, computational analysis of radiomics data has been shown to be predictive of clinical outcome and molecular characteristics. In addition, we have softened the language in the discussion associated with radiomics, emphasizing that we used the imaging findings in a hypothesis-generating manner, not a hypothesis-driven manner, on page 11. The additional references cited in the manuscript are as follows, with papers from our group listed in bold, followed by other citations that, due to length limitations on the paper, not all of them have been included:

- *H.J.Aerts. "The Potential of Radiomic-Based Phenotyping in Precision Medicine: A Review" JAMA Oncol. 2016 Dec 1;2(12):1636-1642. doi: 10.1001/jamaoncol.2016.2631.*
- ***S.Bakas, H.Akbari, J.Pisapia, M.Martinez-Lage, M.Rozycki, S.Rathore, N.Dahmane, D.M.O'Rourke, C.Davatzikos. "In vivo detection of EGFRvIII in glioblastoma via perfusion magnetic resonance imaging signature consistent with deep peritumoral infiltration: the φ index", Clin Cancer Research, 23(16):4724-4734, August 15 2017. DOI: 10.1158/1078-0432.CCR-16-1871***
- ***S.Bakas, Z.A.Binder, H.Akbari, M.Martinez-Lage, M.Rozycki, J.J.D.Morrissette, N.Dahmane, D.M.O'Rourke, C.Davatzikos. "Highly-expressed wild-type EGFR and EGFRvIII mutant glioblastomas have similar MRI signature, consistent with deep peritumoral infiltration." Neuro Oncol. 18:vi125-vi126, 2016 DOI: 10.1093/neuonc/now212.523***
- *B.M.Ellingson, E.R.Gerstner, M.Smits, R.Y.Huang, R.Colen, L.E.Abrey, D.T.Aftab, G.M.Schwab, C.Hessel, R.J.Harris, A.Chakhoyan, R.Gahrmann, W.B.Pope, K.Leu, C.Raymond, D.C.Woodworth, J.de Groot, P.Y.Wen, T.T.Batchelor, M.J.van den Bent, T.F.Cloughesy. "Diffusion MRI Phenotypes Predict Overall Survival Benefit from Anti-VEGF Monotherapy in Recurrent Glioblastoma: Converging Evidence from Phase II Trials" Clin Cancer Res. 2017 Oct 1;23(19):5745-5756. DOI: 10.1158/1078-0432.CCR-16-2844*
- *O.Gevaert, S.Echegaray, A.Khuong, C.D.Hoang, J.B.Shrager, K.C.Jensen, G.J.Berry, H.H.Guo, C.Lau, S.K.Plevritis, D.L.Rubin, S.Napel, A.N.Leung. "Predictive radiogenomics modeling of EGFR mutation status in lung cancer" Sci Rep. 2017; 7: 41674. DOI: 10.1038/srep41674*
- *B.J.Gill, D.J.Pisapia, H.R.Malone, H.Goldstein, L.Lei, A.Sonabend, J.Yun, J.Samanamud, J.S.Sims, M.Banu, A.Dovas, A.F.Teich, S.A.Sheth, G.M.McKhann, M.B.Sisti, J.N.Bruce, P.A.Sims, P.Canoll. "MRI-localized biopsies reveal subtype-specific differences in molecular and cellular composition at the margins of glioblastoma". Proc Natl Acad Sci U S A. 2014 Aug 26;111(34):12550-5. DOI: 10.1073/pnas.1405839111*
- *D.A.Gutman, L.A.D.Cooper, S.N.Hwang, C.A.Holder, J.Gao, T.D.Aurora, W.D.Dunn Jr, L.Scarpace, T.Mikkelsen, R.Jain, M.Wintermark, M.Jilwan, P.Raghavan, E.Huang, R.J.Clifford, P.Mongkolwat, V.Kleper, J.Freymann, J.Kirby, P.O.Zinn, C.S.Moreno, C.Jaffe, R.Colen, D.L.Rubin, J.Saltz, A.Flanders, D.J.Brat. "MR imaging predictors of molecular profile and survival: multi-institutional study of the TCGA glioblastoma data set" Radiology. 2013 May; 267(2): 560–569 DOI: 10.1148/radiol.13120118*
- *H.Itakura, A.S.Achrol, L.A.Mitchell, J.J.Loya, T.Liu, E.M.Westbroek, A.H.Feroze, S.Rodriguez, S.Echegaray, T.D.Azad, K.W.Yeom, S.Napel, D.L.Rubin, S.D.Chang, G.R.Harsh, O.Gevaert. "Magnetic resonance image features identify glioblastoma phenotypic subtypes with distinct molecular pathway activities" Sci Transl Med. 2015 Sep 2;7(303):303ra138. DOI: 10.1126/scitranslmed.aaa7582*
- ***L.Macyszyn, H.Akbari, J.M.Pisapia, X.Da, M.Attiah, V.Pigrish, Y.Bi, S.Pal, R.V.Davuluri, L.Roccograndi, N.Dahmane, M.Martinez-Lage, G.Biros, R.L.Wolf, M.Bilello, D.M.O'Rourke, C.Davatzikos. "Imaging patterns predict patient survival and molecular subtype in glioblastoma via machine learning techniques", Neuro Oncol. 2016 Mar; 18(3): 417–425. DOI: 10.1093/neuonc/nov127***

Additional references not included in the manuscript (due to space limitations)

- ***H.Akbari, L.Macyszyn, X.Da, M.Bilello, R.L.Wolf, M.Martinez-Lage, G.Biros, M.Alonso-Basanta, D.M.O'Rourke, C.Davatzikos. "Imaging Surrogates of Infiltration Obtained Via Multiparametric Imaging Pattern Analysis Predict Subsequent Location of Recurrence of Glioblastoma", Neurosurgery. 2016 Apr;78(4):572-80. doi: 10.1227/NEU.0000000000001202***
- *K.Chang, H.X.Bai, H.Zhou, C.Su, W.L.Bi, E.Agbodza, V.K.Kavouridis, J.T.Senders, A.Boaro, A.L.Beers, B.Zhang, A.Capellini, W.Liao, Q.Shen, X.Li, B.Xiao, J.Cryan, S.Ramkissoon, L.Ramkissoon, K.L.Ligon, P.Y.Wen, R.S.Bindra, J.H.Woo, O.Arnaout, E.Gerstner, P.J.Zhang, B.Rosen, L.Yang, R.Y.Huang, J.Kalpathy-Cramer. "Residual Convolutional Neural Network for Determination of IDH Status in Low-and High-grade Gliomas from MR Imaging" Clin Cancer Res. 2017 Nov 22. pii: clincanres.2236.2017. doi: 10.1158/1078-0432.CCR-17-2236*
- *B.M.Ellingson. "Radiogenomics and imaging phenotypes in glioblastoma: novel observations and correlation with molecular characteristics" Curr Neurol Neurosci Rep. 2015 Jan;15(1):506. DOI: 10.1007/s11910-014-0506-0*
- *O. Gevaert, L.A. Mitchell, A.S. Achrol, J. Xu, S. Echegaray, G.K. Steinberg, S.H. Cheshier, S. Napel, G. Zaharchuk, S.K. Plevritis. "Glioblastoma multiforme: exploratory radiogenomic analysis by using quantitative image features" Radiology. 2014 Oct;273(1):168-74. doi: 10.1148/radiol.14131731.*
- *A.Mahajan, A.V.Moiyadi, R.Jalali, E.Sridhar. "Radiogenomics of glioblastoma: a window into its imaging and molecular variability" **Cancer Imaging**. 2015; 15(Suppl 1): P14. DOI: 10.1186/1470-7330-15-S1-P14*
- *S.H.Patel, L.M.Poisson, D.J.Brat, Y.Zhou, L.Cooper, M.Snuderl, C.Thomas, A.M.Franceschi, B.Griffith, A.Flanders, J.G.Golfinos, A.S.Chi, R.Jain. "T2-FLAIR Mismatch, an Imaging Biomarker for IDH and 1p/19q Status in Lower Grade Gliomas: A TCGA/TCIA Project" Clin Cancer Res. 2017 Oct 15;23(20):6078-6085. DOI: 10.1158/1078-0432.CCR-17-0560.*
- ***E.S. Tykocinski, R.A. Grant, G.S.Kapoor, J. Krejza, L.Bohman, T.A.Gocke, S. Chawla, C.H. Halpern, J. Lopinto, E.R. Melhem, D.M. O'Rourke. "Use of magnetic perfusion-weighted imaging to determine epidermal growth factor receptor variant III expression in glioblastoma" Neuro Oncol. 2012 May; 14(5): 613-623. doi:10.1093/neuonc/nos073.***
- *B.Zhang, K.Chang, S.Ramkissoon, S.Tanguturi, W.L.Bi, D.A.Reardon, K.L.Ligon, B.M.Alexander, P.Y.Wen, R.Y.Huang. "Multimodal MRI features predict isocitrate dehydrogenase genotype in high-grade gliomas." Neuro Oncol. 2017 Jan;19(1):109-117. DOI: 10.1093/neuonc/now121.*

3. If the 289 mutation exerts its effects through MMP-1 mediated invasion, then knockdown of MMP-1 in EGFR-289-expressing cells should revert the cells back to baseline. This kind of data would elucidate and solidify the overall hypothesis of this manuscript.

Reviewer #1 raises a valid point regarding MMP-1 knockdown and its effect on cell invasion. Although we have demonstrated the loss of the invasive phenotype in vitro (Figure 5A-D in the manuscript), in our revised manuscript we have now included new data indicating shMMP1-mediated loss of the invasion in vivo as shown below (Figure 5G-H) and text on Page 8 stating "Finally, MMP1 knockdown in vivo nullified the invasive phenotype attributed to the EGFRA289V mutation (Figure 5G-H)."

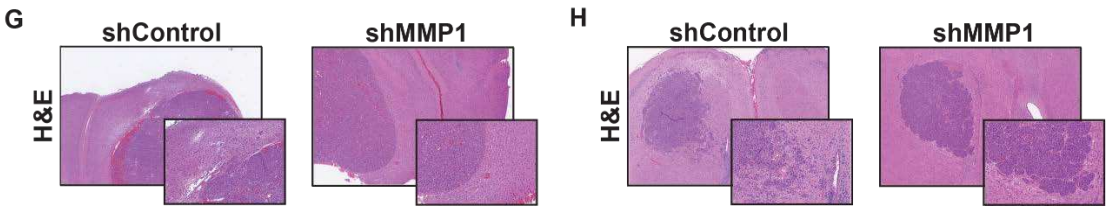

Figure 5G-H. Abrogation of invasive phenotype in vivo was obtained with knockdown of MMP1 in both U87 (G) and HK281 (H).

Reviewer #2: This study begins with investigation of 260 IDH1-wt, de novo GBM patients, looking for clinicopathologic correlates of EGFR extracellular domain (ECD) mutations. The cohort is typical, with 38% harboring EGFR amplification and ~10% with ECD point mutations including 6% with A289D/T/V mutations (A289-mt). These cases are the focus of analysis of survival as well as MRI radiomic correlative features. The main claims are that EGFR missense mutations of A289D/T/V (A289-mt) are associated with shorter median OS (6 months vs. 15 months), and increased invasion and higher proliferation based on MRI feature analysis. The authors go on to explore potential mechanisms using glioma cell lines engineered to express different ECD mutations. Finally, the authors investigate a hypothesis that A289-mt exposes an epitope targeted by the EGFRvIII-directed mAb 806 by testing the antibody in mice bearing glioma cell line orthotopic tumors +/- A289-mt.

The claim of distinct clinicopathologic features for EGFR A289-mt GBMs in patients is foundational to this study. As the authors point out, EGFR genotype is particularly heterogeneous within and across GBMs. A289 mutation commonly occurs with EGFR amplification and can co-occur with other EGFR mutations in the same tumor. The authors have previously shown that intratumoral heterogeneity of EGFRvIII mutation can itself be a strong driver of growth and invasion. Therefore one might expect that direct effects of A289-mt on growth or invasion would be modulated by other factors in human tumors--hard to pull out of a small sample set of 15 tumors. Although the finding of potential clinicopathologic correlates is intriguing, the handling of methods and statistics (particularly false discovery rate) does not allow for a clear conclusion.

There are a few specific points relevant to the human tumor analysis:

Whether EGFR amplification or mutation is prognostic becomes an important issue when considering clinical trials (including ongoing trials of EGFR inhibition in GBM). If A289-mt tumors were truly more deadly, then one might be tempted to direct patients with the mutation to trials early-on in their course of treatment. Study design would need to account for the worse prognosis of A289-mt patients in survival analysis. The current study finds median OS of 6 months in such patients, suggesting little benefit from conventional therapy. It is important to establish whether this is a real effect.

1. Figure 1 shows Kaplan-Meier analysis for 4 GBM subsets defined by specific EGFR alterations. The difference in median OS for A289-mt tumors is marginally significant, and is insignificant if correction for multiple comparisons is performed. The manuscript does not frame a specific hypothesis related to

A289-mt at the outset, so I assume that the selection of this genotype after prognostic analysis of all ECD mutations requires p-value correction. This should be addressed in the text. Claims that the data demonstrate a prognostic effect or clinical significance of A289-mt should be restated in softer language.

Because Reviewer #2's Comment 2 refers back to Comment 1, we have responded to Reviewer #2's Comments 1 and 2 together, following Comment 2.

2. The authors reference TCGA data for support, but fail to show a simple validation of a prognostic effect of A289-mt status. This would render moot the issue of p-values for their exploratory analysis in their own cohort. A simple comparison survival analysis of TCGA primary GBM cases +/- mutation at A289 can be performed on public portals. It should be included in this manuscript.

We agree with Reviewer #2 that demonstration of the survival impact of $EGFR^{A289}$ mutations in a second cohort would strengthen the conclusions and render moot the issue of p-value corrections for our initial exploratory analysis. The initial UPenn cohort contained patient tissue samples assayed at UPenn through June of 2016. We have interrogated an additional 111 patients who visited UPenn between July of 2016 and June of 2017 (not all patients had an operation during this time; some came for second opinions and brought tissue blocks from prior surgeries for sequencing). This validation cohort demonstrated a similar occurrence rate of $EGFR^{A289D/T/V}$, at 4%. Median OS for the A289D/T/V mutant population was 4 months, compared to 20 months for $EGFR^{A289}$, p-value=0.009. We have also obtained a second validation cohort from the Hôpital Pitié-Salpêtrière, similarly demonstrating a negative survival association with expression of $EGFR^{A289D/V}$, p-value=0.01. We have included both cohorts as the French cohort, while from an independent institution, was collected pre-2009 and the UPenn cohort is more modern, encompassing patients from 2015-2017. As per our biostatistician (E.P.W.), these two cohorts sufficiently address the concerns of p-value correction and validation raised here.

The resulting data has now been included in the manuscript as Figure S1B-C (shown here) and text on Page 5, stating "The EGFRA289D/T/V negative survival association was validated using two independent cohorts. An additional 111 patients from UPenn were evaluated, showing a negative survival association with presence of the EGFRA289D/T/V mutation (p=0.001, Figure S1B). A 116 patient cohort from Hôpital Pitié-Salpêtrière (Idbaih et al., 2009) demonstrated a similar negative survival association (p=0.0208, Figure S1C)."

In our efforts to secure a validation cohort, we evaluated numerous other patient cohorts, both nationally and internationally (see table below). We were unable to confirm our $EGFR^{A289D/T/V}$ survival association in these additional datasets and we believe there were several significant issues that explain these findings. Variables such as surgical approach (e.g. extent of resection), adjuvant treatments, and clinical trial availability and accrual all play a role in data discrepancies. We also found that several datasets did not provide sufficient clinical annotation to allow comparison. Specifically, the TCGA dataset had incomplete pathological data, making it difficult to parse the population and obtain a cohort similar to the UPenn group. The Chinese Glioma Gene Atlas (CGGA), while clinically annotated, demonstrated a strikingly different median OS, independent of mutational status (OS of 11 months, compared to 15 months at UPenn), in addition to having an occurrence rate of $EGFR^{A289D/T/V}$ of three times the Penn cohort (15%, compared to 5% at Penn). Washington

University had a median OS of 21 months, significantly different from the UPenn cohort. MSK-IMPACT did not differentiate between de novo and recurrent GBMs and had a median OS of 19 months. Dana Farber had a similar median overall survival to the UPenn group at 15 months and sub-group analysis of the Dana Farber data suggested a negative survival association of EGFR$^{A289D/T/V}$ missense mutations in the absence of EGFR amplification. However, this was a small sample size (AMP n=5, non-AMP n=3) and the results did not reach statistical significance. In addition, Dana Farber used different methods to determine amplification than UPenn (CISH, array CGH, or Oncopanel capture-based sequencing as opposed to our NGS-based method), which could impact the determination threshold for EGFR amplification. Similarly, each examined cohort used a different method for determining EGFR mutational status, which could result in variation in detection sensitivity.

The survival curves for all available national and international cohorts considered, independent of mutation status, are shown below. The differences in survival between cohorts demonstrates the difficulty in performing cross-cohort analyses. Surgical outcomes, standard-of-care therapy, clinical trial enrollment, and other variables all factor into patient survival. An additional possibility is that the EGFR$^{A289D/T/V}$ mutations are associated with a hidden covariate. Continued investigation, both clinically and in the lab, may lead to further insight, but this exploration falls outside the scope of the current manuscript.

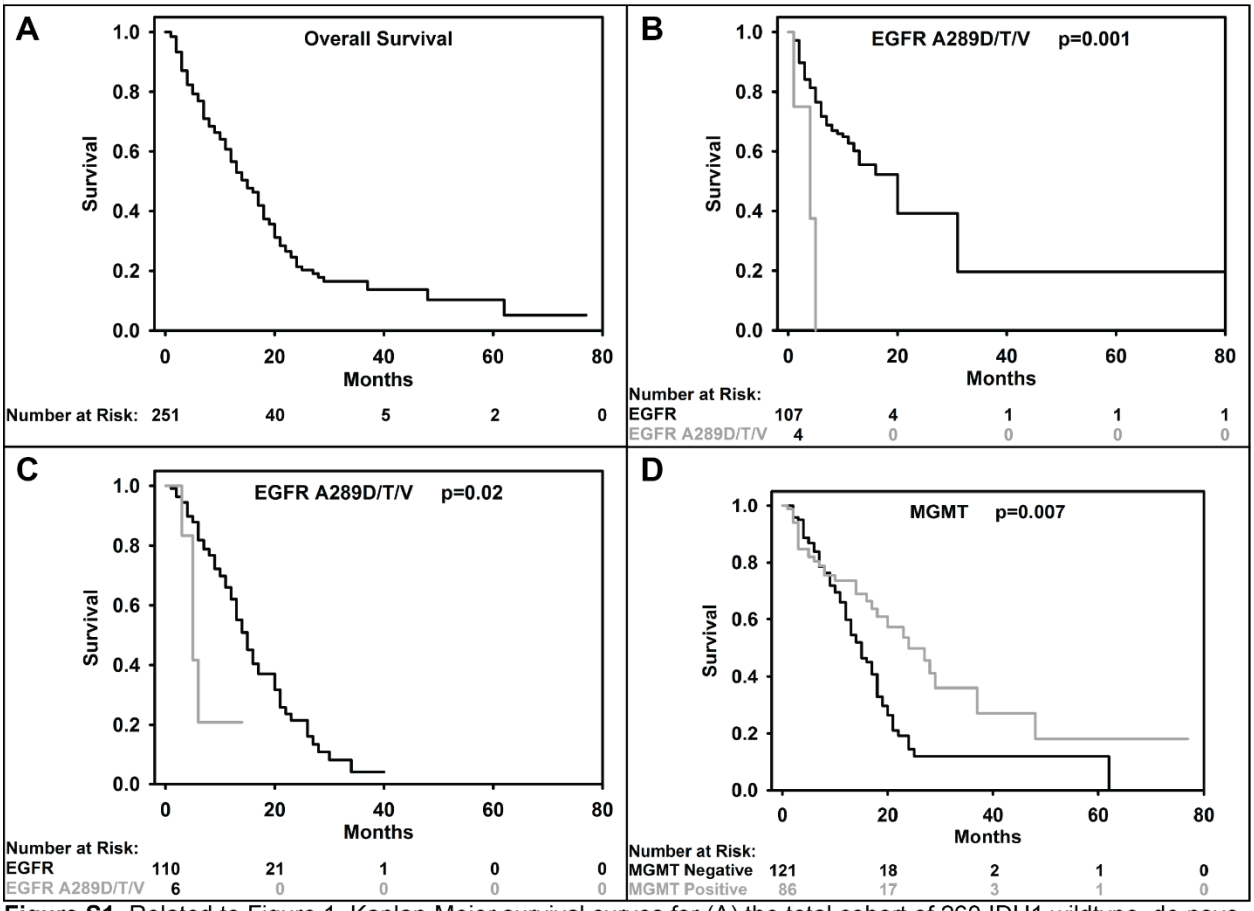

Figure S1. Related to Figure 1. Kaplan-Meier survival curves for (A) the total cohort of 260 IDH1 wildtype, de novo GBMs, (B) the validation UPenn cohort, (C) the validation French cohort, and (D) MGMT methylated versus MGMT unmethylated GBM patients.

Cohort	*Sample size*	*De novo vs recurrent distinction*	*Median OS (Months)*
UPenn Discovery	*260*	*Yes*	*15*
UPenn Validation	*111*	*Yes*	*20*
TCGA	*522*	*Mixed*	*14*
CGGA	*84*	*Yes*	*13*
Washington University	*88*	*Yes*	*21*
MSK	*210*	*No*	*19*
Dana Farber	*204*	*Yes*	*15*
GGN	*183*	*Yes*	*16*
Hôpital Pitié-Salpêtrière	*116*	*Yes*	*14*

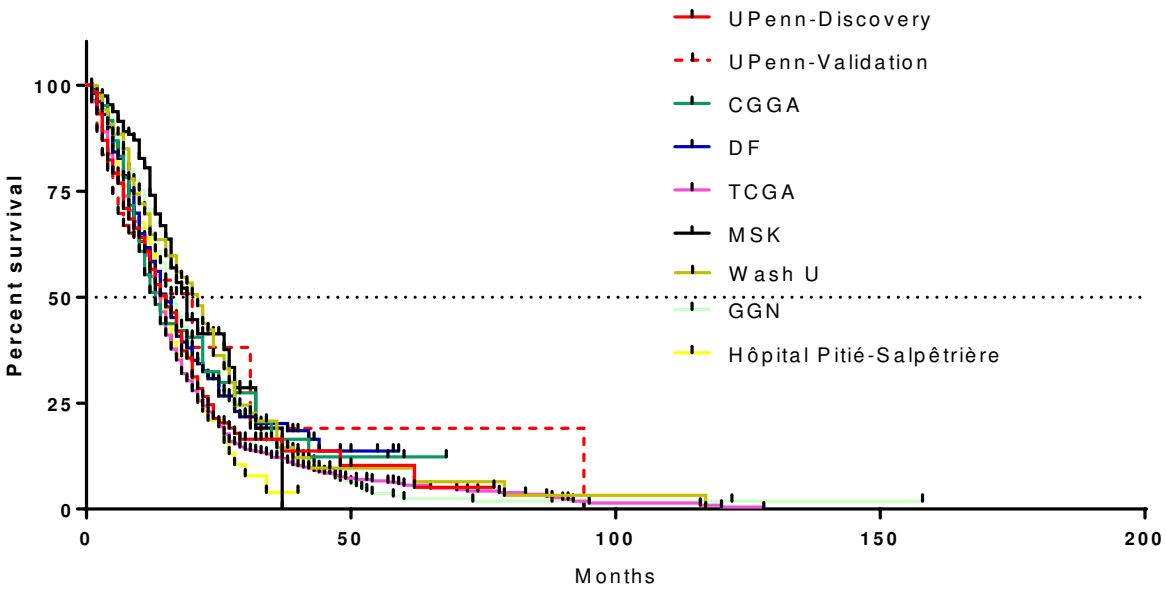

Kaplan-Meier survival curve for overall survival of all cohorts considered.

3. The methodology for selecting the 17 Quantitative Imaging Phenomic (QIP) features is not adequately described.

We appreciate the reviewer's comment on not adequately describing the methodological details of the multivariate feature selection approach we followed. In our attempt to clarify how the pruning was conducted, we have now elaborated on the selection in the Materials section of the manuscript (page 30). We highlight that the feature selection was based off of statistically significant ($p<0.05$) features. Following the suggestion of the editor, we did not include comprehensive mathematical formulation of the method we used. However, it can be found in Gaonkar and Davatzikos, 2013, as referenced in our paper.

3.1: The first step appears to be extraction of features distinguishing 3 separate ECD mutation classes from EGFR-WT. How is the latter set defined? Does EGFR-WT include EGFRvIII? If testing A289-mt, is EGFR-WT defined as wildtype at the 289 residue?

Considering this comment in addition to comment 4.2, we realize that the definition of WT EGFR for the image analyses was not clear. To avoid any potential misunderstanding or confusion, we have now explicitly defined in the Methods section (page 30) that WT EGFR "described only those tumors that had confirmed wild-type EGFR at normal expression levels, thereby excluding EGFRvIII, amplification, and mutations at A289, R108, and G598 residues."

3.2: Table S3 lists 17 QIP feature comparisons selected from the preceding analysis. If I understand correctly, the table shows only 12 unique QIP features (some are listed twice).

We understand the confusion caused by Table S3. To further clarify why there are some duplicate textual descriptions shown in the column describing the QIP "feature observation", we have now expanded the caption of Table S3 to state that "The described feature observations are the ones denoted as statistically significant (p>0.05), based on the applied multivariate approach for feature selection (Gaonkar and Davatzikos, 2013) and after selection based on radiographic interpretation. Furthermore, this table denotes the tumor sub-regions in which each of these feature observations were captured, as well as the pairs of EGFR variants that these features were found as statistically significant."

3.3: Table S3: The first feature in the table is presented as distinguishing R108-mt vs. A289-mt. Were such ECD vs. ECD discriminations part of the preceding analysis? If so, then it seems that almost no features distinguish A289-mt from other ECD mutations. This would not be surprising given the small numbers of ECD-mutant cases.

To address the reviewer's comment, we have now clarified in the Methods section (page 32) that we have also "analytically estimated the statistical significance of all extracted radiomic features distinguishing the EGFR missense mutants from WT EGFR, as well as between the EGFR mutants". Furthermore, we have now expanded Table S2, which previously included only the statistically significant QIP features distinguishing the EGFR mutations from the WT EGFR, to include the statistically significant QIP features that distinguish ***between*** *the ECD mutations assessed in our study. Table S3 focused on the features that were radiographically interpretable while Table S2 focused on features that were statistically significant.*

3.4: False discovery rate must be considerable for this exercise, given thousands of QIP features. There is no discussion of this, nor of p-value correction (whether performed or not).

We appreciate Reviewer #2's comment regarding FDR analysis (p-value correction) for our imaging component. To address and clarify this concern, we have now added appropriate text in the manuscript (Methods, on page 30):

1. *Indeed, we used the p-values assigned by this multivariate method to reduce the QIP features to a smaller number (from 2,104) by selecting the ones with the most discriminative power, while considering all features jointly. However, statistical significance is not relevant to the scope of this imaging analysis, since the latter was used to generate hypotheses that were then tested both in silico and in animal models. Even if the outcome findings of the imaging analysis were*

considered to be just trends, the conclusions of this study, after their evaluation in silico and in vivo, remained unchanged.

2. *Furthermore, traditional correction methods used for correcting for multiple comparisons (e.g. false discovery rate, and/or Bonferroni correction) were designed for multiple independent univariate tests. However, in the method we used, the significance of a feature is not calculated through univariate tests that use each feature independently. In contrast, the method we used for feature selection considers all features together and finds the optimally discriminative combination of all features jointly by a multivariate classifier (Gaonkar and Davatzikos, 2013). Specifically, the p-value for a feature indicates the significance of the weight assigned to this specific feature by the multivariate classifier. Accordingly, in the permutation tests the weights of each feature depend on the weights of all other features. Due to this dependence structure, application of traditional correction methods (that assume for feature independence) to p-values obtained from the method we applied cannot be considered appropriate. Please see a more technical discussion of this issue in (Gaonkar and Davatzikos, 2013) Sec 6.2.*

4. Figure 2 B-E and the corresponding Results were confusing and the interpretation possibly misleading.
4.1: Some of the features shown are from Table S3 but others (T2, rCBV) are not. How are these features being chosen?

The features discussed in our manuscript were chosen based on their radiographic interpretability. In an effort to be inclusive, we have now expanded Table S2 to a comprehensive list of all statistically significant feature observations. We have also included the features that were discussed throughout the manuscript based on their interpretability, but not reaching statistical significance, together with their corresponding p-value. Finally, we have also clarified in our discussion (page 11) that "Although some of the features discussed here and shown in Figure 2B-E were not found to be statistically significant, they were still chosen to be included in our analysis and discussion as their radiographic interpretability was supportive of the overall evaluated radiographic phenotype of the EGFR$^{A289D/T/V}$ mutants."

4.2: It is unclear how the set of EGFR-wt is defined. Does EGFR-wt include EGFR-amplified or vIII-expressing tumors?

Please refer to our response for comment 3.1.

Other studies have identified radiomic features distinguishing proneural vs. mesenchymal tumors. Some of the differences between A289-mt and EGFR-wt shown may in fact reflect differences between EGFR-driven tumors vs. non-EGFR-driven (including most proneural and mesenchymal tumors, by TCGA classification). In order to better distinguish features specific to A289-mt genotype, it would be better to show radiomic features compared across A289-mt vs. EGFR-amplified/A289-wt vs. non-EGFR-amplified.

Reviewer #2 makes a valid point concerning the co-occurrence of the EGFR$^{A289D/T/V}$ mutations with EGFR amplification. To address the possible confounder, we have now analyzed an additional group of only EGFR-amplified patients, where we compared the imaging features across 3 separate groups: EGFR$^{A289D/T/V}$ mutants vs non-mutant/EGFR amplified vs non-mutant/EGFR non-amplified (i.e. WT

EGFR). The results, shown below and included in Figure S3C-D, confirm the feature relationships observed were due to the presence of the EGFR missense mutation and not amplification. FA homogeneity did not show significance between the mutant and amplified populations; the question of the major driving factor for that finding is now the subject of additional work in our group. Additional text has been added on Page 6 stating "Comparison of EGFRA289D/T/V mutants to WT EGFR and EGFR-amplified cases confirmed the association of the imaging features with the A289D/T/V mutation, with the exception of FA homogeneity in the ED (Figure S3C, Table X). Consistently, the ED was previously reported as having a unifying MRI signature across various EGFR pathway activating alterations (including EGFRvIII, EGFR-amplification, EGFRA289D/T/V, EGFRR108K, EGFRG598V) in GBM, compared to WT EGFR (Bakas et al., 2017c)"

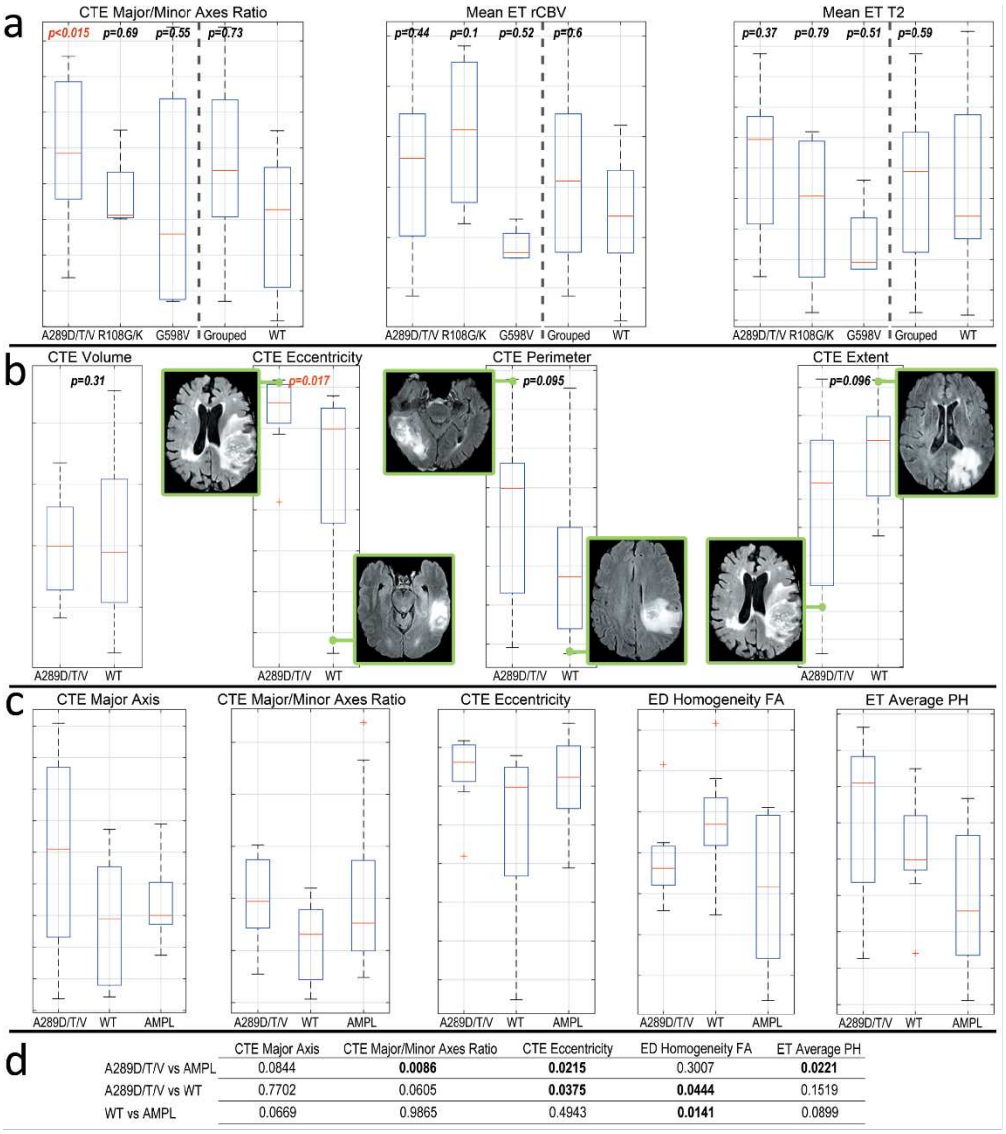

d

	CTE Major Axis	CTE Major/Minor Axes Ratio	CTE Eccentricity	ED Homogeneity FA	ET Average PH
A289D/T/V vs AMPL	0.0844	**0.0086**	**0.0215**	0.3007	**0.0221**
A289D/T/V vs WT	0.7702	0.0605	**0.0375**	**0.0444**	0.1519
WT vs AMPL	0.0669	0.9865	0.4943	**0.0141**	0.0899

Figure S3. Related to Figure 2. (A) Feature comparison across each individual EGFR missense mutation, the grouped mutations, and WT EGFR, for the major: minor axes ratio of the CTE (left), the average rCBV signal in the ET (middle), and the average T2 signal in the ET (right). P-values represent each condition versus WT EGFR. (B) While the volume distribution of the CTE is similar between the $EGFR^{A289D/T/V}$ and the WT EGFR cohorts, the higher eccentricity and perimeter values, combined with lower extent values, in the $EGFR^{A289D/T/V}$ cohort present a picture of more irregularly-shaped tumors, suggestive of more invasive tumors. Insets show representative T2-FLAIR MRI examples of both $EGFR^{A289D/T/V}$ and WT EGFR tumors demonstrating corresponding plotted features. (C) Comparison across $EGFR^{A289D/T/V}$, WT EGFR, and EGFR-amplified patients. $EGFR^{A289D/T/V}$ mutant cases demonstrated distinct distributions from the other two populations, with the exception of the homogeneity in the FA signal of the ED region. (D) Two-sided T test p-values for the features in plotted in (C). Feature definitions: The "Eccentricity" defines the circularity of the assessed shape, i.e. eccentricity value of 0 describes a perfect circle and larger values represent more elongated shapes. The "Perimeter" describes the distance around the boundary of the assessed shape. The "Extent" is the ratio of the area of the assessed shape to the area of its rectangular bounding box. Abbreviations: CTE=complete tumor extent; ET=enhancing tumor; rCBV=relative cerebral blood volume; ED=peritumoral edematous/invaded region; FA=fractional anisotropy; PH=peak height.

4.3: The author's interpretation of the biology underpinning radiomic feature differences is speculative, and more appropriate for the discussion section. From the observation of decreased T1 signal and increased contrast enhancement in A289-mt tumors, it does not follow that these tumors have increased neovascularization or proliferation. RCBV is not significantly different between A289-mt and EGFR-wt tumors. I could not follow the argument for inferring increased tumor invasion from the select imaging parameters shown.

We appreciate the reviewer's comment that the Results section involved some speculative statements, and some parts would be more appropriate for the Discussion section. We have removed all speculative text from the Results and moved it to the Discussion. In regards to the increased neovascularization hypothesis, increased contrast enhancement could reflect neovascularization, which in turn could reflect increased proliferation, per evaluation by our board-certified Neuroradiologist (M.B.). As these outcomes are all suppositional and not conclusive, they have been moved to the Discussion, on Pages 10-11.

To further assist in following the argument for inferring increased tumor invasion for the A289-mt tumors we have added additional figure panels assessing the morphological characteristics of these tumors (Figure S3B and shown under Comment 4.2). The following text has also been added to Page 6: "Additional morphological characteristics, while not demonstrating statistical significance, displayed relationships further emphasizing the irregular shape of the EGFRA289D/T/V mutant tumors (Figure S3B)."

Epidermal Growth Factor Receptor extracellular domain mutations in glioblastoma present opportunities for clinical imaging and therapeutic development

Zev A. Binder[1,2,19], Amy Haseley Thorne[3,19], Spyridon Bakas[1,4,19], E. Paul Wileyto[5], Michel Bilello[1,4], Hamed Akbari[1,4], Saima Rathore[1,4], Sung Min Ha[1,4], Logan Zhang[2], Cole J. Ferguson[6], Sonika Dahiya[6], Wenya Linda Bi[7], David A. Reardon[8], Ahmed Idbaih[9], Joerg Felsberg[10], Bettina Hentschel[11], Michael Weller[12], Stephen J. Bagley[13], Jennifer J.D. Morrissette[14], MacLean P. Nasrallah[15], Jianhui Ma[3], Ciro Zanca[3], Laura Orellana[16,17], Andrew M. Scott[18], Christos Davatzikos[1,4], Frank B. Furnari[3,20, 21], Donald M. O'Rourke[1,2,13,20]

[1]Center for Biomedical Image Computing and Analytics, Perelman School of Medicine, University of Pennsylvania, Philadelphia, PA, 19104, USA.
[2]Department of Neurosurgery, Perelman School of Medicine, University of Pennsylvania, Philadelphia, PA, 19104, USA.
[3]Ludwig Institute for Cancer Research, La Jolla, San Diego, 92093, USA
[4]Department of Radiology, Perelman School of Medicine, University of Pennsylvania, Philadelphia, PA, 19104, USA.
[5]Department of Biostatistics, Epidemiology, and Informatics, Perelman School of Medicine, University of Pennsylvania, Philadelphia, PA, 19104, USA
[6]Division of Neuropathology, Department of Pathology and Immunology, Washington University School of Medicine, St. Louis, MO, 63108, USA
[7]Center for Skull Base and Pituitary Surgery, Department of Neurosurgery, Brigham and Woman's Hospital, Harvard Medical Center, Boston, MA 02115
[8]Center for Neuro-Oncology, Dana-Farber Cancer Institute, Boston, MA 02215
[9]Sorbonne Université, Inserm, CNRS, UMR S 1127, Institut du Cerveau et de la Moelle épinière, ICM, AP-HP, Hôpitaux Universitaires Pitié Salpêtrière - Charles Foix, Service de Neurologie 2-Mazarin, F-75013, Paris, France
[10]Institute of Neuropathology, Heinrich Heine University, Medical Faculty, Moorenstrasse 5, D-40225 Duesseldorf, Germany
[11]Institute for Medical Informatics, Statistics and Epidemiology, University of Leipzig, Medical Faculty, Härtelstrasse 16, D-04107 Leipzig, Germany
[12]Department of Neurology, University Hospital and University of Zurich, 8091 Zurich, Switzerland
[13]Abramson Cancer Center, University of Pennsylvania, PA, 19104, USA
[14]Department of Pathology and Laboratory Medicine, Perelman School of Medicine, University of Pennsylvania, Philadelphia, PA, 19104, USA
[15]Division of Neuropathology, Department of Pathology and Laboratory Medicine, Perelman School of Medicine, University of Pennsylvania, Philadelphia, PA, 19104, USA
[16]Science for Life Laboratory, KTH Royal Institute of Technology, Stockholm, Sweden
[17]Department of Biochemistry and Biophysics, Stockholm University, Stockholm, Sweden
[18]Olivia Newton-John Cancer Research Institute, and La Trobe University, Melbourne, Australia
[19]These authors contributed equally
[20]Senior authors, correspondence: ffurnari@ucsd.edu (F.B.F.), Donald.ORourke@uphs.upenn.edu (D.M.O.)
[21]Lead Contact

Summary

We explored the clinical and pathological impact of EGFR extracellular domain missense mutations. Retrospective assessment of 260 *de novo* glioblastoma (GBM) patients revealed a significant reduction in overall survival of patients with EGFR mutations at alanine 289 ($EGFR^{A289D/T/V}$). Quantitative multi-parametric MRI analyses indicated increased tumor invasion for $EGFR^{A289D/T/V}$ mutants, a finding corroborated in mice bearing intracranial tumors expressing $EGFR^{A289V}$ and dependent on ERK-mediated expression of matrix metalloproteinase-1 (MMP1). $EGFR^{A289V}$ tumor growth was attenuated with an EGFRvIII conformation-specific antibody based on a hypothesized structural convergence. Collectively, the findings of this study indicate a highly invasive and prognostic indicator for the $EGFR^{A289V}$ missense mutation in GBM, postulating $EGFR^{A289V}$ as a molecular marker for responsiveness to therapy with EGFR-targeting antibodies.

Keywords: glioma; glioblastoma; GBM; EGFR; A289D/T/V; survival

Significance

Although EGFR mutants have different biological activities, we here identify an extracellular convergence that may be exploited through broader EGFR ECD targeting. Importantly, when designing clinical trials for EGFR targeted therapies, EGFR ECD missense mutations may give valuable insight into responsive patient populations.

Introduction

Glioblastoma (GBM) is the most common adult, primary, malignant brain tumor with an overall incidence rate of 3.2 per 100,000 in the U.S.(Ostrom et al., 2015). With a median overall survival (OS) of 14.6 months following standard-of-care (SOC), patients diagnosed with GBM have a strikingly poor prognosis (Stupp et al., 2005). Much insight has been gleaned following studies describing the somatic genomic alterations in GBM, with the intended goal of defining core biological pathways to facilitate the discovery of actionable targets for diagnostic and therapeutic purposes (Brennan et al., 2013; Parsons et al., 2008). The 2016 Central Nervous System tumor classification of the World Health Organization incorporated molecular parameters into traditionally microscopy-based histological classification (Louis et al., 2016). Regardless of classification, GBM remains a poorly-margined, diffusely infiltrating necrotic mass that is difficult to treat, in part due to its highly invasive phenotype.

Intra-tumoral heterogeneity is a key factor in the poor therapeutic success for GBM. A seminal study found that 57% of GBM specimens contain a mutation, rearrangement, splicing alteration, and/or amplification of the epidermal growth factor receptor (EGFR). While the most common EGFR variant is a deletion from exons 2-7, EGFRvIII, extracellular domain (ECD) missense mutations comprise 10-15% of transcripts and often co-occur with focal EGFR amplification (Brennan et al., 2013). The contribution of cellular cross-talk between EGFR variants to GBM pathogenicity sheds light on the importance of dissecting the GBM tumor into its single components, rather than focusing on individual mutations (Inda et al., 2010; Zanca et al., 2017). While transforming capacity of several ECD EGFR missense mutants has been described, sufficient analysis of their downstream signaling pathways, their phenotypic impact on the tumor, clinical impact, and potential to specifically target these mutants has yet to be elucidated (Lee et al., 2006).

Multimodal MRI depicts the tumor core as consisting of enhancing (ET), non-enhancing, and necrotic (NET) sub-regions, distinct from the peritumoral edematous/invaded region (ED), which in combination with the tumor core describe the complete tumor extent (CTE) (Bakas et al., 2016). Boosted GLioma Image SegmenTation and Registration (GLISTRboost) is a computer-aided method, utilizing machine-learning algorithms to accurately partition gliomas into its various distinct sub-regions in multimodal magnetic resonance imaging (MRI) scans (Bakas et al., 2017b). This partitioning enables quantitative feature analysis of precise sub-regions from which the clinician may gain valuable insight into the rational selection of targeted agents.

Here we show that patients expressing the EGFR missense mutations A289D/T/V share shorter median OS compared to patients with EGFR that is wildtype at this locus. GLISTRboost imaging analysis and in vivo studies revealed a specific phenotype indicative of increased invasion and higher proliferation of tumors expressing an A289 mutation. Mechanistic exploration of these phenomena demonstrated increased expression of MMP1, driven through a constitutively active EGFR/ERK signaling pathway. Based on the structural convergence of EGFR ECD deletion and missense mutations in exposing the 806-epitope (Orellana et al., 2014), we demonstrate that use of the EGFRvIII-specific monoclonal antibody 806 (mAb806, precursor to ABT-414 (Phillips et al., 2016)) in animal models significantly reduced tumor growth and extended survival of mice bearing A289-mutated gliomas. This is the first study to indicate patient stratification based on the presence of an EGFR ECD missense mutation and suggests

that convergence in receptor structural alterations with EGFRvIII can be leveraged therapeutically.

Results

Demographics of the GBM patient population from the University of Pennsylvania (UPenn) resemble The Cancer Genome Atlas (TCGA) data

To investigate the relationship of EGFR ECD missense mutations with GBM patient OS, patient records from UPenn from 2013 through 2016 demonstrating a confirmed diagnosis of GBM were included for analysis. Of 411 GBM cases, 260 were IDH1 wildtype, de novo GBMs with accompanying next generation sequencing (NGS) data from the UPenn Center for Personalized Diagnostics (CPD). Male to female ratio was 1.5:1 with a median age of 61 at the time of diagnosis (Table S1). The DNA repair protein O^6-methylguanine-DNA methyltransferase (*MGMT*) was methylated in 49% of cases. EGFR amplification was identified in 38% of cases and EGFRvIII was found in 25% of cases. The most common missense mutations were ECD mutations A289D/T/V, R108G/K, and G598V, found in 6%, 3%, and 2% of cases, respectively (Figure 1A). Comparison of the frequency and location of EGFR missense mutations in the UPenn cohort with data from TCGA demonstrated significant overlap (Figure 1B). Analysis of these missense mutations revealed no significant association with gender, age, or EGFRvIII status. However, each was found to co-occur with EGFR amplification (Table 1), while R108G/K was found more frequently in patients with *MGMT* methylation. The majority of patients received SOC, including surgical resection, concurrent radiotherapy and temozolomide (TMZ), and maintenance TMZ. There were no treatment differences in the missense mutation cohorts.

$EGFR^{A289D/T/V}$ missense mutations confer a negative survival benefit in GBM patients

Median OS in the complete cohort was 15 months, with a 2-year survival rate of 21%, and a 5-year survival rate of 10% (Figure S1A). The median OS, 2-year survival rate, and 5-year survival rate of patients with A289D/T/V mutations was 6 months, 12%, and 12%, respectively (Figure 1C). Patients containing a wildtype $EGFR^{A289}$ had a median OS of 15 months, a 2-year OS rate of 22%, and a 5-year OS rate of 11%, demonstrating a significantly shorter median OS for patients harboring the A289D/T/V mutations compared to wildtype at that same position (p=0.028). Patients with R108G/K mutations had a median OS, a 2-year survival rate, and a 5-year survival rate of 17 months, 19%, and 19%, respectively and patients with wildtype $EGFR^{R108}$ had a median OS of 14 months, a 2-year survival rate of 22%, and a 5-year

survival rate of 10%, indicating no significant difference (p=0.77, Figure 1D). Finally, patients with a G598V mutation had a median OS, a 2-year survival rate, and a 5-year survival rate of 17 months, 33%, and 33% respectively and patients with wildtype $EGFR^{G598}$ had a median OS of 15 months, a 2-year survival rate of 21%, and a 5-year survival rate of 10%, also indicating no significant difference (p=0.54, Figure 1E). The discovered $EGFR^{A289D/T/V}$ negative survival association was validated using two independent cohorts. An additional 111 patients from UPenn were evaluated, showing a negative survival association with presence of the $EGFR^{A289D/T/V}$ mutation (p=0.001, Figure S1B). 116 patients from Hôpital Pitié-Salpêtrière (Idbaih et al., 2009) demonstrated a similar negative survival association (p=0.0208, Figure S1C).

Given the association of missense mutation with EGFR amplification, we looked at the survival characteristics of patients with amplified EGFR versus those with WT EGFR (Figure 1F). The median OS for amplified patients was 16 months, compared to 14 months for non-amplified patients and the 2-year and 5-year survival rates were 17% and 5% for the amplified EGFR population compared to 25% and 14% for the WT EGFR population, indicating no significant difference between these two populations (p=0.72).

As $EGFR^{R108G/K}$ and *MGMT* methylation were associated, we looked at the survival characteristics of *MGMT* methylated versus unmethylated patients (Figure S1D). As expected, the median OS of patients with *MGMT* methylation was significantly longer than patients without *MGMT* methylation, at 24 months versus 15 months, respectively, and the 2-year and 5-year survival rates for *MGMT* methylated versus *MGMT* unmethylated were 50% and 18% versus 14% and 12%, respectively. Collectively, the patient survival data from the UPenn cohort revealed a novel oncogenic driving force behind the $EGFR^{A289DT/V}$ mutants, which is distinct from EGFR amplification and *MGMT* methylation status.

Patient specific MRI signatures of EGFR missense mutants suggest an invasive and proliferative phenotype in GBM

The initial comprehensive set of 2,104 Quantitative Imaging Phenomic (QIP) features was pruned into 299 statistically significant ($p<0.05$) features (Table S2) using a multivariate classification framework (Gaonkar and Davatzikos, 2013). QIP features synergistically represented altered imaging signals to formulate a descriptive signature of each EGFR variant (Figure 2A, S2). Grouped together, comparison of WT EGFR with the missense mutants revealed relatively few features that demonstrated statistical significance (Figure S3A, Table

S2). However, when we looked at the individual component, each mutation had a unique set of features associated with it, rather than a unifying radiophenotype (Table S2). While EGFR$^{R108G/K}$ and EGFR^{G598V} did have unique features, the overall picture presented by the EGFR$^{A289D/T/V}$ mutations highlighted possible biological mechanisms that could result in the poor patient OS associated with this mutation; thus, we focused our attention on this specific mutant.

The relative contrast enhancement (rCE) in the ET tissue, defined as the subtraction of the native T1-weighted signal (T1) from the post-contrast (gadolinium) T1 signal (T1Gd), demonstrated a higher value in the presence of an EGFR$^{A289D/T/V}$ mutation (Figure 2B). To investigate the cause of the increased rCE, we assessed the mean value of the T1 signal in the ET. This revealed lower values in the presence of the EGFR$^{A289D/T/V}$ mutation, indicating that the higher contrast value was not solely due to the presence of contrast, but also a lower native T1 signal. Examining the T2 value in the ET, we found that EGFR$^{A289D/T/V}$ mutant tumors had higher values. When combined with the T1 and rCE data, these values supported a radiographic phenotype of higher water content in the tissue. To elucidate a possible cause for this, we examined relative cerebral blood volume (rCBV) and peak height (PH) in the ET (Figure 2C), where both parameters showed higher values in the EGFR$^{A289D/T/V}$ population.

When looking at the CTE, we found the ratio of major to minor axes associated with EGFR$^{A289D/T/V}$ significantly different (Figure 2D). The major axis was defined as the largest 2D distance and the minor axis is perpendicular to the major axis. Additional morphological characteristics, while not demonstrating statistical significance, displayed relationships further emphasizing the more irregular shape of the EGFR$^{A289D/T/V}$ mutant tumors compared to that of the WT EGFR (Figure S3B). Furthermore, the quantitative assessment of the ED region revealed decreased homogeneity of fractional anisotropy (FA) for the EGFR$^{A289D/T/V}$ mutation (Figure 2E), indicating decreased tissue organization, and increased rCE signal. Comparison of EGFR$^{A289D/T/V}$ mutants to WT EGFR and EGFR-amplified cases confirmed the association of the imaging features with the A289D/T/V mutation, with the exception of FA homogeneity in the ED (Figure S3C-D). The ED was previously reported as having a unifying MRI signature across various EGFR pathway activating alterations (including EGFRvIII, EGFR-amplification, EGFR$^{A289D/T/V}$, EGFR^{R108K}, and EGFR^{G598V}) in GBM, compared to WT EGFR (Bakas et al., 2017c).

Mice bearing intracranial EGFR^{A289V} tumors have attenuated survival and an invasive phenotype

Based on patient imaging analysis, we hypothesized that $EGFR^{A289}$ missense mutations conveyed enhanced tumor growth and invasion distinguishable from amplified WT EGFR activity. To test this, we engineered U87 glioma cells and HK281 GBM-spheres to express either WT EGFR or $EGFR^{A289V}$ at levels associated with amplified EGFR found in GBM (Nishikawa et al., 1994). Corroborating our findings in the GBM patient population, mice bearing intracranial tumors harboring the $EGFR^{A289V}$ mutation had a significantly worse survival rate compared to those engrafted with WT EGFR-expressing tumors (Figure 3A, 3C). Histological examination of these tumors revealed a striking increase in invasive fronts as well as increased Ki67 staining (Figure 3B, 3D, S4A-B).

Comparison of $EGFR^{A289V}$ with WT EGFR tumors by T2-weighted MRI at Day 14 further demonstrated a striking difference between the two conditions (Figure 3E-F), and corroborated our radiographic findings in GBM patients. The scans of WT EGFR tumors showed little if any disruption of the normal brain; however, the $EGFR^{A289V}$ images demonstrated large, necrotic tumors with poorly demarcated borders, suggesting an invasive phenotype. While limited modalities of animal imaging do not allow for a quantitative analysis, increased T2 signal throughout the $EGFR^{A289V}$ tumors and in the peritumoral region showed a similar pattern to the patient data. Follow-up histological examination of the imaged brains revealed highly cellular, poorly demarcated, and invasive neoplasms mainly developing unilaterally within the injected neuroparenchyma, confirming the invasive edge of the U87 $EGFR^{A289V}$ tumors (Figure S4C-D).

$EGFR^{A289V}$ missense mutation induces ERK activation and increased MMP1 expression

The results above indicated an aggressive tumor growth phenotype that was imparted by the $EGFR^{A289V}$ mutation in both patients and animal models. To characterize the molecular underpinnings of this mutation, we first examined the expression of matrix metalloproteinases (MMP) 2 and 9, known to convey enhanced glioma cell invasion (Das et al., 2011; Nakada et al., 2003). Surprisingly, we did not find any effect of $EGFR^{A289V}$ on MMP2 or 9 gene expression or secretion in U87 cells (Figure S5A-B). Additionally, invasion through gelatinous substrates was unaffected by $EGFR^{A289V}$ expression (Figure S5C). Next, we examined a panel of MMPs known to be expressed in glioma cells (Hagemann et al., 2012). Here we found a significant increase in MMP1 expression in U87 cells expressing $EGFR^{A289V}$ compared to WT EGFR, $EGFR^{R108K}$, and $EGFR^{G598V}$, which was also induced in HK281 GBM-spheres expressing $EGFR^{A289V}$ compared to WT EGFR (Figure S5, 4A, 4G).

The $EGFR^{A289V}$ missense mutation has been shown previously to be constitutively activated (Lee et al., 2006). To examine the downstream signaling pathways that may have contributed to increased MMP1 expression, we interrogated known signaling effectors by immunoblot analysis of U87 glioma cells harboring mutant EGFR variants. Our results confirm that the $EGFR^{A289V}$ mutation leads to constitutive EGFR activation (Figure 4B). Furthermore, analysis of downstream MAPK, AKT, and STAT3 signaling pathways revealed a striking constitutive activation in the signaling molecule p42/44 MAPK (ERK) in cells expressing the $EGFR^{A289V}$ mutant. Importantly, when we inhibited this signaling pathway using two different MEK inhibitors, U0126 and PD98059, or the tyrosine kinase inhibitors gefitinib and lapatinib, there was a significant reduction in MMP1 gene expression (Figure 4C-F). We confirmed this $EGFR^{A289V}$-driven EGFR/ERK/MMP1 signaling pathway in the HK281 GBM-spheres (Figure 4G-I).

$EGFR^{A289V}$ constitutive EGFR/ERK/MMP1 signaling results in increased invasion and proliferation in vitro

To further delineate the effect of $EGFR^{A289V}$ on EGFR/ERK/MMP1 signaling, we used modified Boyden Transwells coated with collagen, in the presence or absence of MEK inhibitors (Figure S6A-B). Corroborating our in vivo findings, both U87 cells and HK281 GBM-spheres expressing the $EGFR^{A289V}$ mutation showed increased invasion compared to their WT counterparts. When we blocked the ERK signaling pathway by U0126, we rescued the effect in $EGFR^{A289V}$ cells to the level of WT (Figure 5A, 5C). To test the role of MMP1 in this assay, we transduced the $EGFR^{A289V}$-expressing cells with either an shRNA targeting MMP1 or a control shRNA (Figures S6C-D), and showed that in both in vitro glioma models, invasion was attenuated upon MMP1 knockdown (Figure 5B, D).

Next, we tested if increased Ki67 staining in vivo was due specifically to the expression of $EGFR^{A289V}$ (Figure 3B, 3D) by quantifying BrdU incorporation (Figure S6E). We found that $EGFR^{A289V}$ expressing cells had a significantly higher percentage of active proliferation than WT cells in both U87 and HK281 models. Treatment with U0126 again reversed the phenotypic difference, bringing the proliferation percentage in the $EGFR^{A289V}$ cells to a level comparable to the WT EGFR cells (Figure 5E-F). Finally, MMP1 knockdown in vivo nullified the invasive phenotype attributed to the $EGFR^{A289V}$ mutation (Figure 5G-H). The results from these experiments indicated that the increased invasion and proliferation in $EGFR^{A289V}$ expressing

mutant cells was due to a constitutively active EGFR/ERK/MMP1 signaling pathway that can be rescued through pharmacological inhibition.

mAb806 is a potential therapeutic option for patients expressing EGFR^{A289V}

The antibody-drug conjugate, ABT-414, that specifically recognizes EGFRvIII and WT EGFR when expressed at amplified levels, has shown promise in phase I/II clinical trials for GBM patients (Gan et al., 2017; Phillips et al., 2016; Reardon et al., 2017). Prior work has shown that mAb806 detects a convergent structural feature related to constitutive activation, which is shared by heterogeneous EGFR ECD missense mutations, including EGFR^{A289V} (Orellana et al., 2014). To examine the potential efficacy of this therapy for patients expressing EGFR^{A289V}, we used flow cytometry to confirm the ability of mAb806 to bind EGFR^{A289V}. We found mAb806 bound EGFR^{A289V} significantly better than WT EGFR in both U87 and HK281 models (Figure 6A-B). We next assessed the efficacy of this drug in vivo using subcutaneous and intracranial tumor models. To directly test the ability for mAb806 to reduce tumor growth, we engrafted mice subcutaneously with U87 glioma cells expressing WT EGFR, EGFR^{A289V}, or EGFRvIII and treated mice with either mAb806 or vehicle. Using a low dose of mAb806 (0.1 mg/mouse) previously shown to have no effect on WT EGFR expressing cells (Mishima et al., 2001), we verified these results and also show that there is a similar reduction in tumor growth when cells express the EGFR^{A289V} mutation compared to the EGFRvIII deletion mutation (Figure 6C).

To test if mAb806 recognition of the EGFR^{A289V} mutation would lead to an increase in survival, fluorescently labeled U87 cells were engrafted orthotopically in mice, followed by treatment with mAb806 or vehicle and fluorescence molecular tomography imaging (FMT). By Day 16, FMT imaging indicated a strong reduction in fluorescence intensity in mAb806 treated mice bearing tumors expressing EGFR^{A289V} or EGFRvIII, and this difference further intensified over the next week (Figure 6F-G, Day 23). It became clear that the difference in FMT intensity, a direct indicator of intracranial tumor volume, correlated with survival (Figure 6H). In addition to the EGFRvIII model ($p=0.0025$), mAb806 therapy significantly enhanced animal survival in mice bearing EGFR^{A289V} expressing tumors ($p=0.0015$), with only a mild effect on mice bearing WT EGFR expressing tumors ($p=0.06$). This result was reproduced in in the HK281 GBM-sphere model (Figure 6I: WT EGFR expressing tumors $p=0.085$, EGFR^{A289V} expressing tumors $p=0.0048$, Figure S7C-D). This is the first study showing that an EGFRvIII-directed therapy is beneficial to tumors expressing a different EGFR ECD mutation, due to a structural convergent

feature first predicted in silico (Orellana et al, 2014). These results suggest that the $EGFR^{A289V}$ mutation, in addition to EGFRvIII, may be considered a good prognostic indicator for patients undergoing clinical trials with ABT-414. Collectively, this data justifies the further development of EGFR ECD targeting reagents for GBM therapy.

Discussion

In this study, we have demonstrated that the UPenn cohort of GBM patient specimens matches the literature, in terms of demographics, survival, and EGFR mutational frequency and location (Cerami et al., 2012; Stupp et al., 2005). Median OS of patients with GBM following SOC treatment, in the literature, is 14.8 months, closely matching the 15 months OS of our cohort (Stupp et al., 2005). Median age at diagnosis and male: female ratio also closely matched the population data (Dubrow and Darefsky, 2011), as did *MGMT* promoter methylation status, the only prognostic biomarker in GBM (Hegi et al., 2005). EGFRvIII expression and EGFR amplification were lower in the UPenn cohort than in the literature (Heimberger et al., 2005), potentially because our assessment of EGFR amplification was based on the read depth from NGS, compared to fluorescent in situ hybridization (FISH), which is often used in the literature. While NGS offers multiple advantages over FISH, including high-throughput nature and objective quantification, it also averages the reads across the tumor sample. In contrast, FISH assesses individual cells, avoiding the possibility of sample dilution via non-neoplastic sources such as stroma and microglia.

A deeper look at EGFR alterations revealed a trio of ECD missense mutations second to EGFRvIII in frequency. $EGFR^{R108G/K}$, $EGFR^{A289D/T/V}$, and $EGFR^{G598V}$ are the most common missense mutations in both the UPenn cohort and the TCGA population (Cerami et al., 2012). Prior work has demonstrated that these missense mutations have tumorigenic potential (Lee et al., 2006). In addition, structural work on these mutations has pointed towards increased ligand affinity (Bessman et al., 2014). Thus, the overall impact of these mutations could be anticipated to be over-activation of EGFR-driven pathways, leading to increased cell proliferation and invasion (Talasila et al., 2013; Xing et al., 2013). Additionally, we have shown that these mutations share the exposure of a conformational epitope for the antibody mAb806, which is related to ligand-independent activation, increased oncogenicity, and predictive of their response to kinase inhibitors (Orellana et al., 2014).

Turning towards the clinical outcomes from our patient cohort, $EGFR^{A289D/T/V}$ was associated with a worse OS when compared to WT EGFR at the A289 position. In contrast,

EGFR^{G598V} was not associated with survival and EGFR$^{R108G/K}$ presented a complex picture: while the OS trend was neither positive nor negative, EGFR$^{R108G/K}$ mutations were shown to occur in the presence of *MGMT* methylation. As *MGMT* methylation is known to confer sensitivity to TMZ treatment and result in increased OS (Stupp et al., 2005), the true survival impact of the EGFR$^{R108G/K}$ mutation could not be elucidated.

There is increasing evidence demonstrating the validity of advanced computational analysis of QIP features that has shown promise in predicting clinical outcome and molecular characteristics (Aerts, 2016; Bakas et al., 2017a; Bakas et al., 2017c; Ellingson et al., 2017; Gevaert et al., 2017; Gill et al., 2014; Gutman et al., 2013; Itakura et al., 2015; Macyszyn et al., 2016; Zhang et al., 2017). In this study, examination of QIP features associated with the EGFR missense mutations helped to generate hypotheses for the negative survival impact of EGFR$^{A289D/T/V}$. The water content picture presented in the ET could have been due to either increased "leakiness" of existing vessels or increased total blood content as a result of increased neovascularization (Aronen et al., 1994). Together with the relationship of PH values and rCBV values between EGFR$^{A289D/T/V}$ and WT EGFR, this presents a picture of increased proliferation in the ET, and we hypothesized that there was increased total neovascularization. The morphological characteristics of the CTE presented a picture of a highly invasive tumor, penetrating further from the tumor in an asymmetrical pattern. The ED, considered a mix of tumor and normal brain, showed a loss of normal tissue structure accompanied by neovascularization at a level indiscernible to the naked eye, as supported by the decreased homogeneity in the FA signal. A shifting of the composition towards tumor cells, due to increased invasion, would result in a more chaotic picture as the existing brain architecture is disrupted by the tumor cells. Tumor cells would also stimulate neovascularization, leading to the increased gadolinium presence (i.e., increased rCE) we discovered in the EGFR$^{A289D/T/V}$ mutants. Taken together, the major: minor axes ratio, the FA, and the rCE signals suggest increased invasion in the peritumoral ED region of the EGFR$^{A289D/T/V}$ mutant tumors. Although some of the features discussed here and shown in Figure 2B-E were not statistically significant, they were included in our analysis and discussion as they supported the overall evaluated radiographic phenotype of the EGFR$^{A289D/T/V}$ mutants.

While imaging characteristics can suggest underlying biological processes, verification using animal studies is more conclusive. U87 often displays bulky tumors with little presentation of invasion in orthotopic implantations (Miura et al., 2010). The invasive picture presented by the EGFR^{A289V} mutation represents a significant alteration to both the baseline of U87 and U87

expressing WT EGFR. Importantly, we recapitulated this result in the patient-derived HK281 GBM-sphere model, indicating invasion is an attribute of the $EGFR^{A289V}$ mutant in a more pathologically-appropriate model.

EGFR-mediated signaling acts through two main pathways, Ras/Rak/ERK and PIK3CA/Akt, resulting in increased nuclear transcription of genes involved in cellular proliferation and tumor invasion. To explore the mechanism behind the in vivo phenotypes we found, we examined the activation statuses of these two pathways and performed inhibition studies. In both U87 cells and HK281 GBM-spheres, $EGFR^{A289V}$ expression resulted in constitutive phosphorylation of EGFR, as seen previously (Lee et al., 2006). Further analyses revealed that A289V-mediated EGFR activation resulted in constitutive cellular signaling through phosphorylated ERK, ultimately enhancing gene expression of MMP1. Although the $EGFR^{A289V}$ ECD missense mutant does respond to EGF (Figure 4B), it does so weakly in comparison to wild type or the missense mutants $EGFR^{R108K}$ and $EGFR^{G598V}$. Interestingly, while WT EGFR signals mainly through the STAT3 and MAPK pathways, EGFRvIII preferentially acts through the PI3K/AKT pathway (Thorne et al., 2016); $EGFR^{A289V}$ acting primarily through the MAPK pathway thus indicates a divergence in oncogenic signaling activation between EGFR ECD missense and deletion mutants.

A role for MMPs in cancer progression and invasion has been widely characterized. Specifically, MMP2 and MMP9 have been extensively implicated in GBM progression. It has been shown that while MMP1 is not typically expressed in the normal brain, it is elevated in gliomas, correlating with tumor grade and survival (Stojic et al., 2008). Here, we reveal a novel link between the EGFR ECD missense mutant A289V and MMP1 expression, which results in a pro-invasive phenotype. A previous study showed that MMP1 is induced by EGF stimulation in glioma cells (Anand et al., 2011), indicating the likelihood of an exacerbated effect of the $EGFR^{A289V}$-mediated invasive phenotype following stimulation. Interestingly, this study also indicated EGFR/MAPK signaling for its effect, and therefore it is likely that $EGFR^{A289V}$ would mediate its pro-invasive phenotype through this pathway regardless of ligand stimulation.

Directly targeting MMPs in cancer has proven to be a challenge due to structural homology between members of the MMP family and a bilateral role in many cancers (Levin et al., 2017). To date, there have been few clinical trials testing MMP inhibitors for GBM. Most notably, a Phase II trial combining the broad spectrum MMP inhibitor marimastat with TMZ resulted in a PFS at 6 months that significantly exceeded the literature target. However, a

separate randomized, double-blind, placebo-controlled trial indicated that the inhibitor on its own had no effect on patient survival (Groves et al., 2002; Levin et al., 2006) and further studies examining MMP inhibitors for GBM were not conducted.

Along these lines, a significant contributor to the overwhelmingly poor outcome for GBM patients is the relative dearth of active treatments. There are four FDA-approved therapies for GBM: TMZ, carmustine implants, bevacizumab, and NovoTTF-100A (Brem et al., 1995; Friedman et al., 2009; Stupp et al., 2005; Stupp et al., 2012). Novel therapies are needed to improve patient outcomes. Following promising results indicating safety, efficacy studies are currently underway for ABT-414, which specifically targets tumor cells expressing aberrant EGFR (Reardon et al., 2016). Here we examined the prospects of using ABT-414 against GBMs containing the $EGFR^{A289V}$ missense mutant by assessing the efficacy of its non-conjugated precursor, mAb806, in subcutaneous and orthotopic animal models. We found that mAb806 therapy significantly reduced tumor burden and prolonged animal survival in mice bearing $EGFR^{A289V}$ positive tumors to a similar degree as to what has been previously published in mice bearing EGFRvIII positive tumors (Mishima et al., 2001). Significantly, our data demonstrates that ECD mutant structural convergence (Orellana et al., 2014) can be exploited by EGFR-targeted therapies, and indicates that mAb806 is a viable therapeutic option for tumors expressing EGFR mutations other than EGFRvIII. Our study indicates that when deciding measurement outcomes for clinical trials with EGFR-targeted therapies, we should not ignore the smaller EGFR ECD missense mutation populations, as they may provide valuable insight for patient stratification. Importantly, with a baseline poor OS in the $EGFR^{A289D/T/V}$ mutation population, survival benefits in this population may be overshadowed by a lack of significant survival improvement in the WT EGFR cohort.

We have demonstrated the clinical significance of the $EGFR^{A289D/T/V}$ missense mutations in the context of IDH1 wildtype, de novo GBMs. This negative survival impact was reinforced by quantitative imaging analysis suggesting hyperproliferation and increased invasion in patients. Decreased OS, increased proliferation, and increased invasion were demonstrated using modified cell lines in vivo. Mechanistic exploration revealed increased MMP1 expression driven by ERK activation leading to both the increased proliferation and invasion. Finally, the tumor driver status of $EGFR^{A289V}$ was demonstrated by in vivo targeting via mAb806, increasing animal survival and inhibiting tumor growth. These results serve to highlight the complexity of the EGFR signaling cascade and pathway nuances of ECD mutations in the context of cancer.

Acknowledgements

We would like to thank the following organizations for their support: Templeton Family Initiative in Neuro-Oncology (Z.A.B.); NCI: 2T32CA009523-29A1 (A.H.T.); NINDS: R01NS042645 (C.D., D.M.O.), NCI: U24CA189523, NCATS: UL1TR001878, ITMAT of the University of Pennsylvania (S.B., C.D., D.M.O.); NBTS: Defeat GBM Research Collaborative, NIH: RO1NS080939 (F.F); Lawski Fund for Biomedical Research (L.O.). We would also like to thank Kent Osborn, D.V.M., Ph.D., Associate Director for the Animal Care Program at UCSD, and Enrico Radaelli, M.S., V.M.D., D.E.C.V.P., Technical Director for the Comparative Pathology Core in the Department of Pathobiology, School of Veterinary Medicine, University of Pennsylvania, for their assistance with histology.

Author Contributions

Conceptualization, Z.A.B., A.H.T., S.B., L.O., C.D., F.B.F., D.M.O.; Methodology, Z.A.B., A.H.T., S.B., J.J.D.M.; Software, S.B., H.A., S.R.; Validation, Z.A.B., A.H.T., S.B.; Formal Analysis, Z.A.B., A.H.T., S.B., E.P.W., M.B., H.A.; Investigation, Z.A.B., A.H.T., S.B., L.Z., C.Z., J.M.; Resources, Z.A.B., S. B., C.J.F., S.D., W.L.B., D.A.R., A.I., J.F., B.H., M.W., J.J.D.M., M.P.N., C.Z., A.S.; Data Curation, Z.A.B., A.H.T., S.B., S.M.H., C.J.F., S.D., S.J.B.; Writing-Original Draft, Z.A.B., A.H.T., S.B.; Writing-Review & Editing, Z.A.B., A.H.T., S.B., E.P.W., M.B., H.A., S.R., S.M.H., L.Z., C.J.F., S.D., W.L.B., D.A.R., A.I., J.F., B.H., M.W., S.J.B., J.J.D.M., M.P.N., J.M., C.Z., L.O., A.S., C.D., F.B.F., D.M.O.; Visualization, Z.A.B., A.H.T., S.B.; Supervision, Z.A.B., A.H.T., C.D., D.M.O.; Project Administration, Z.A.B., A.H.T.; Funding Acquisition, S.B., C.D., F.B.F., D.M.O.

References

Aerts, H. J. (2016). The Potential of Radiomic-Based Phenotyping in Precision Medicine: A Review. JAMA oncology *2*, 1636-1642.

Anand, M., Van Meter, T. E., and Fillmore, H. L. (2011). Epidermal growth factor induces matrix metalloproteinase-1 (MMP-1) expression and invasion in glioma cell lines via the MAPK pathway. J Neurooncol *104*, 679-687.

Aronen, H. J., Gazit, I. E., Louis, D. N., Buchbinder, B. R., Pardo, F. S., Weisskoff, R. M., Harsh, G. R., Cosgrove, G. R., Halpern, E. F., Hochberg, F. H., and et al. (1994). Cerebral blood volume maps of gliomas: comparison with tumor grade and histologic findings. Radiology *191*, 41-51.

Bakas, S., Akbari, H., Pisapia, J., Martinez-Lage, M., Rozycki, M., Rathore, S., Dahmane, N., O'Rourke, D. M., and Davatzikos, C. (2017a). In Vivo Detection of EGFRvIII in Glioblastoma via Perfusion Magnetic Resonance Imaging Signature Consistent with Deep Peritumoral Infiltration: The ϕ-Index. Clinical cancer research *23*, 4724-4734.

Bakas, S., Akbari, H., Sotiras, A., Bilello, M., Rozycki, M., Kirby, J. S., Freymann, J. B., Farahani, K., and Davatzikos, C. (2017b). Advancing The Cancer Genome Atlas glioma MRI collections with expert segmentation labels and radiomic features. Scientific data *4*, 170117.
Bakas, S., Binder, Z. A., Morrissette, J. J. D., Akbari, H., O'Rourke, D., and Davatzikos, C. (2017c). NIMG-07. UNIFYING MAGNETIC RESONANCE IMAGING SIGNATURE OF EGFR PATHWAY ACTIVATION IN GLIOBLASTOMA CONSISTENT WITH UNIFORMLY AGGRESSIVELY INFILTRATION. Neuro-Oncology *19*, vi143-vi143.
Bakas, S., Chatzimichail, K., Hunter, G., Labbé, B., Sidhu, P. S., and Makris, D. (2017d). Fast semi-automatic segmentation of focal liver lesions in contrast-enhanced ultrasound, based on a probabilistic model. Computer Methods in Biomechanics and Biomedical Engineering: Imaging & Visualization *5*, 329-338.
Bakas, S., Zeng, K., Sotiras, A., Rathore, S., Akbari, H., Gaonkar, B., Rozycki, M., Pati, S., and Davatzikos, C. (2016). GLISTRboost: Combining Multimodal MRI Segmentation, Registration, and Biophysical Tumor Growth Modeling with Gradient Boosting Machines for Glioma Segmentation. Brainlesion: Glioma, Multiple Sclerosis, Stroke and Traumatic Brain Injuries, LNCS *9556*, 144-155.
Bessman, N. J., Bagchi, A., Ferguson, K. M., and Lemmon, M. A. (2014). Complex relationship between ligand binding and dimerization in the epidermal growth factor receptor. Cell reports *9*, 1306-1317.
Brem, H., Piantadosi, S., Burger, P. C., Walker, M., Selker, R., Vick, N. A., Black, K., Sisti, M., Brem, S., Mohr, G., and et al. (1995). Placebo-controlled trial of safety and efficacy of intraoperative controlled delivery by biodegradable polymers of chemotherapy for recurrent gliomas. The Polymer-brain Tumor Treatment Group. Lancet *345*, 1008-1012.
Brennan, C. W., Verhaak, R. G., McKenna, A., Campos, B., Noushmehr, H., Salama, S. R., Zheng, S., Chakravarty, D., Sanborn, J. Z., Berman, S. H.*, et al.* (2013). The somatic genomic landscape of glioblastoma. Cell *155*, 462-477.
Cerami, E., Gao, J., Dogrusoz, U., Gross, B. E., Sumer, S. O., Aksoy, B. A., Jacobsen, A., Byrne, C. J., Heuer, M. L., Larsson, E.*, et al.* (2012). The cBio cancer genomics portal: an open platform for exploring multidimensional cancer genomics data. Cancer Discov *2*, 401-404.
Das, G., Shiras, A., Shanmuganandam, K., and Shastry, P. (2011). Rictor regulates MMP-9 activity and invasion through Raf-1-MEK-ERK signaling pathway in glioma cells. Mol Carcinog *50*, 412-423.
Davatzikos, C., Rathore, S., Bakas, S., Pati, S., Bergman, M., Kalarot, R., Sridharan, P., Gastounioti, A., Jahani, N., Cohen, E.*, et al.* (2018). Cancer imaging phenomics toolkit: quantitative imaging analytics for precision diagnostics and predictive modeling of clinical outcome. J Med Imaging (Bellingham) *5*, 011018.
Doshi, J., Erus, G., Ou, Y., Resnick, S. M., Gur, R. C., Gur, R. E., Satterthwaite, T. D., Furth, S., Davatzikos, C., and Alzheimer's Neuroimaging, I. (2016). MUSE: MUlti-atlas region Segmentation utilizing Ensembles of registration algorithms and parameters, and locally optimal atlas selection. Neuroimage *127*, 186-195.
Dubrow, R., and Darefsky, A. S. (2011). Demographic variation in incidence of adult glioma by subtype, United States, 1992-2007. BMC cancer *11*, 325.
Ellingson, B. M., Gerstner, E. R., Smits, M., Huang, R. Y., Colen, R., Abrey, L. E., Aftab, D. T., Schwab, G. M., Hessel, C., Harris, R. J.*, et al.* (2017). Diffusion MRI Phenotypes Predict Overall Survival Benefit from Anti-VEGF Monotherapy in Recurrent Glioblastoma: Converging Evidence from Phase II Trials. Clinical cancer research *23*, 5745-5756.
Friedman, H. S., Prados, M. D., Wen, P. Y., Mikkelsen, T., Schiff, D., Abrey, L. E., Yung, W. K., Paleologos, N., Nicholas, M. K., Jensen, R.*, et al.* (2009). Bevacizumab alone and in combination with irinotecan in recurrent glioblastoma. J Clin Oncol *27*, 4733-4740.
Gan, H. K., van den Bent, M., Lassman, A. B., Reardon, D. A., and Scott, A. M. (2017). Antibody-drug conjugates in glioblastoma therapy: the right drugs to the right cells. Nat Rev Clin Oncol *14*, 695-707.

Gaonkar, B., and Davatzikos, C. (2013). Analytic estimation of statistical significance maps for support vector machine based multi-variate image analysis and classification. Neuroimage *78*, 270-283.
Gaonkar, B., Macyszyn, L., Bilello, M., Sadaghiani, M. S., Akbari, H., Atthiah, M. A., Ali, Z. S., Da, X., Zhan, Y., O'Rourke, D.*, et al.* (2015). Automated tumor volumetry using computer-aided image segmentation. Academic radiology *22*, 653-661.
Gevaert, O., Echegaray, S., Khuong, A., Hoang, C. D., Shrager, J. B., Jensen, K. C., Berry, G. J., Guo, H. H., Lau, C., Plevritis, S. K.*, et al.* (2017). Predictive radiogenomics modeling of EGFR mutation status in lung cancer. Scientific reports *7*, 41674.
Gill, B. J., Pisapia, D. J., Malone, H. R., Goldstein, H., Lei, L., Sonabend, A., Yun, J., Samanamud, J., Sims, J. S., Banu, M.*, et al.* (2014). MRI-localized biopsies reveal subtype-specific differences in molecular and cellular composition at the margins of glioblastoma. Proceedings of the National Academy of Sciences of the United States of America *111*, 12550-12555.
Gooya, A., Pohl, K. M., Bilello, M., Cirillo, L., Biros, G., Melhem, E. R., and Davatzikos, C. (2012). GLISTR: glioma image segmentation and registration. IEEE transactions on medical imaging *31*, 1941-1954.
Groves, M. D., Puduvalli, V. K., Hess, K. R., Jaeckle, K. A., Peterson, P., Yung, W. K., and Levin, V. A. (2002). Phase II trial of temozolomide plus the matrix metalloproteinase inhibitor, marimastat, in recurrent and progressive glioblastoma multiforme. J Clin Oncol *20*, 1383-1388.
Gutman, D. A., Cooper, L. A., Hwang, S. N., Holder, C. A., Gao, J., Aurora, T. D., Dunn, W. D., Jr., Scarpace, L., Mikkelsen, T., Jain, R.*, et al.* (2013). MR imaging predictors of molecular profile and survival: multi-institutional study of the TCGA glioblastoma data set. Radiology *267*, 560-569.
Hagemann, C., Anacker, J., Ernestus, R. I., and Vince, G. H. (2012). A complete compilation of matrix metalloproteinase expression in human malignant gliomas. World J Clin Oncol *3*, 67-79.
Hansen, C. D., and Johnson, C. R. (2005). The visualization handbook, (Amsterdam ; Boston: Elsevier-Butterworth Heinemann).
Hegi, M. E., Diserens, A. C., Gorlia, T., Hamou, M. F., de Tribolet, N., Weller, M., Kros, J. M., Hainfellner, J. A., Mason, W., Mariani, L.*, et al.* (2005). MGMT gene silencing and benefit from temozolomide in glioblastoma. N Engl J Med *352*, 997-1003.
Heimberger, A. B., Hlatky, R., Suki, D., Yang, D., Weinberg, J., Gilbert, M., Sawaya, R., and Aldape, K. (2005). Prognostic effect of epidermal growth factor receptor and EGFRvIII in glioblastoma multiforme patients. Clinical cancer research *11*, 1462-1466.
Hogea, C., Biros, G., Abraham, F., and Davatzikos, C. (2007). A robust framework for soft tissue simulations with application to modeling brain tumor mass effect in 3D MR images. Physics in medicine and biology *52*, 6893-6908.
Idbaih, A., Aimard, J., Boisselier, B., Marie, Y., Paris, S., Criniere, E., Carvalho Silva, R., Laigle-Donadey, F., Rousseau, A., Mokhtari, K.*, et al.* (2009). Epidermal growth factor receptor extracellular domain mutations in primary glioblastoma. Neuropathol Appl Neurobiol *35*, 208-213.
Inda, M. M., Bonavia, R., Mukasa, A., Narita, Y., Sah, D. W., Vandenberg, S., Brennan, C., Johns, T. G., Bachoo, R., Hadwiger, P.*, et al.* (2010). Tumor heterogeneity is an active process maintained by a mutant EGFR-induced cytokine circuit in glioblastoma. Genes & development *24*, 1731-1745.
Itakura, H., Achrol, A. S., Mitchell, L. A., Loya, J. J., Liu, T., Westbroek, E. M., Feroze, A. H., Rodriguez, S., Echegaray, S., Azad, T. D.*, et al.* (2015). Magnetic resonance image features identify glioblastoma phenotypic subtypes with distinct molecular pathway activities. Sci Transl Med *7*, 303ra138.
Jenkinson, M., Bannister, P., Brady, M., and Smith, S. (2002). Improved optimization for the robust and accurate linear registration and motion correction of brain images. Neuroimage *17*, 825-841.
Jenkinson, M., Beckmann, C. F., Behrens, T. E., Woolrich, M. W., and Smith, S. M. (2012). Fsl. Neuroimage *62*, 782-790.

Lee, J. C., Vivanco, I., Beroukhim, R., Huang, J. H., Feng, W. L., DeBiasi, R. M., Yoshimoto, K., King, J. C., Nghiemphu, P., Yuza, Y.*, et al.* (2006). Epidermal growth factor receptor activation in glioblastoma through novel missense mutations in the extracellular domain. PLoS Med *3*, e485.
Levin, M., Udi, Y., Solomonov, I., and Sagi, I. (2017). Next generation matrix metalloproteinase inhibitors - Novel strategies bring new prospects. Biochim Biophys Acta.
Levin, V. A., Phuphanich, S., Yung, W. K., Forsyth, P. A., Maestro, R. D., Perry, J. R., Fuller, G. N., and Baillet, M. (2006). Randomized, double-blind, placebo-controlled trial of marimastat in glioblastoma multiforme patients following surgery and irradiation. J Neurooncol *78*, 295-302.
Louis, D. N., Perry, A., Reifenberger, G., von Deimling, A., Figarella-Branger, D., Cavenee, W. K., Ohgaki, H., Wiestler, O. D., Kleihues, P., and Ellison, D. W. (2016). The 2016 World Health Organization Classification of Tumors of the Central Nervous System: a summary. Acta neuropathologica *131*, 803-820.
Macyszyn, L., Akbari, H., Pisapia, J. M., Da, X., Attiah, M., Pigrish, V., Bi, Y., Pal, S., Davuluri, R. V., Roccograndi, L.*, et al.* (2016). Imaging patterns predict patient survival and molecular subtype in glioblastoma via machine learning techniques. Neuro Oncol *18*, 417-425.
Mishima, K., Johns, T. G., Luwor, R. B., Scott, A. M., Stockert, E., Jungbluth, A. A., Ji, X. D., Suvarna, P., Voland, J. R., Old, L. J.*, et al.* (2001). Growth suppression of intracranial xenografted glioblastomas overexpressing mutant epidermal growth factor receptors by systemic administration of monoclonal antibody (mAb) 806, a novel monoclonal antibody directed to the receptor. Cancer research *61*, 5349-5354.
Miura, F. K., Alves, M. J., Rocha, M. C., da Silva, R., Oba-Shinjo, S. M., and Marie, S. K. (2010). Xenograft transplantation of human malignant astrocytoma cells into immunodeficient rats: an experimental model of glioblastoma. Clinics (Sao Paulo) *65*, 305-309.
Nakada, M., Okada, Y., and Yamashita, J. (2003). The role of matrix metalloproteinases in glioma invasion. Front Biosci *8*, e261-269.
Nishikawa, R., Ji, X. D., Harmon, R. C., Lazar, C. S., Gill, G. N., Cavenee, W. K., and Huang, H. J. (1994). A mutant epidermal growth factor receptor common in human glioma confers enhanced tumorigenicity. Proceedings of the National Academy of Sciences of the United States of America *91*, 7727-7731.
Orellana, L., Hospital, A., and Orozco, M. (2014). Oncogenic mutations of the EGF-Receptor ectodomain reveal an unexpected mechanism for ligand-independent activation. bioRxiv.
Ostrom, Q. T., Gittleman, H., Fulop, J., Liu, M., Blanda, R., Kromer, C., Wolinsky, Y., Kruchko, C., and Barnholtz-Sloan, J. S. (2015). CBTRUS Statistical Report: Primary Brain and Central Nervous System Tumors Diagnosed in the United States in 2008-2012. Neuro Oncol *17 Suppl 4*, iv1-iv62.
Parsons, D. W., Jones, S., Zhang, X., Lin, J. C., Leary, R. J., Angenendt, P., Mankoo, P., Carter, H., Siu, I. M., Gallia, G. L.*, et al.* (2008). An integrated genomic analysis of human glioblastoma multiforme. Science *321*, 1807-1812.
Phillips, A. C., Boghaert, E. R., Vaidya, K. S., Mitten, M. J., Norvell, S., Falls, H. D., DeVries, P. J., Cheng, D., Meulbroek, J. A., Buchanan, F. G.*, et al.* (2016). ABT-414, an Antibody-Drug Conjugate Targeting a Tumor-Selective EGFR Epitope. Molecular cancer therapeutics *15*, 661-669.
Reardon, D. A., Lassman, A. B., van den Bent, M., Kumthekar, P., Merrell, R., Scott, A. M., Fichtel, L., Sulman, E. P., Gomez, E., Fischer, J.*, et al.* (2016). Efficacy and safety results of ABT-414 in combination with radiation and temozolomide in newly diagnosed glioblastoma. Neuro Oncol.
Reardon, D. A., Lassman, A. B., van den Bent, M., Kumthekar, P., Merrell, R., Scott, A. M., Fichtel, L., Sulman, E. P., Gomez, E., Fischer, J.*, et al.* (2017). Efficacy and safety results of ABT-414 in combination with radiation and temozolomide in newly diagnosed glioblastoma. Neuro Oncol *19*, 965-975.
Sled, J. G., Zijdenbos, A. P., and Evans, A. C. (1998). A nonparametric method for automatic correction of intensity nonuniformity in MRI data. IEEE transactions on medical imaging *17*, 87-97.

Stojic, J., Hagemann, C., Haas, S., Herbold, C., Kuhnel, S., Gerngras, S., Roggendorf, W., Roosen, K., and Vince, G. H. (2008). Expression of matrix metalloproteinases MMP-1, MMP-11 and MMP-19 is correlated with the WHO-grading of human malignant gliomas. Neurosci Res *60*, 40-49.
Stupp, R., Mason, W. P., van den Bent, M. J., Weller, M., Fisher, B., Taphoorn, M. J., Belanger, K., Brandes, A. A., Marosi, C., Bogdahn, U*., et al.* (2005). Radiotherapy plus concomitant and adjuvant temozolomide for glioblastoma. N Engl J Med *352*, 987-996.
Stupp, R., Wong, E. T., Kanner, A. A., Steinberg, D., Engelhard, H., Heidecke, V., Kirson, E. D., Taillibert, S., Liebermann, F., Dbaly, V*., et al.* (2012). NovoTTF-100A versus physician's choice chemotherapy in recurrent glioblastoma: a randomised phase III trial of a novel treatment modality. Eur J Cancer *48*, 2192-2202.
Talasila, K. M., Soentgerath, A., Euskirchen, P., Rosland, G. V., Wang, J., Huszthy, P. C., Prestegarden, L., Skaftnesmo, K. O., Sakariassen, P. O., Eskilsson, E*., et al.* (2013). EGFR wild-type amplification and activation promote invasion and development of glioblastoma independent of angiogenesis. Acta neuropathologica *125*, 683-698.
Thorne, A. H., Zanca, C., and Furnari, F. (2016). Epidermal growth factor receptor targeting and challenges in glioblastoma. Neuro Oncol *18*, 914-918.
Visnyei, K., Onodera, H., Damoiseaux, R., Saigusa, K., Petrosyan, S., De Vries, D., Ferrari, D., Saxe, J., Panosyan, E. H., Masterman-Smith, M*., et al.* (2011). A molecular screening approach to identify and characterize inhibitors of glioblastoma stem cells. Molecular cancer therapeutics *10*, 1818-1828.
Xing, W. J., Zou, Y., Han, Q. L., Dong, Y. C., Deng, Z. L., Lv, X. H., Jiang, T., and Ren, H. (2013). Effects of epidermal growth factor receptor and phosphatase and tensin homologue gene expression on the inhibition of U87MG glioblastoma cell proliferation induced by protein kinase inhibitors. Clinical and experimental pharmacology & physiology *40*, 13-21.
Yushkevich, P. A., Piven, J., Hazlett, H. C., Smith, R. G., Ho, S., Gee, J. C., and Gerig, G. (2006). User-guided 3D active contour segmentation of anatomical structures: significantly improved efficiency and reliability. Neuroimage *31*, 1116-1128.
Zanca, C., Villa, G. R., Benitez, J. A., Thorne, A. H., Koga, T., D'Antonio, M., Ikegami, S., Ma, J., Boyer, A. D., Banisadr, A*., et al.* (2017). Glioblastoma cellular cross-talk converges on NF-kappaB to attenuate EGFR inhibitor sensitivity. Genes & development.
Zhang, B., Chang, K., Ramkissoon, S., Tanguturi, S., Bi, W. L., Reardon, D. A., Ligon, K. L., Alexander, B. M., Wen, P. Y., and Huang, R. Y. (2017). Multimodal MRI features predict isocitrate dehydrogenase genotype in high-grade gliomas. Neuro Oncol *19*, 109-117.

Figure Legends

Figure 1. $EGFR^{A289D/T/V}$ missense mutations are associated with inferior survival in GBM. (A-B) 2D representation of EGFR protein with functional domains indicated by colored segments in the (A) UPenn cohort and (B) TCGA cohort. The location of mutated amino acids is indicated by a bar with a green circle. The height of the bar shows the number of patients in each cohort with the specific mutation. Missense mutations at $EGFR^{A289}$ are the most frequent event in both cohorts. (C-F) KM survival curves for the UPenn cohort, comparing (C) $EGFR^{A289D/T/V}$ to $EGFR^{A289}$, (D) $EGFR^{R108G/K}$ to $EGFR^{R108}$, (E) $EGFR^{G598V}$ to $EGFR^{G598}$, and (F) EGFR amplified to non-amplified. See also Figure S1.

Figure 2. MRI signatures of EGFR missense mutants suggest an invasive and proliferative phenotype. (A) Examples of the four basic/structural MRI modalities used to segment all brain scans into healthy and tumor labels, along with the major axis, minor axis, and the color legend for each label. (B) Selected features found in the ET region presenting a picture of increased neovascularization. (C) Features found in the ET region highlighting the invasive nature of the $EGFR^{A289D/T/V}$ mutation. (D) Ratio of the major and minor axes of the CTE, highlighting the asymmetrical growth pattern of the $EGFR^{A289D/T/V}$ mutants when compared to WT EGFR tumors. (E) Features found in the ED region supporting the picture of increased invasion. See also Figures S2 and S3. Abbreviations: ET=enhancing tumor; NET=non-enhancing tumor; ED=peritumoral edematous/invaded region; CTE=complete tumor extent; WM=white matter; GM= gray matter; CSF=cerebrospinal fluid; PH=peak height; rCBV=relative cerebral blood volume; FA=fractional anisotropy; rCE=relative contrast enhancement.

Figure 3. Mice bearing intracranial $EGFR^{A289V}$ tumors have attenuated survival and an invasive phenotype. KM survival curves comparing mice implanted with either (A) U87 or (C) HK281 tumors expressing either WT EGFR or $EGFR^{A289V}$, n=6 per group, **p<0.01. Representative H&E and Ki67 stained sections of (B) U87 and (D) HK281 tumors expressing WT EGFR or $EGFR^{A289V}$ harvested at time of sacrifice from mice in A and C. Magnification 40x, insets 100x. T2 weighted MRI for (E, left panel) WT EGFR and (F, left panel) $EGFR^{A289V}$ U87 tumors at 20 days, orthotopically implanted in nude mice. 3D volume segmentation map of (E, right panel) WT EGFR and (F, right panel) $EGFR^{A289V}$ mouse brains and tumor. Whole brain is in red and tumor is in green. See also Figure S4.

Figure 4. $EGFR^{A289V}$ missense mutation induces ERK activation and increased MMP1 expression. (A) RT-PCR analysis of MMP1 gene expression in U87 glioma cells expressing WT EGFR, EGFRvIII (V3), $EGFR^{R108K}$, $EGFR^{A289V}$, or $EGFR^{G598V}$. (B, left panel) Western blotting analysis of the indicated proteins in serum starved U87 glioma cells expressing WT EGFR, EGFRvIII, $EGFR^{R108K}$, $EGFR^{A289V}$, or $EGFR^{G598V}$ in the presence or absence of 100ng/ml EGF for 10 minutes at 37C. (B, right panel) Densitometric quantification of immunoblot. (C, left panel) Western blot analysis of the indicated proteins in U87 glioma cells expressing either WT EGFR or $EGFR^{A289V}$ following treatment with gefitinib or lapatinib (4μM, 24h). (C, right panel) Densitometric quantification of immunoblot. (D, left panel) Western blot analysis of the indicated proteins in U87 glioma cells expressing either WT EGFR or $EGFR^{A289V}$ following treatment with U0126 or PD98059 (10μM, 24h). (D, right panel) Densitometric quantification of immunoblot. (E) RT-PCR analysis of MMP1 in U87 glioma cells expressing $EGFR^{A289V}$ following treatment with

gefitinib or lapatinib (4μM, 24h). (F) RT-PCR analysis of MMP1 in U87 glioma cells expressing $EGFR^{A289V}$ following treatment with U0126 or PD98059 (10μM, 24h). (G) RT-PCR analysis of MMP1 in HK281 GBM-spheres expressing WT EGFR or $EGFR^{A289V}$. (H, left panel) Western blot analysis of the indicated proteins in HK281 GBM-spheres expressing either WT EGFR or $EGFR^{A289V}$ following treatment with gefitinib (4μM), lapatinib (4μM), or U0126 (10μM) for 24h. (H, right panel) Densitometric quantification of immunoblot. (I) RT-PCR analysis of MMP1 in HK281 GBM-spheres expressing $EGFR^{A289V}$ following treatment with gefitinib (4μM), lapatinib (4μM), or U0126 (10μM) for 24h. RT-PCR data shown are fold change gene expression relative to GAPDH. Error bars are standard error of the mean of at least three replicates and represent at least three independent experiments. See also Figure S5. ns=not significant, *p<0.05, **p<0.01, ***p<0.001.

Figure 5. Constitutive $EGFR^{A289V}$/ERK/MMP1 signaling results in increased invasion and proliferation in vitro. Quantification of invaded (A, B) U87 glioma cells and (C, D) HK281 GBM-spheres was determined using a modified Boyden Transwell chamber assay coated with collagen. A and C, Quantification of WT EGFR and $EGFR^{A289V}$ cell invasion following treatment with U0126 (10μM) or control for 24 hours. B and D, Quantification of $EGFR^{A289V}$ cells expressing an shMMP1 vector compared to control shRNA. Quantification of % BrdU positive U87 (E) or HK281 (F) cells following BrdU incorporation. Cells were treated +/- U0126 (10μM) 24h prior to BrdU incorporation. Abrogation of invasive phenotype in vivo was obtained with knockdown of MMP1 in both U87 (G) and HK281 (H). Error bars are standard error of the mean of at least three replicates and represent at least three independent experiments. See also Figure S6. ns=not significant, *p<0.05, **p<0.01, ***p<0.001.

Figure 6. MAb806 as a therapeutic option for patients expressing $EGFR^{A289V}$. (A, B) FACS analysis of (A) U87 glioma cells and (B) HK281 GBM-spheres expressing WT EGFR, EGFRvIII, or $EGFR^{A289V}$. Serum starved cells were incubated with either mAb806 or mAb528 (1μg/1x10^6 cells) followed by secondary staining with a FITC-conjugated antibody. Results are shown as mAb806 staining normalized to mAb528 (total EGFR). (C) Mice bearing U87 subcutaneous tumors expressing either WT EGFR, EGFRv3, or $EGFR^{A289V}$ were treated with PBS (100μL/mouse) or mAb806 (0.1mg/100μL/mouse) i.p. 3x/week for 2 weeks once tumors reached an average of 100mm^3. Mean tumor growth after treatment is shown as a function of time. (D) Representative images of IRFP720-expressing tumors as detected by fluorescence molecular topography (FMT) in mice. Mice were implanted intracranially with IRFP720 expressing U87 glioma cells expressing either WT EGFR, EGFRvIII, or $EGFR^{A289V}$ and treated

with PBS (100μL) or mAb806 (1mg/100μL/mouse) i.p. every other day from days 0-14. Quantification of FMT signal intensity on day 23 post-implantation for each region of interest is shown in (E). (F) KM survival curve of mice in (D) and (E). (G) KM survival curve of mice bearing HK281 intracranial tumors as described in (D). n=5 for each animal group. See also Figure S6. ns=not significant, *$p<0.05$, **$p<0.01$.

Tables

Table 1. Demographics of EGFR extracellular domain missense mutations.

			Mutational Status at ECD Locus		
			Wild Type	**Mutated**	**Fisher's Exact Test**
Gender	A289D/T/V	Female	95 (92%)	8 (8%)	0.286
		Male	150 (96%)	7 (4%)	
	R108G/K	Female	98 (95%)	5 (5%)	0.325
		Male	153 (97%)	4 (3%)	
	G598V	Female	102 (99%)	1 (1%)	0.408
		Male	152 (97%)	5 (3%)	
Age	A289D/T/V	0-29	2 (100%)	0 (0%)	0.607
		30-49	26 (100%)	0 (0%)	
		50-69	147 (94%)	10 (6%)	
		70+	70 (93%)	5 (7%)	
	R108G/K	0-29	2 (100%)	0 (0%)	0.795
		30-49	26 (100%)	0 (0%)	
		50-69	151 (96%)	6 (4%)	
		70+	72 (96%)	3 (4%)	
	G598V	0-29	2 (100%)	0 (0%)	0.695
		30-49	25 (96%)	1 (4%)	
		50-69	153 (97%)	4 (3%)	
		70+	74 (99%)	1 (1%)	
***MGMT* Methylation Status**	A289D/T/V	Unmethylated	118 (97%)	4 (3%)	0.175
		Methylated	81 (93%)	6 (7%)	
	R108G/K	Unmethylated	120 (98%)	2 (2%)	**0.036**
		Methylated	80 (92%)	7 (8%)	
	G598V	Unmethylated	118 (97%)	4 (3%)	0.404
		Methylated	86 (99%)	1 (%)	
EGFR Amplification	A289D/T/V	Unamplified	161 (99%)	1 (1%)	**<0.001**
		Amplified	84 (86%)	14 (14%)	
	R108G/K	Unamplified	160 (99%)	2 (1%)	**0.029**
		Amplified	91 (93%)	7 (7%)	
	G598V	Unamplified	161 (99%)	1 (1%)	**0.030**
		Amplified	93 (95%)	5 (5%)	
EGFRvIII Status	A289D/T/V	Negative	144 (94%)	10 (6%)	0.932
		Positive	48 (96 %)	2 (4%)	
	R108G/K	Negative	150 (97%)	4 (3%)	0.103
		Positive	46 (92%)	4 (8%)	
	G598V	Negative	149 (97%)	5 (3%)	1.000

		Positive	49 (98%)	1 (1%)	
Received standard-of-care therapy	A289D/T/V	Yes	158 (95%)	9 (5%)	0.582
		No	78 (93%)	6 (7%)	
	R108G/K	Yes	161 (96%)	6 (4%)	1.000
		No	81 (96%)	3 (4%)	
	G598V	Yes	163 (98%)	4 (2%)	1.000
		No	82 (98%)	2 (2%)	

Bolded values represent statistically significant Fisher's Exact Test p-values. Abbreviations: ECD, extracellular domain; *MGMT*, O^6-methylguanine-DNA methyltransferase; EGFR, Epidermal Growth Factor Receptor; EGFRvIII, EGFR variant III.

STAR Methods

Contact for Reagent and Resource Sharing

Further information and requests for resources and reagents should be directed to and will be fulfilled by the Lead Contact, Frank B. Furnari (ffurnari@ucsd.edu).

Experimental Model and Subject Details

Patient Cohort

Patients undergoing surgical resection for a cranial malignancy were identified through the UPenn CPD. GBM diagnoses were confirmed via medical records containing neuropathological assessment. Exclusion criteria were IDH1 mutation as determined by NGS, 1p19q co-deletion, recurrent resection, and prior diagnosis of a lower grade glioma. There were a total of 260 cases that fit all the criteria. Full patient demographics are presented in Table S1.

Cell Lines

U87 glioma cells were maintained in Dulbecco's Modified Eagle Medium (DMEM) containing 10% FBS and 1% penicillin/streptomycin. HK281 GBM-spheres (a kind gift from Harley Kornblum, UCLA, (Visnyei et al., 2011)) were cultured in DMEM/F12 medium supplemented with 1x B27 (GIBCO/Life Technologies), 1% penicillin/streptomycin, human recombinant EGF (20 ng/mL), bFGF (20 ng/mL) and 2 mg/mL heparin (StemCell Technologies).

All cells were maintained at 37°C, 5% CO2, and 100% relative humidity for the duration of the experiment. Reagents used in this study were obtained from the following sources: Antibodies: EGFR (BD Biosciences), pan-phospho-Tyrosine-HRP (R&D Systems), p42/44 MAPK, phospho-p42/44 MAPK, STAT3, phospho-STAT3 y705, AKT, phospho-AKT s473 (Cell Signaling Technology), Ki67 (Santa Cruz Biotechnology), and β-Actin (Sigma). Inhibitors: U0126 and PD98059 (LC Laboratories). The monoclonal antibody 806 was produced in the Biological Production Facility at the Olivia-Newton John Cancer Research Institute (Melbourne, Australia).

Animals

All animal experiments were performed in accordance with the IACUC at the University of California, San Diego or the University of Pennsylvania. Four to six week old female Athymic nu/nu mice were used for the subcutaneous tumor studies and six to eight week old female Athymic nu/nu mice were used for the intracranial tumor studies (Charles River Laboratories, Frederick, MD; The Jackson Laboratory, Bar Harbor, ME). For subcutaneous studies, mice were injected into the rear right flank with $2.5x10^5$ U87 glioma cells expressing WT EGFR, EGFRvIII, or $EGFR^{A289V}$. When tumors reached an average size of 100 mm^3 mice were injected intraperitoneally with either PBS control or mAb806 antibody (0.1 mg/mouse in 100 µL PBS) 3x/week, for two weeks. Tumor width (*a*) and length (*b*) were obtained using calipers and tumor volumes were determined using the formula $V = ½ \times a^2 \times b$, where $b \leq a$. Mice were euthanized when tumor volumes exceeded 1,500 mm^3. For intracranial studies, mice were anesthetized and fixed in a stereotactic apparatus, and a burr hole was drilled at 2 mm right or left lateral to bregma. U87 glioma cells or HK281 GBM-spheres expressing WT EGFR, EGFRvIII, or $EGFR^{A289V}$ (1×10^5 cells) were implanted at a depth of 3 mm. Every other day, from day 0 – 14, mice were injected intraperitoneally with mAb806 or PBS control (1 mg/mouse in 100 µL PBS). Animals were observed daily and were euthanized when they showed signs of morbidity.

Method Details

EGFR Mutational Status

EGFR mutation status (single nucleotide variants, indels) was obtained from the CPD through an NGS assay. Briefly, formalin-fixed paraffin-embedded (FFPE) tumor tissue blocks

were selected by a neuropathologist and sent to the CPD for processing. DNA was extracted from the tissue following manufacturer's instructions (Qiagen, Valencia, CA). After extraction, DNA quality and concentration were assessed (Agilent, Santa Clara, CA; Life Technologies, Waltham, MA). For NGS, between 10 and 200 ng of DNA was used to prepare the library. Samples were multiplexed and read on a MiSeq (Illumina, San Diego, CA) with an average read depth of 2500x. NGS data was processed through an in-house bioinformatics pipeline, identifying variants and amplifications of EGFR by standard methods.

EGFRvIII Expression

EGFRvIII determination was made by NGS sequencing through the CPD. A total of 204 of the 260 cases were assessed for EGFRvIII expression. Briefly, using primers designed to capture both EGFRvIII and WT EGFR, NGS library preparations were amplified and sequenced using MiSeq (Illumina, San Diego, CA). The resulting data was processed through an in-house bioinformatics pipeline that quantified EGFRvIII as a fraction of total EGFR. Samples with an EGFRvIII fraction greater than 5% were considered to be positive.

MGMT Methylation

A total of 209 cases were examined for *MGMT* promoter methylation. The initial 91 samples were sent out to an outside laboratory (ARUP, Salt Lake City, UT). The remaining 118 samples were processed at UPenn. Briefly, DNA was extracted from FFPE blocks following manufacturer's instructions (Qiagen, Valencia, CA). Bisulfite conversion was carried out according to manufacturer's instructions (Zymo Research, Irvine, CA) and DNA was then amplified using PCR targeting 4 CpG islands in exon 1 of *MGMT*. The PCR results were then pyrosequenced to assess the presence of methylation at each CpG island (Qiagen, Valencia, CA).

Magnetic Resonance Imaging Acquisition

The assessed patients were pre-operatively scanned, as part of the UPenn standard care protocol of patients with brain tumors, using an advanced MRI acquisition protocol of 6

different modalities, comprising native (T1) and contrast-enhanced (T1Gd) T1-weighted, T2-weighted (T2), T2 Fluid-Attenuated Inversion Recovery (T2-FLAIR), Diffusion Tensor Imaging (DTI), and Dynamic Susceptibility Contrast (DSC) MRI volumes. The GBM patients with available advanced MRI brain scans included 13 WT EGFR, 11 EGFR-amplified, 11 $EGFR^{A289D/T/V}$, 4 $EGFR^{R108G/K}$, and 4 $EGFR^{G598V}$. The protocol was approved by the Institutional Review Board at the Hospital of the University of Pennsylvania (HUP), and informed consent was obtained from all subjects. No randomization method was used for allocating samples to experimental groups.

All MRI scans were acquired in the axial plane using 3-Tesla Siemens Magnetom Trio A Tim clinical MRI systems (Erlangen, Germany), according to the standardized advanced acquisition protocol followed at the HUP. MRI specifics are available in Table S4. The contrast material used in the scans included in this study was either gadodiamide (Omniscan, GE Healthcare, Mickleton, NJ), or gadobenate dimeglumine (MultiHance, Bracco SpA, Milan), and administered intravenously (IV). The total dose of contract material was divided into two IV injections to help minimize errors due to potential contrast leakage out of intravascular space. The initial loading dose described the 25% of the total injected contrast material and the second bolus injection the remaining 75%, with a delay of 5-minutes. The exact contrast material dosage was dependent on patient weight and given on a relative proportion of 0.3 mL/kg. The T2 volumes were acquired prior to any contrast administration. The T2-FLAIR volumes were acquired between the initial IV injection and the DSC acquisition. The DSC acquisition was performed during the second IV injection of the contrast material. DTI scans (Axial 2D) were acquired using a single-shot spin echo planar imaging sequence (Variant: segmented k-space\spoiled, Options: Partial Fourier-Phase\Fat Saturation), with 95 phase encoding steps. Following acquisition at b=0 s/mm^2 (repeated 3 times), diffusion weighted images were acquired (b=1000 s/mm^2) with diffusion gradients applied in 30 directions.

Image Pre-processing

All acquired volumes were converted from DICOM to NIfTI and oriented to the RAI coordinate system convention, as part of the requirements of the segmentation algorithm we used (Bakas et al., 2017b). All patient scans were co-registered to a single T1Gd template using an affine registration, through the Oxford center for Functional MRI of the Brain (FMRIB) Linear Image Registration Tool (FLIRT) (Jenkinson et al., 2002) of the FMRIB Software Library (FSL)

(Jenkinson et al., 2012). All brain scans were then skull-stripped using a template library of 216 MRI brain scans and their corresponding masks. This library was used for target specific template selection and subsequent registrations MUlti-atlas Segmentation utilizing Ensembles (MUSE) (Doshi et al., 2016). A final step based on region-growing guided by the T2 signal was applied to obtain a brain mask that includes the intra-cranial CSF. High frequency intensity variations in regions of uniform intensity profile, while preserving the underlying tissue structure was then applied using the Smallest Univalue Segment Assimilating Nucleus (SUSAN) approach (Jenkinson et al., 2002). Non-uniformities of the image intensity caused by the inhomogeneity of the magnetic field during acquisition were removed using a non-parametric, non-uniform intensity normalization algorithm (Sled et al., 1998), and the intensity histograms of all modalities of all patients were then matched to the corresponding modality of a single reference patient. A set of DTI measurements were extracted from the DTI volumes for comprehensive analysis, namely the tensor's fractional anisotropy DTI(FA), radial diffusivity DTI(RAD), axial diffusivity DTI(AX), and apparent diffusion coefficient DTI(ADC). Furthermore, parametric maps of clinical parameters from the temporal perfusion dynamic volumes (i.e., DSC-MRI) were extracted, comprising the relative cerebral blood volume (rCBV), peak height (PH) and percentage signal recovery (PSR). Both the DTI and the DSC extracted maps were treated as individual image modalities.

Tumor Segmentation

The method used to segment each tumor into its various histologically distinct sub-regions is named GLISTRboost (Bakas et al., 2017b) and it is based on a hybrid generative-discriminative model. The generative part (Gooya et al., 2012) incorporates a glioma growth model (based on a reaction-diffusion-advection model) (Hogea et al., 2007), and follows an Expectation-Maximization (EM) framework to segment the brain scans into tumor (i.e., ET, NET and ED), as well as healthy tissue labels (i.e., WM, GM, CSF, vessels and cerebellum), and register a healthy population probabilistic atlas to glioma patients' brain scans using the tumor growth model to account for mass effects. The discriminative part is based on a gradient boosting multi-class classification scheme and used to refine the tumor sub-region labels based on information from multiple patients. Lastly, a Bayesian strategy (Bakas et al., 2017d) is employed to further refine and finalize the tumor segmentation based on patient-specific intensity statistics from the multimodal MRI scans available (Fig. 2A).

GLISTRboost is designed to tackle cases with both solitary and multifocal masses of complex shapes with heterogeneous texture. It requires manual input of tissue seed-points for each segmentation label, to capture the intensity variation and model the intensity distribution (i.e., mean and variance) across all modalities. However, the coordinate position of these input seed-points is not taken into consideration by the segmentation method, but only the corresponding intensity value. Therefore, any potential variation in the coordinates of seed-points initialized during independent initialization attempts should not affect the output segmentation labels, given that the modelled intensity distributions during these attempts are the same. In addition to the seed-points for each tissue class, a single seed-point and a radius are also required to approximate the bulk volume of each apparent tumor by a spherical parametric model, which is then used as a prior to the tumor growth model (Hogea et al., 2007). This growth model deforms a healthy population probabilistic atlas into a glioma patient brain scan matching the input scan, while approximating the brain tissue deformations occurred due to the mass effect of the tumors. A random-walk-based generative model estimates a tumor shape prior, initialized by the spherical parametric model. This prior is incorporated in the generative part of GLISTRboost via an empirical Bayes model (Gooya et al., 2012) and produces a probability map for each tissue label, leading to an integrative non-overlapping segmentation label map. This label map is then refined by a voxel-level multi-label classification through a gradient boosting ensemble model of decision trees. We trained decision trees of maximum depth 3 in a subset of the training data to introduce randomness and using a cross-validation framework to avoid overfitting. Sampling rate of 0.6 was used, while additional randomness was introduced by sampling stochastically a subset (square root of the total number of features) of imaging features at each node. The exact features use for training this discriminative part of GLISTRboost, consisted of i) intensity, ii) image derivatives, ii) geodesic distance transform, iv) texture parameters and the tissue probability maps. The intensity parameters comprise the raw intensity voxel value at each MRI modality, as well as their differences across all four modalities. The image derivatives are summarized by the Laplacian of Gaussians and the image gradient magnitude. These sets of parameters are extracted after performing an intensity normalization based on the median intensity of the current cerebrospinal fluid segmentation label. The geodesic distance transform was estimated for each voxel from the initialized tumor center seed-point (Gaonkar et al., 2015). Texture features were based on a gray-level co-occurrence matrix (GLCM) and extracted following discretization of the input volumes into 64 gray levels and using a bounding box of 125 voxels (5x5x5) for each voxel of each image. The GLCM accounted for intensity values within a radius of 2 voxels and for 26 3D

directions to extract the energy, entropy, dissimilarity, homogeneity (i.e., inverse difference moment of order 2), and inverse difference moment of order 1. The tumor segmentation labels of each patient were then further refined based on individual patient intensities (Bakas et al., 2017d). First the intensity distributions of the WM, ED, NET and ET were populated, considering the corresponding voxels of tissue probability equal to 1. The histograms of the 3 pair-wise distributions considered (i.e., ED vs WM in T2-FLAIR, ET vs ED in T1-Gd, and ET vs NET in T1-Gd) were then normalized. The maximum likelihood estimation was then used to model the class-conditional probability densities ($Pr(I(v_i)|Class$) of each class by a distinct Gaussian model for each class. The voxels of each class in a close proximity (4 voxels) to the voxels of the paired class, were then iteratively evaluated by assessing their intensity $I(v_i)$ and comparing the $Pr(I(v_i)|Class_1)$ with $Pr(I(v_i)|Class_2)$. The voxel v_i was then classified into the class with the larger conditional probability, which is equivalent to a classification based on Bayes' Theorem with equal priors for the two classes, i.e., $Pr(Class_1) = Pr(Class_2) = 0.5$.

Extraction of Quantitative Imaging Phenomic Features

Accurate delineation of the three histologically distinct tumor sub-regions (i.e., ET, NET, ED) enabled us to extract QIP features (n=2104), accurately corresponding to each of the sub-regions. Specifically, these QIP features comprise: 21 volumetric measurements, 11 parameters describing the spatial configuration and distribution of the tumor, 1650 radiomic features (150 for each modality assessed), 330 histogram-based intensity parameters (30 for each modality), 66 first order statistics of image intensities (the mean and standard deviation of each sub-region in each modality), 21 parameters descriptive of the tumor's shape, and 5 glioma diffusion properties extracted from tumor biophysical models using reaction-diffusion-advection equations.

Multivariate Machine Learning Analysis

An analytic estimation of statistical significance based on multivariate analysis (Gaonkar and Davatzikos, 2013) was employed to calculate the relative contribution of each QIP feature extracted on distinguishing the EGFR missense mutants from WT EGFR by assigning a corresponding p-value. The multivariate approach was based on a support vector machine formulation for classification using a linear kernel function. The parameter for the soft margin

cost function (c) was optimized on the training data based on a five-fold cross validated grid search; $c=2^{\alpha}$, where $\alpha \epsilon [-5,5]$. This parameter controls the influence of each individual support vector that involves trading error penalty for stability. This analytic estimation assesses the relative individual contribution of each feature, while considering the synergistic interactions with other features, and assigns a conservative p-value to each feature for evaluating/quantifying the statistical significance of each. Feature selection was conducted by selecting those features with a p-value above a certain threshold ($p>0.05$). Next, we analytically estimated the statistical significance (i.e., p-values) of all extracted radiomic features distinguishing the EGFR missense mutants from WT EGFR, as well as between the EGFR mutants, based on a multivariate classification framework (Gaonkar and Davatzikos, 2013). Note that WT EGFR here described only those tumors that had confirmed wildtype EGFR at normal expression levels, thereby excluding EGFRvIII, amplification, and mutations at A289, R108, and G598 residues. This multivariate analysis enabled us to prune the extensively comprehensive set including 2,104 QIP features into 299 statistically significant ($p<0.05$) features (Table S2). Subsequent selection of features based on radiographic interpretability, according to a board-certified Neuroradiologist (M.B.), further reduced these features to a more manageable set of 17 QIP features (Table S3).

Typically, p-value corrections for multiple comparisons are considered for assignment of statistical significance. However, statistical significance was not relevant to the scope of our imaging analysis, since the latter was used to generate hypotheses that were then tested both in silico and in vivo. Even if the outcome findings of the imaging analysis were considered trends, the conclusions of this study, after their evaluation in silico and in vivo, remained unchanged. Furthermore, traditional correction methods used (e.g. false discovery rate, and/or Bonferroni correction) were designed for multiple independent univariate tests. In the multivariate method we used, the significance of a feature was not calculated through univariate tests that use each feature independently. In contrast, our feature selection considered all features together and found the optimally discriminative combination of all features jointly by a multivariate classifier (Gaonkar and Davatzikos, 2013). Specifically, the p-value for a feature indicated the significance of the weight assigned to this specific feature by the multivariate classifier. Accordingly, in the permutation tests, the weights of each feature depended on the weights of all other features. Considering the assumption of traditional correction methods for feature independence did not hold true, their application was not appropriate.

Reagents

Plasmids. For U87 transduction, pLRNL retroviral plasmids containing the full length wild type EGFR and the truncated EGFRvIII constructs were previously reported (Zanca et al., 2017). The EGFR ECD missense mutations were generated from the WT EGFR construct by site-directed mutagenesis (Agilent Technology), according to manufacturer's instructions. Primers used were as follows: $EGFR^{A289V}$ forward 5'-caaatacagctttggtgtcacctgcgtgaagaagt-3' and reverse 5'-acttcttcacgcaggtgacaccaaagctgtatttg-3', $EGFR^{R108K}$ forward 5'-aaacctgcagatcatcaaaggaaatatgtactac-3' and reverse 5'-gtagtacatatttcctttgatgatctgcaggttt-3', $EGFR^{G598V}$ forward 5'-caagacctgcccggcagtagtcatgggagaaaaca-3' and reverse 5'-tgttttctcccatgactcatgccgggcaggtcttg-3'. For HK281 transduction, the pLRNL constructs were used to subclone WT EGFR and $EGFR^{A289V}$ into the pLV-EF1a-MCS-IRES-Hyg plasmid (Biosettia). The near-infrared fluorescent protein IRFP720 cDNA construct was described previously (Zanca et al., 2017). The MMP1 Mission shRNA pLKO.1 plasmid was obtained from Sigma (clone NM_002421.3-986s21c1).

Retro- and Lentivirus production and transduction

To produce retrovirus, HEK 293T cells were co-transfected with pLRNL vectors and the pCL10A1 packaging construct using Lipofectamine 2000 reagent (Life Sciences). Viral supernatants were collected and filtered at 48 and 72 hours following transfection and used to infect cells overnight in the presence of 10 µg/mL polybrene. Cells were then selected and maintained with neomycin (400 µg/mL). To produce lentivirus, HEK 293T cells were co-transfected with pLV or pLKO.1 vectors, along with pRev, pMDL, and VSVg packaging constructs using Lipofectamine 2000. Supernatants were collected and filtered at 48 and 72 hours after transfection. Viral supernatant was concentrated by centrifugation at 23,000 x g for 2 hours at 4°C and used to infect cells overnight in the presence of 10 µg/mL polybrene. Cells were selected and maintained with hygromycin (200 µg/mL, pLV-EF1a-MCS-IRES-Hyg), puromycin (2ug/ml, shMMP1), or blastocidin (5ug/ml, IRFP720), depending on vector. Gene expression was verified by western blot, real time PCR, and FACS analysis.

FACS (Fluorescent-activated Cell Sorter) Sorting and Analysis.

For the generation of stable U87 cell lines and HK281 GBM-spheres expressing equal levels of EGFR, cells were collected at 1 x 10^6 cells in 100 µL FACS buffer (PBS + 1% FBS) and exposed to 1 µg of the EGFR monoclonal antibody 528, which recognizes WT and mutant EGFR, for 1 hour. Cells were then exposed to FITC-conjugated goat anti-mouse IgG antibody for 1 hour. Stained cells were analyzed by SH800 Cell Sorter (Sony Biotechnology) and sorted to within 10% of the mean FITC intensity of control cells expressing EGFRvIII. Sorted cells were cultured and reanalyzed to confirm stability of receptor levels. To measure binding affinity to the mAb806 antibody, the cells were processed as above but each cell line was stained separately with 1µg of either antibody 528 or mAb806, followed by a secondary staining with a FITC-conjugated antibody. Mean FITC intensity following mAb806 staining was normalized to the corresponding mean FITC intensity for antibody 528.

Western Blotting

Cells were seeded in 10% FBS overnight to allow for adherence and then serum starved for 24 hours and treated with or without EGF at 100 ng/mL for 10 minutes at 37°C. Cell lysates were collected on ice with RIPA buffer (50 mM Tris-HCl, 150 mM NaCl, 1% NP-40, 0.5% Sodium Deoxycholate, 0.1% SDS, 5 mM EDTA) supplemented with protease (Roche) and phosphatase (Sigma) inhibitors. Protein concentration was determined using a standard DC assay (Bio-Rad) and equal amounts were loaded and separated by SDS-PAGE and then transferred to PVDF membranes. The membranes were blocked with buffer containing 5% BSA in tris-buffered saline with 0.1% Tween-20 (TTBS) for 1 h and incubated overnight with primary antibodies at 4°C. Membranes were washed with TTBS, and then incubated with HRP-conjugated secondary antibodies (Sigma-Aldrich) and developed with an enhanced chemiluminescence detection kit (Pierce). ImageJ software was used to quantify band signal intensity normalized to total protein.

FMT Imaging

For the intracranial in vivo experiments, tumor growth was monitored via fluorescence molecular tomography using the FMT 2500 Fluorescence Tomography System (PerkinElmer). Signal intensity was calculated based on ROI and analyzed using Perkin Elmer software.

Immunohistochemistry

Formalin-fixed, paraffin-embedded (FFPE) tissue sections were prepared by the Histology Core Facility at UCSD Moores Cancer Center. Immunohistochemistry was performed according to standard procedures using the Scytek SensiTek HRP (AEC) Staining System. Antigen was retrieved by boiling slides in 0.01 M of sodium citrate (pH 6.0) in an oven for 30 minutes. Sections were incubated with primary antibody at 4°C overnight, followed by incubation with biotinylated secondary antibodies at room temperature for 20 min. Nine representative images from each immunostained section were taken with a Keyence BZ-X700 microscope and analyzed with BZ-X Analyzer Keyence software.

For pathological examination, the entire head was collected and fixed for approximately 5 days in 4% PFA at 4 °C. After fixation, brain was removed from the skull and serially sliced using the coronal brain matrix system (Zivic Instruments BSMYS001-1). Five slices were obtained from each brain using the following anatomical landmarks as references: paraflocculi, infundibulum/median eminence, optic chiasm, cranial border of olfactory tubercles. Sliced brains were then processed for paraffin embedding (Thermo Scientific Excelsior™ AS Tissue Processor and HistoStar™ Embedding Workstation) and serial sagittal sections of 5 µm were obtained (Reichert Jung 2030 microtome). Sections were mounted on Superfrost microscope slides (Fisherbrand 12-550-14) and stained with hematoxylin and eosin (H&E) using the Gemini AS automated slide stainer (Thermo Fisher Scientific). H&E-stained slides were finally evaluated by a board certified veterinary pathologist (ER) and representative pictures were captured using an Olympus BX53 microscope coupled with an Olympus DP25 camera.

Animal MRI Studies

All MRI studies were performed in the Small Animal Imaging Facility in the Department of Radiology at the University of Pennsylvania, on a 9.4T horizontal bore scanner (Agilent Inc, Palo Alto, CA) equipped with a 12 cm ID, 40 gauss/cm gradient tube. Animals were prepared for study by induction of general anesthesia using 1-2% inhaled isoflurane through a nose cone. A respiration pillow and rectal temperature probe were placed on the animal and attached to a MR compatible vital signs monitoring system (Small Animal Instrument Inc, Stonybrook, NY). The animals were then mounted in a 20 mm ID quadrature birdcage RF coil (M2M Imaging,

Cleveland, OH) and positioned in the magnet. The vital signs monitoring system was equipped with a regulated warm air source which was directed over the animal during the study to maintain the core body temperature at 37±1°C. Respiration and core body temperature were monitored throughout the study and the isoflurane level was adjusted as needed to maintain a deep anesthesia. Following optimization of RF transmitter power and generation of scout images, a contiguous series of T2-weighted, fast spin echo, axial slices spanning the brain (cerebral cortex or cerebellum) was generated with the following parameters: TR = 3800 msec; ETL = 8; ESP = min (10.96); k_{zero} = 5; Effective TE = 54.80 msec; averages = 8; dummy scans = 2; FOV = 20 x 20; matrix = 256 x 256; slice thickness = 0.5 mm; 30 slices total. Images were converted to the Meta file format for 3D volumetric analysis using the ITK-SNAP program. The total brain volume and volume of the T2 abnormality were determined (Yushkevich et al., 2006). The overlay maps were generated using ParaView (Hansen and Johnson, 2005).

Cell Invasion Assay

In vitro cell invasion was evaluated using a 24-well chemotaxis chamber equipped with a polycarbonate filter with 8 µm pores (Costar, Corning, NY). Prior to plating, transwells were coated with Pure Col, Bovine Collagen Solution, Type I collagen for 30 minutes at 37°C (1:30 in 0.1% FBS, DMEM for U87 cells, 1:30 in F12 DMEM for HK281 GBM-spheres). Serum starved cells were incubated with the indicated inhibitor for 24 hours prior to plating. Cells were then counted and plated in the upper chamber and left to migrate for 6 hours towards 10% FBS, DMEM. Following incubation, cells that traversed the membrane were fixed and stained with crystal violet and non-migrated cells were removed with a cotton-tipped applicator. Cells were quantified by averaging the cell count of 5 different view fields at 20x magnification from at least three independent transwells.

BrdU Assay

For U87 glioma cells, BrdU assessment was carried out as follows: cells were plated on coverslips (10,000 cells/well in a 24 well plate), cultured for 7 days, and then incubated in the presence of 10 µM BrdU for 4-6 hours. The cells were fixed in 4% PFA (Sigma), stained with anti-BrdU antibody (BD), and counterstained with Hoechst 33258 (Sigma). The number of BrdU-positive cells was scored as a percentage of the total number of cells counterstained with

Hoechst 33258. All pictures were captured using Nikon DS-Ri1 microscope. The assay was performed in triplicate for all conditions. For HK281 GBM-spheres, cells were plated in 6-well dishes (200,000 cells/well), cultured for 24 hours and then incubated in the presence of 10 μM BrdU for 6 hours. Cells were washed once with PBS, and 50,000 were plated on coverslips in a 24-well dish. The plate was centrifuged at 1500rpm for 5 minutes to allow cells to adhere. Cells were then fixed with 4% PFA and stained with anti-BrdU antibody as described above.

Real time-PCR

Cells were harvested with 0.5% trypsin-EDTA, centrifuged for 5 min at 2,000 rpm, and cell pellets frozen. Cell pellets were homogenized using a QIAshredder (Qiagen, Valencia, CA) and RNA was isolated using an RNeasy Mini Kit (Qiagen, Valencia, CA). Real time continuous detection of PCR product was achieved using Sybr Green (Applied Biosystems, Carlsbad, CA). GAPDH was used as an internal control with relative quantification being expressed as a ratio of the difference in the number of cycles needed for expression of a gene. Primers were designed using the Primer3 version 4.0.0. (Table S5).

Zymography

U87 glioma cells expressing the following EGFR mutations: Parental (non-transduced), WT (wild type EGFR over-expressed), V3 (EGFRvIII), V2 (EGFRvII, deletion from exon 14-15), R108K, G63R, A289V, A/R (double A289V + R108K), and G598V, were seeded at $1x10^6$ cells/10cm dish and serum starved for 24 hours. Conditioned media was collected and concentrated by centrifugation using Amicon Ultra Centrifugal Filters according to manufacturer's instructions (Ultracel - 10K, Millipore, Billerica, MA). Protein concentration was measured and 5ug was loaded onto a 7.5% acrylamide gel containing 0.1% gelatin for SDS-PAGE. The gel was washed in washing buffer (2.5% Triton X-100, 50mM Tris-HCl pH 7.5, 5mM $CaCl_2$, 1uM $ZnCl_2$) for 30 minutes twice, rinsed in incubation buffer (1% Triton X-100, Tris-HCl 50mM pH 7.5, 5mM $CaCl_2$, 1uM $ZnCl_2$) for 5 minutes and incubated in fresh incubation buffer for 24 hours at 37C with agitation. Following staining with Coomassie Brilliant Blue for 1 hour and decoloration with acetic acid, the gel was imaged using the Chemi-Doc MP Imaging System (Bio-Rad).

Quantification and Statistical Analysis

All population analyses were conducted using Stat 14.2 (Stata Corporation, College Station, TX). Time to event data were analyzed using Kaplan-Meier methods, and group differences were tested using the log-rank test. Other associations among binary or categorical variables were analyzed using contingency table methods, and tested using the chi-square statistic. Results from experiments are presented as mean values ± standard error of the mean (SEM). Statistical analyses were carried out by unpaired Student's t-test using GraphPad Prism® 5.01 software. P values < 0.05 were considered statistically significant. For the animal survival analysis, Kaplan–Meier curves were plotted and compared using the log rank test. Statistical details can be found in the figure legends.

Data and Software Availability

The software tool used for skull-stripping (i.e., MUSE (Doshi et al., 2016)) is available in www.med.upenn.edu/sbia/muse.html. The software tool used for co-registration (i.e., FLIRT (Jenkinson et al., 2002)) is available in: fsl.fmrib.ox.ac.uk. We developed the Cancer Imaging Phenomics Toolkit (CaPTk) (Davatzikos et al., 2018) to facilitate clinical translation of complex computational algorithms, without requiring computational background (e.g., identification of genetic mutation imaging signatures (Bakas et al., 2017a)). Specifically for this study, CaPTk was used for 1) initialization of seed-points required by GLISTRboost, 2) image smoothing, as well as 3) extracting the quantitative imaging features. The code source, as well as executable installers, of CaPTk are available in: www.med.upenn.edu/cbica/captk. Finally, our segmentation approach, GLISTRboost (Bakas et al., 2017b), is available for public use through CBICA's Image Processing Portal (IPP - ipp.cbica.upenn.edu), which allows users to perform data analysis using integrated algorithms, without any software installation, whilst using CBICA's High Performance Computing resources.

Animal MRIs were converted to the Meta file format for 3D volumetric analysis using the ITK-SNAP (www.itksnap.org) program. The total brain volume and volume of the T2 abnormality were determined (Yushkevich et al., 2006). The overlay maps were generated using ParaView (Hansen and Johnson, 2005).

KEY RESOURCES TABLE

REAGENT or RESOURCE	SOURCE	IDENTIFIER
Antibodies		
EGFR antibody	BD Biosciences	61007
Pan-phospho-Tyrosine HRP antibody	R&D Systems	HAM1676
p42/44 MAPK antibody	Cell Signaling Technology	9102
Phospho-p42/44 MAPK antibody	Cell Signaling Technology	9101
STAT3 antibody	Cell Signaling Technology	4904
Phospho-STAT3 y705 antibody	Cell Signaling Technology	9145
Akt antibody	Cell Signaling Technology	9272
Phospho-Akt s473	Cell Signaling Technology	4060
Ki67	Santa Cruz Biotechnology	Sc-15402
β-Actin	Sigma	A 3854
mAb806	Biological Production Facility	N/A
BrdU (clone B44) antibody	BD Biosciences	BDB347580
Hoechst 33258	Sigma-Aldrich	B2883
Bacterial and Virus Strains		
pLRNL vector	Nishikawa et al, 1994	N/A
pLV-EF1a-MCS-IRES-Hyg	Biosettia	cDNA-pLV02
iRFP720 cDNA	Shcherbakova et al, 2013	N/A
Biological Samples		
Chemicals, Peptides, and Recombinant Proteins		
U0126	LC Laboratories	U-6770
U0126	Cell Signaling Technology	9903S
PD98059	LC Laboratories	P-4313
Critical Commercial Assays		
Deposited Data		
Experimental Models: Cell Lines		
Human: U87 cells	ATCC	HTB-14
Human: HK281 GBM-spheres	Laboratory of Harley Kornblum, UCLA	N/A
Experimental Models: Organisms/Strains		
Mouse: Female NCI Ath/Nu	Charles River Labs	Strain 563
Mouse: Female J:NU Homozygous	The Jackson Laboratory	007850
Oligonucleotides		
shRNA targeting sequence: shMMP1: CCGGGCTAACCTTTGATGCTATAACCT CGAGGTTATAGCATCAAAGGTTAGCTT TTTG	Sigma	TRCN0000372933
shControl: pLKO.1shGFP2	Fenton, et al 2012	N/A
Primers for Real Time PCR, see Table S2	This paper	N/A
Recombinant DNA		
Software and Algorithms		
MUSE	Doshi, J., et al., 2016	www.med.upenn.edu/sbia/muse.html

FLIRT	Jenkinson, M. and S. Smith, 2001	fsl.fmrib.ox.ac.uk
Cancer Imaging Phenomics Toolkit (CaPTk)	Davatzikos, C., et al., (In Press)	www.med.upenn.edu/sbia/captk.html
GLISTRboost	Bakas, S., et al., GLISTRboost: Combining Multimodal MRI Segmentation, Registration, and Biophysical Tumor Growth Modeling with Gradient Boosting Machines for Glioma Segmentation, 2016	ipp.cbica.upenn.edu http://www.med.upenn.edu/sbia/glistrboost.html
ITK-SNAP	Yushkevich, P. A., et al., 2006	www.itksnap.org
ParaView	Hansen, C. D., et al., 2005	www.paraview.org
Other		

Figure 1

Click here to download Figure Figure 1.jpg

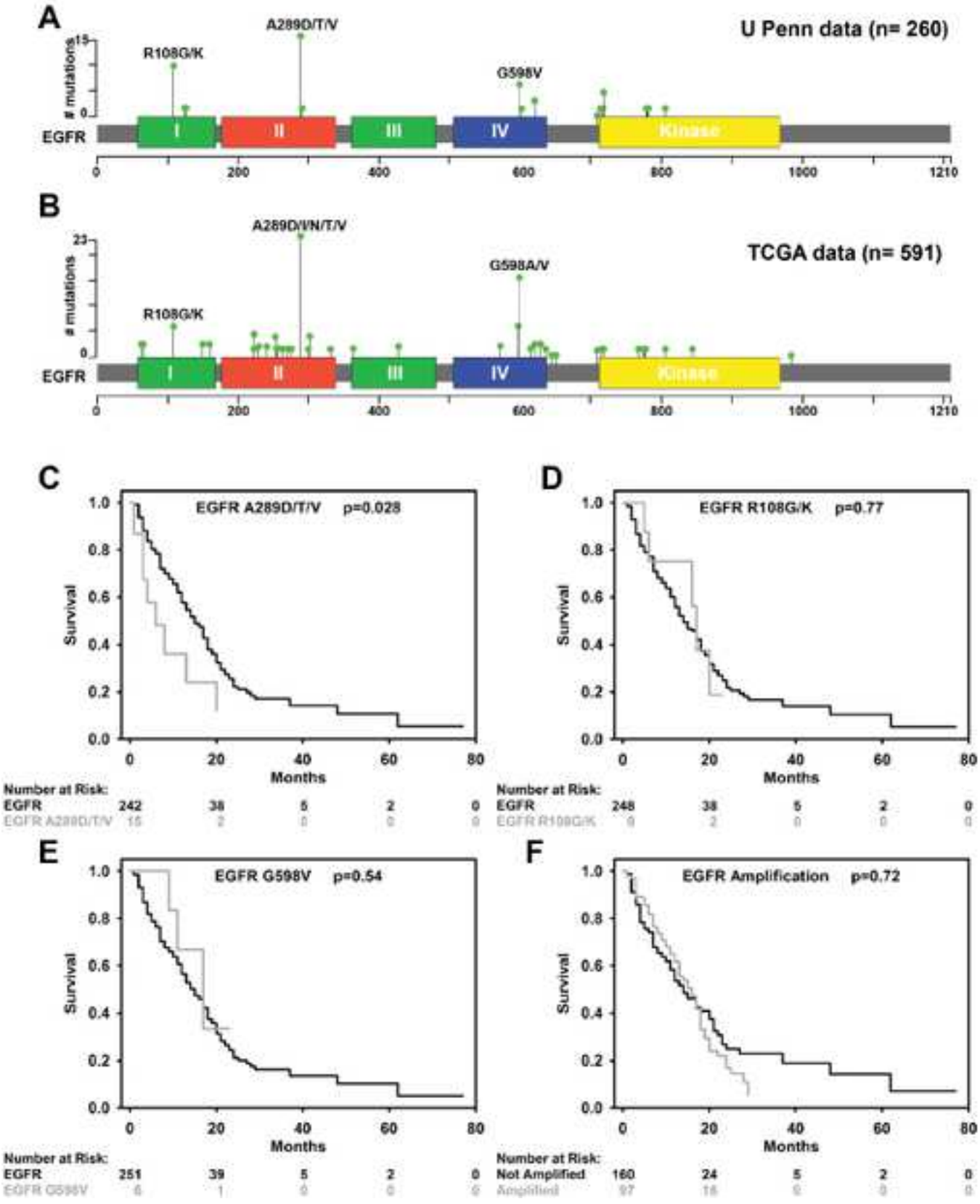

Figure 2

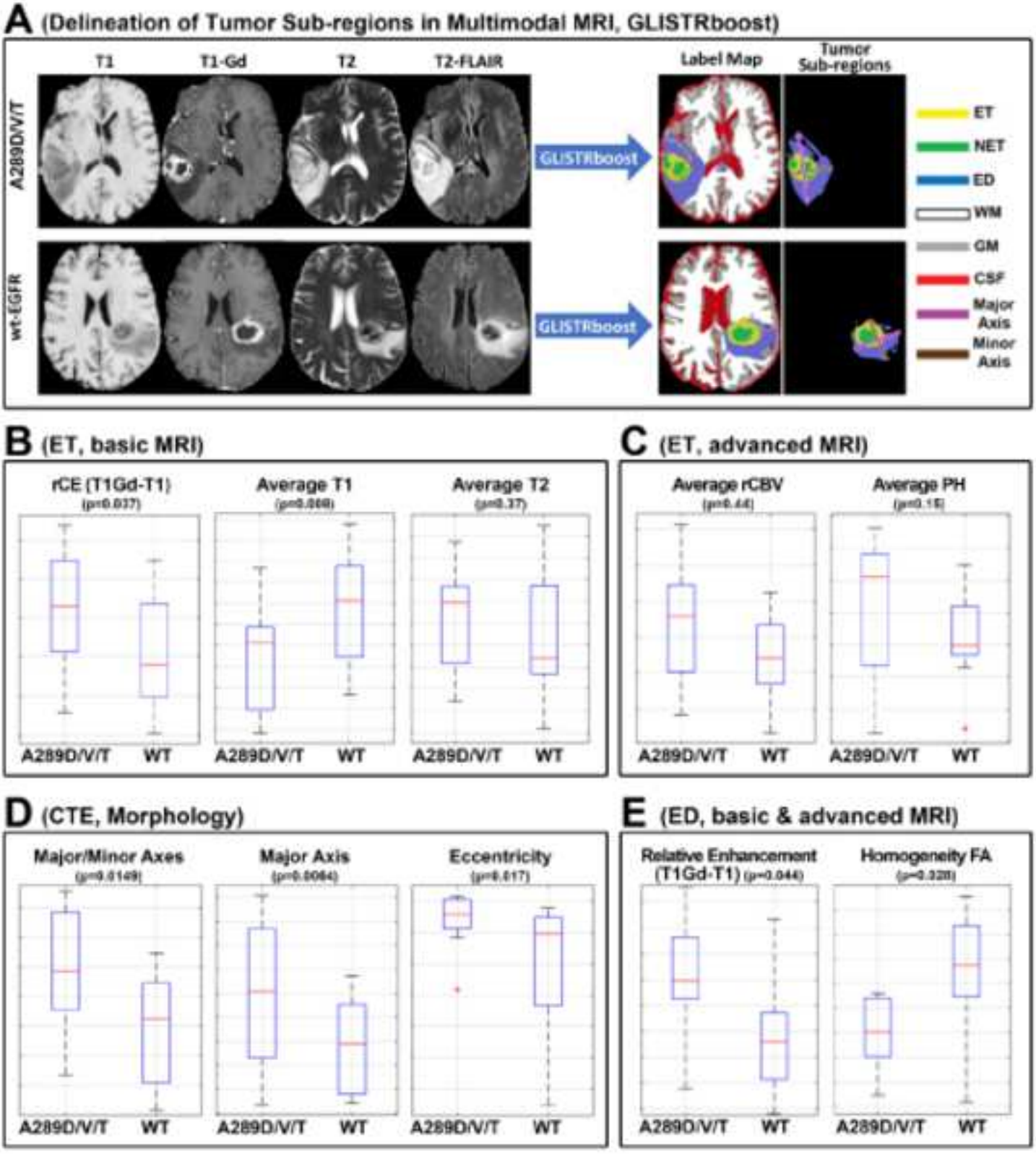

Figure 3

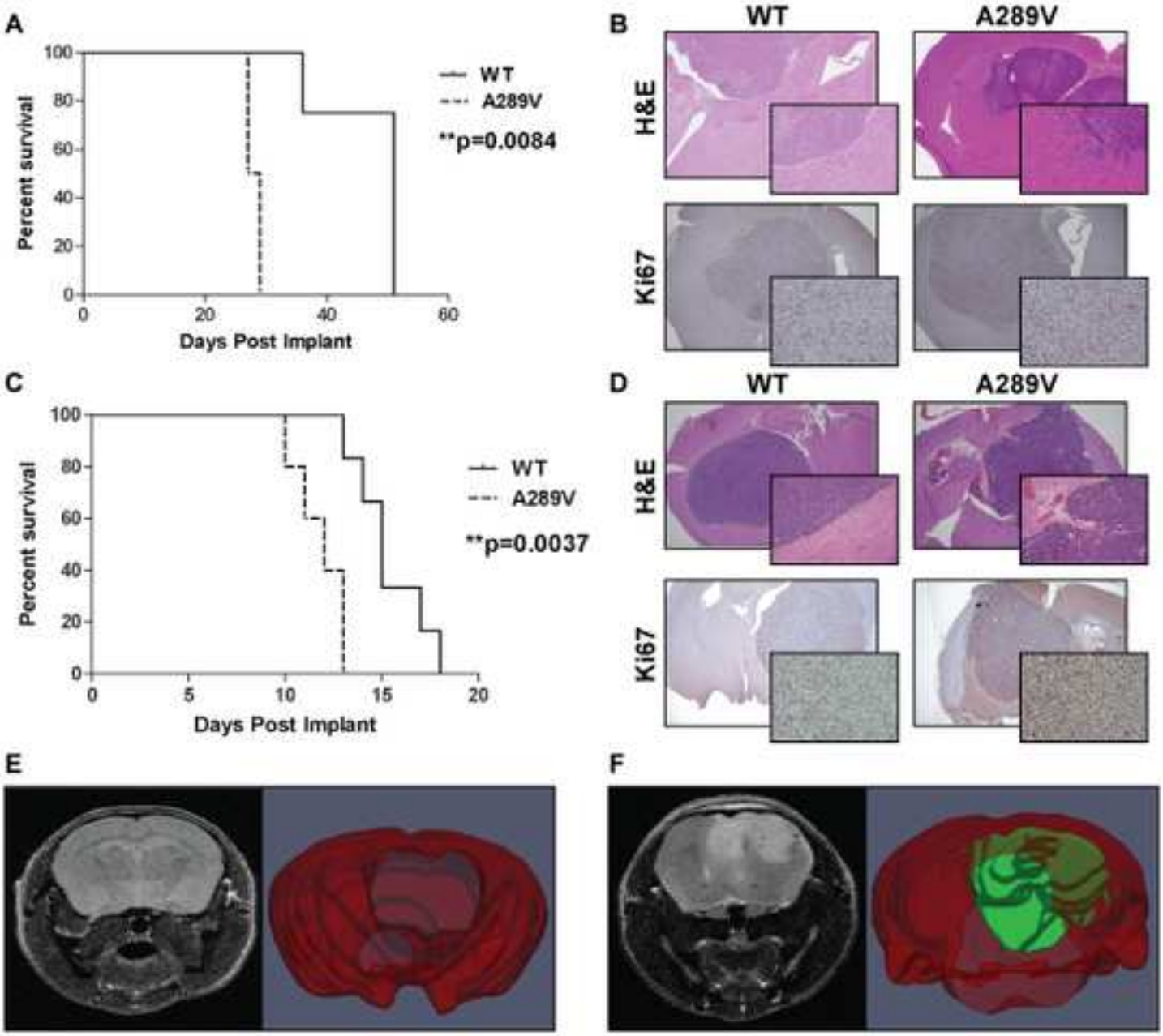

Figure 4

Click here to download Figure Figure 4.jpg

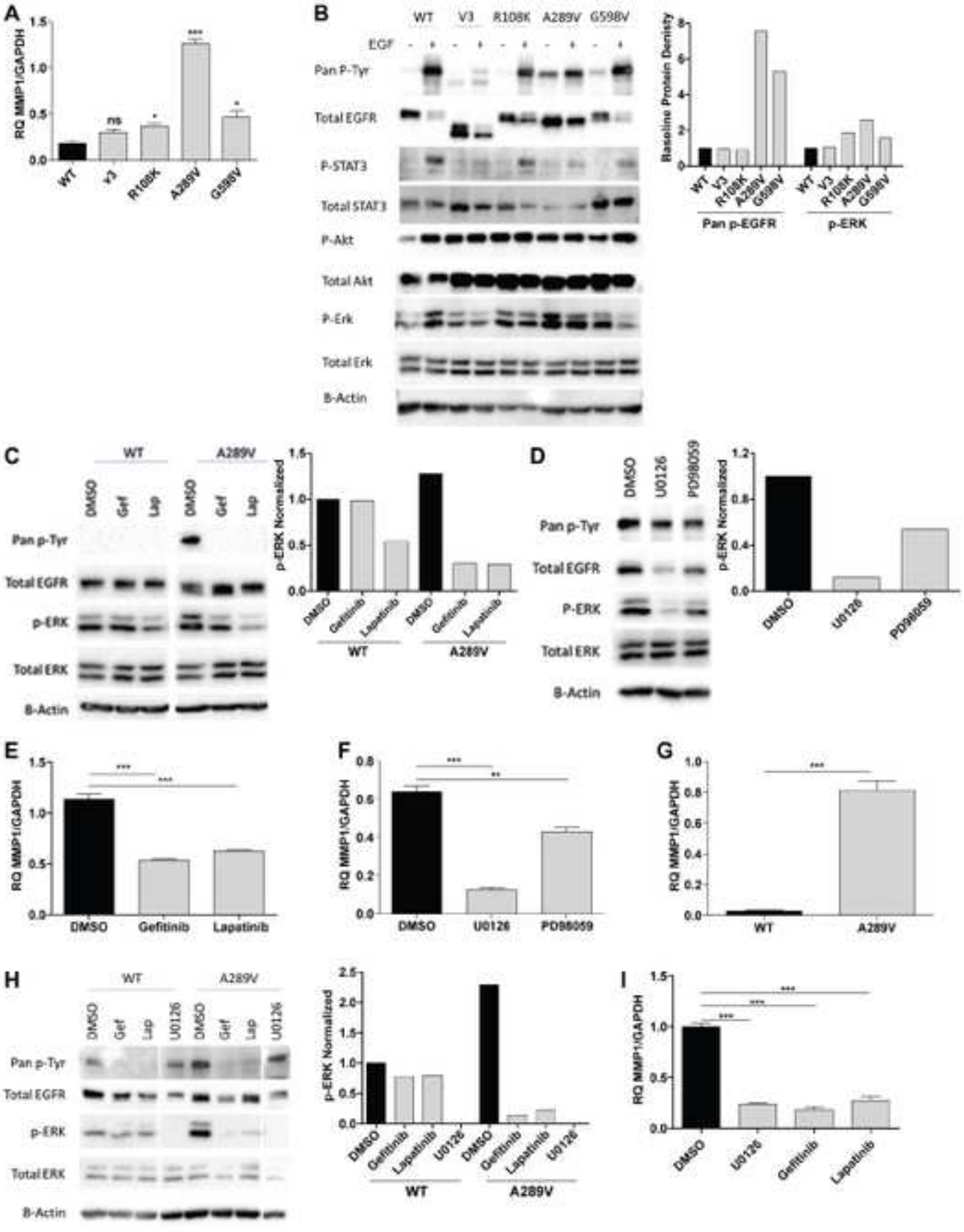

Figure 5

Click here to download Figure Figure 5.jpg

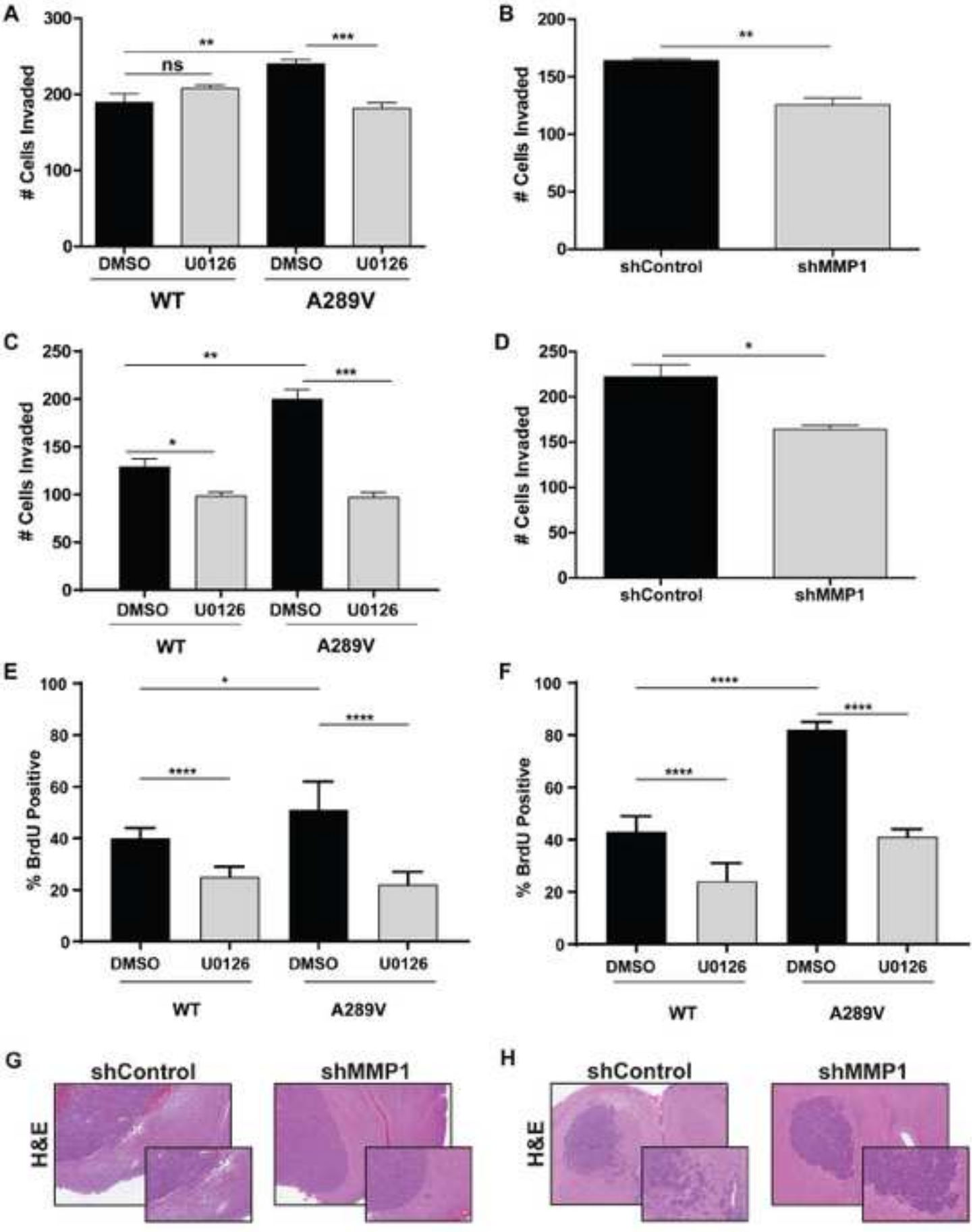

Figure 6

Click here to download Figure Figure 6.jpg

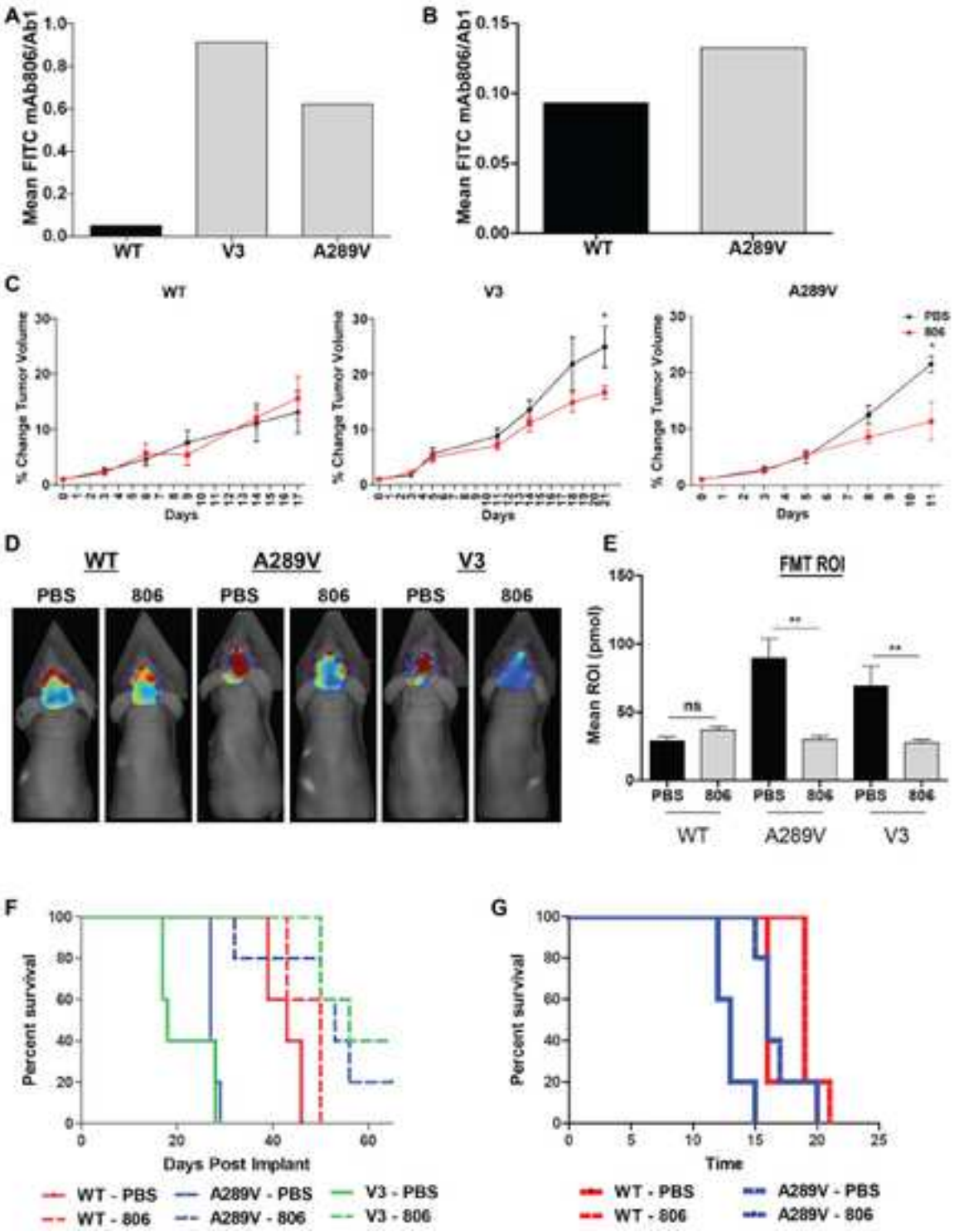

Variable		n	%
Gender	Female	103	40
	Male	157	60
Age	0-29	2	1
	30-49	26	10
	50-69	157	60
	70+	75	29
MGMT	Unmethylated	122	47
	Methylated	87	33
	Unknown	51	20
EGFR	Non-Amplified	162	62
	Amplified	98	38
EGFRvIII	Negative	154	59
	Postive	50	19
	Unknown	56	22
Misense Mutants	Ad289D/T/V	15	6
	R108G/K	9	3
	G598V	6	2

Supplementary Table 1: Patient demographics of the discovery GBM cohort at UPenn.

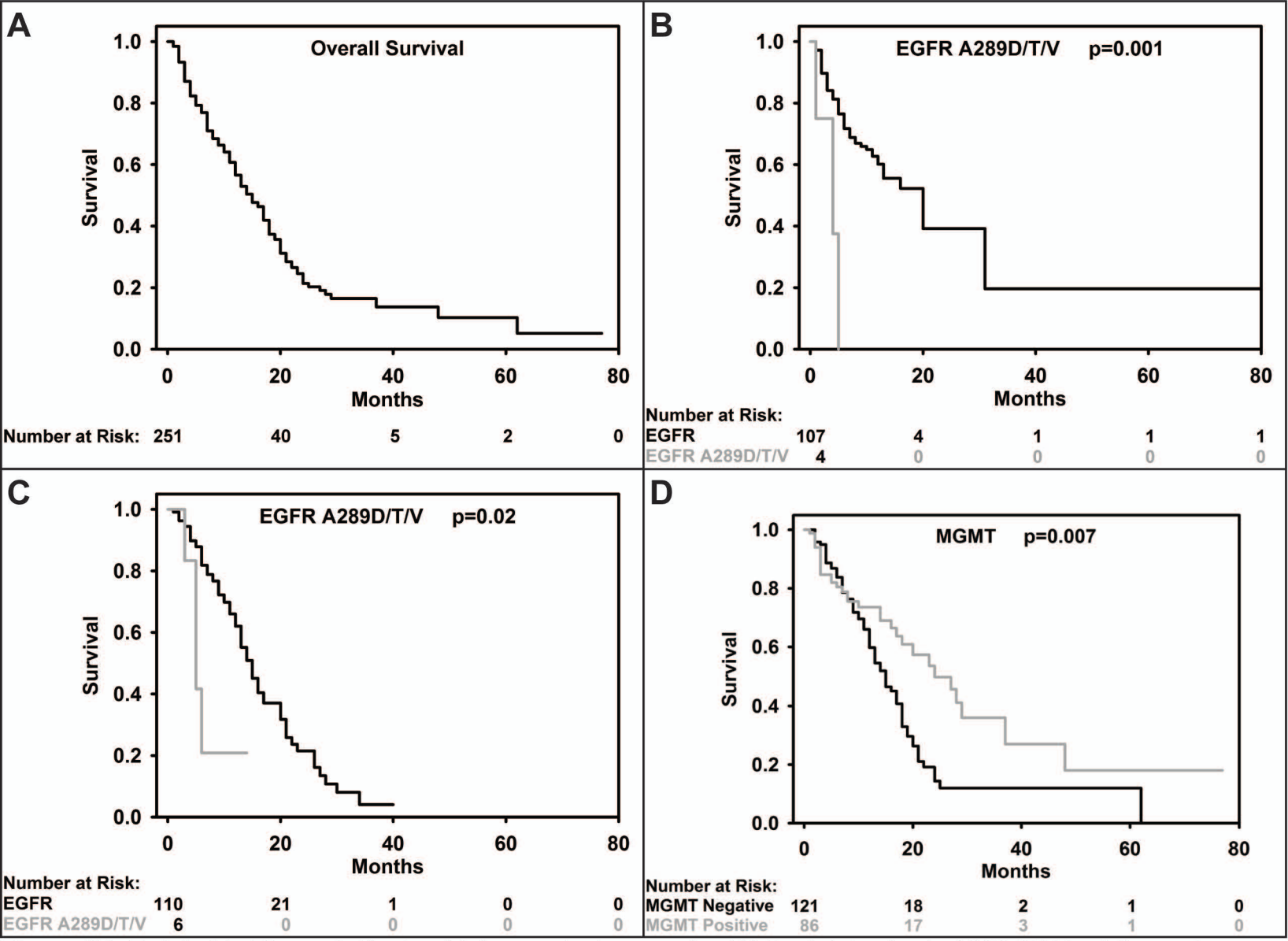

Figure S1. Related to Figure 1. Kaplan-Meier survival curves for (A) the total cohort of 260 IDH1 wildtype, de novo GBMs, (B) the validation UPenn cohort, (C) the validation French cohort, and (D) MGMT methylated versus MGMT unmethylated GBM patients.

EGFR alteration	Tumor sub-region	Feature Observation	*p*-value
A289D/T/V vs wt-EGFR	CTE	Major Axis	0.0064
A289D/T/V vs wt-EGFR	ET	GLSZM: Zone Percentage in T2 signal	0.0065
A289D/T/V vs wt-EGFR	ET	GLCM: Homogeneity in T2 signal	0.0068
A289D/T/V vs wt-EGFR	ET	Average T1 Signal	0.0081
A289D/T/V vs wt-EGFR	ET	Minor Axis	0.0085
A289D/T/V vs wt-EGFR	ET	GLSZM: Zone-Size Nonuniformity in T2 signal	0.0096
A289D/T/V vs wt-EGFR	ET	GLSZM: Small Zone Emphasis in T2 signal	0.0099
A289D/T/V vs wt-EGFR	ET	GLRLM: Run Length Non-uniformity in T2 signal	0.0112
A289D/T/V vs wt-EGFR	ET	GLCM: Dissimilarity in the T2 signal	0.0125
A289D/T/V vs wt-EGFR	ET	GLRLM: Short Run Emphasis in T2 signal	0.0129
A289D/T/V vs wt-EGFR	ET	Bin 4 of the T1 signal	0.0147
A289D/T/V vs wt-EGFR	CTE	Major/Minor Axis Ratio	0.0149
A289D/T/V vs wt-EGFR	ET	NGTDM: Contrast in T2 signal	0.0161
A289D/T/V vs wt-EGFR	CTE	Eccentricity	0.0176
A289D/T/V vs wt-EGFR	ET	GLRLM: Run Percentage in T2 signal	0.0212
A289D/T/V vs wt-EGFR	NET	GLCM: Contrast in T2 signal	0.0218
A289D/T/V vs wt-EGFR	ET	NGTDM: Complexity in T2 signal	0.0224
A289D/T/V vs wt-EGFR	NET	Relative Enhancement (T1Gd - T1)	0.0236
A289D/T/V vs wt-EGFR	ET	GLCM: Contrast in T2 signal	0.0256
A289D/T/V vs wt-EGFR	NET	GLCM: Dissimilarity in T2 signal	0.0262
A289D/T/V vs wt-EGFR	ED	GLCM: Homogeneity in the Fractional Anisotropy signal	0.0283
A289D/T/V vs wt-EGFR	NET	Standard deviation of the Peak Height signal	0.0309
A289D/T/V vs wt-EGFR	ET	GLCM: Correlation in T2 signal	0.0325
A289D/T/V vs wt-EGFR	NET	Average T1 signal	0.0331
A289D/T/V vs wt-EGFR	ET	Relative Enhancement (T1Gd - T1)	0.0374
A289D/T/V vs wt-EGFR	ED	Bin 1 of Local Binary Patterns in T2-FLAIR signal	0.0377
A289D/T/V vs wt-EGFR	NET	GLCM: Homogeneity in T2 signal	0.0429
A289D/T/V vs wt-EGFR	ED	Relative Enhancement (T1Gd - T1)	0.0441
A289D/T/V vs wt-EGFR	NET	GLCM: Correlation in T2 signal	0.0455
A289D/T/V vs wt-EGFR	NET	Bin 4 of the T1Gd signal	0.0479
R108G/K vs wt-EGFR	ET	Bin 4 of Peak Height signal	0.0107
R108G/K vs wt-EGFR	ED	Standard deviation of T1Gd signal	0.0145
R108G/K vs wt-EGFR	NET	Bin 4 of Peak Height signal	0.0149
R108G/K vs wt-EGFR	NET	Bin 5 of Percentage Signal Recovery signal	0.0154
R108G/K vs wt-EGFR	ED	Bin 1 of Local Binary Patterns RAD Bin1	0.0169
R108G/K vs wt-EGFR	NET	Bin 5 of Peak Height signal	0.0181
R108G/K vs wt-EGFR	ET	GLRLM: High Grey-Level Run Emphasis in T2 signal	0.0189
R108G/K vs wt-EGFR	ET	GLRLM: Short Run High Grey-Level Emphasis in T2 signal	0.0196
R108G/K vs wt-EGFR	ET	Skewness in T2 signal	0.0237
R108G/K vs wt-EGFR	ET	Average Peak Height signal	0.0275
R108G/K vs wt-EGFR	NET	Average Percentage Signal Recovery signal	0.0279
R108G/K vs wt-EGFR	ED	Solidity	0.0284
R108G/K vs wt-EGFR	NET	GLCM: Dissimilarity in T2 signal	0.0289
R108G/K vs wt-EGFR	NET	GLCM: Contrast in T2 signal	0.0295
R108G/K vs wt-EGFR	NET	GLCM: Correlation in T2 signal	0.0302
R108G/K vs wt-EGFR	ET	Bin 5 of Local Binary Patterns in Radial Diffusivity signal	0.0319
R108G/K vs wt-EGFR	NET	GLCM: Homogeneity in T1 signal	0.0332
R108G/K vs wt-EGFR	ET	GLRLM: Grey Level Non-uniformity in T2 signal	0.0347

R108G/K vs wt-EGFR	NET	GLSZM: Zone-Size Nonuniformity in T2 signal	0.0372
R108G/K vs wt-EGFR	NET	NGTDM: Contrast in T2 signal	0.0372
R108G/K vs wt-EGFR	ET	GLRLM: Long Run High Grey-Level Emphasis in T2 signal	0.0388
R108G/K vs wt-EGFR	NET	GLCM: Entropy in T2 signal	0.0393
R108G/K vs wt-EGFR	NET	Bin 3 of Percentage Signal Recovery signal	0.0423
R108G/K vs wt-EGFR	NET	Solidity	0.0429
R108G/K vs wt-EGFR	NET	GLSZM: Small Zone Emphasis in T2 signal	0.0431
R108G/K vs wt-EGFR	ED	GLRLM: Run Percentage in T2-FLAIR signal	0.0436
R108G/K vs wt-EGFR	ET	GLSZM: High Grey-Level Zone Emphasis in T2 signal	0.0438
R108G/K vs wt-EGFR	ED	GLRLM: Long Run Emphasis in T2-FLAIR signal	0.044
R108G/K vs wt-EGFR	ET	GLRLM: Grey Level Non-uniformity in T1 signal	0.0444
R108G/K vs wt-EGFR	ET	NGTDM: Complexity in T1Gd signal	0.0447
R108G/K vs wt-EGFR	NET	Bin 4 of relative Cerebral Blood Volume signal	0.0448
R108G/K vs wt-EGFR	ET	Correlation in T1Gd signal	0.0455
R108G/K vs wt-EGFR	NET	Average Peak Height signal	0.0458
R108G/K vs wt-EGFR	ED	Bin 1 of Local Binary Patterns in Apparent Diffusion Coefficient signal	0.0459
R108G/K vs wt-EGFR	NET	NGTDM: Complexity in T2 signal	0.0473
R108G/K vs wt-EGFR	ET	GLCM: Variance in T2 signal	0.0477
R108G/K vs wt-EGFR	NET	Standard deviation of Peak Height signal	0.0485
R108G/K vs wt-EGFR	ED	Homogeneity of Fractional Anisotropy signal	0.0487
R108G/K vs wt-EGFR	ED	Bin 3 of T1Gd signal	0.0488
R108G/K vs wt-EGFR	ED	GLRLM: Short Run Emphasis in T2-FLAIR signal	0.0493
R108G/K vs wt-EGFR	NET	GLCM: Homogeneity in T2 signal	0.0497
G598V vs wt-EGFR	ED	Relative Enhancement (T1Gd - T1)	0.00264
G598V vs wt-EGFR	ET	Bin 2 of T1 signal	0.0032
G598V vs wt-EGFR	ET	Bin 2 of T2-FLAIR signal	0.00432
G598V vs wt-EGFR	ED	Average T1 signal	0.00456
G598V vs wt-EGFR	NET	Bin 2 of T1 signal	0.00549
G598V vs wt-EGFR	ED	Bin 2 of T1 signal	0.00627
G598V vs wt-EGFR	NET	Bin 5 of T1Gd signal	0.00702
G598V vs wt-EGFR	NET	Bin 4 of T1Gd signal	0.00776
G598V vs wt-EGFR	ET	GLRLM: Run Length Non-uniformity in T2 signal	0.00999
G598V vs wt-EGFR	ET	GLRLM: Short Run Emphasis in T2 signal	0.0101
G598V vs wt-EGFR	ET	Average T1 signal	0.01253
G598V vs wt-EGFR	ET	GLRLM: Run Percentage in T2 signal	0.01898
G598V vs wt-EGFR	ED	Bin 4 of T2-FLAIR signal	0.0198
G598V vs wt-EGFR	ET	Bin 1 of T2-FLAIR signal	0.02065
G598V vs wt-EGFR	ET	Skewness of T1 signal	0.02103
G598V vs wt-EGFR	ET	GLRLM: Long Run Low Grey-Level Emphasis in T1 signal	0.02282
G598V vs wt-EGFR	ET	Average T2-FLAIR signal	0.02326
G598V vs wt-EGFR	ED	Bin 3 of T1Gd signal	0.02409
G598V vs wt-EGFR	NET	GLCM: Entropy in T1Gd signal	0.02647
G598V vs wt-EGFR	ED	Bin 2 of Local Binary Patterns in T2-FLAIR signal	0.02924
G598V vs wt-EGFR	ED	GLSZM: Low Grey-Level Zone Emphasis in T1Gd signal	0.02962
G598V vs wt-EGFR	NET	GLCM: Energy in T1Gd signal	0.03009
G598V vs wt-EGFR	ET	GLCM: SumAverage in T1 signal	0.03043
G598V vs wt-EGFR	ET	GLSZM: Zone Percentage in T2 signal	0.03173
G598V vs wt-EGFR	ET	Relative Enhancement (T1Gd - T1)	0.03262
G598V vs wt-EGFR	ET	Bin 4 of T2-FLAIR signal	0.03359
G598V vs wt-EGFR	ED	Bin 3 of T2-FLAIR signal	0.03495

G598V vs wt-EGFR	ED	Bin 1 of T1 signal	0.03848
G598V vs wt-EGFR	NET	GLSZM: Gray-Level Nonuniformity in T1Gd signal	0.03859
G598V vs wt-EGFR	ET	GLRLM: Long Run Emphasis in T2 signal	0.0403
G598V vs wt-EGFR	ED	Correlation in T2-FLAIR signal	0.04048
G598V vs wt-EGFR	ET	GLCM: Energy in T1 signal	0.04134
G598V vs wt-EGFR	NET	GLCM: Homogeneity in T1Gd signal	0.0439
G598V vs wt-EGFR	ED	GLSZM: Short Zone Low Grey-Level Emphasis in T1Gd signal	0.04669
G598V vs wt-EGFR	NET	Average T1 signal	0.04848
A289D/T/V vs G598V	ET	Bin 4 of T2-FLAIR signal	0.00829
A289D/T/V vs G598V	ET	Bin 3 of T2-FLAIR signal	0.00932
A289D/T/V vs G598V	ED	Standard deviation of T2-FLAIR signal	0.01028
A289D/T/V vs G598V	ET	Extent	0.01034
A289D/T/V vs G598V	NET	Bin 5 of T1Gd signal	0.01083
A289D/T/V vs G598V	NET	GLSZM: Gray-Level Nonuniformity in T1Gd signal	0.01285
A289D/T/V vs G598V	ED	Bin 2 of T1 signal	0.01943
A289D/T/V vs G598V	ED	Skewness of T1Gd signal	0.01951
A289D/T/V vs G598V	ED	Bin 4 of T2-FLAIR signal	0.02063
A289D/T/V vs G598V	ED	Homogeneity in T2-FLAIR signal	0.02078
A289D/T/V vs G598V	ET	Bin 3 of relative Cerebral Blood Volume signal	0.0235
A289D/T/V vs G598V	ET	GLCM: Correlation in T2-FLAIR signal	0.0262
A289D/T/V vs G598V	ET	GLSZM: Large Zone Emphasis in T1Gd signal	0.02878
A289D/T/V vs G598V	NET	Correlation in Radial Diffusivity signal	0.03051
A289D/T/V vs G598V	ED	Standard deviation on relative Cerebral Blood Volume signal	0.03247
A289D/T/V vs G598V	NET	Bin 4 of Local Binary Patterns in T2-FLAIR signal	0.03673
A289D/T/V vs G598V	ET	Skewness of T1 signal	0.03848
A289D/T/V vs G598V	ET	GLRLM: Long Run Emphasis in T1Gd signal	0.03924
A289D/T/V vs G598V	ET	Solidity	0.0396
A289D/T/V vs G598V	ED	Standard deviation of T1 signal	0.03993
A289D/T/V vs G598V	ET	Average relative Cerebral Blood Volume signal	0.04217
A289D/T/V vs G598V	ED	Relative Enhancement (T1Gd - T1)	0.04316
A289D/T/V vs G598V	ED	GLRLM: Long Run Low Grey-Level Emphasis in T1Gd signal	0.04351
A289D/T/V vs G598V	ED	Average T2-FLAIR signal	0.04371
A289D/T/V vs G598V	ET	GLSZM: Long Zone High Grey-Level Emphasis in T1Gd signal	0.04389
A289D/T/V vs G598V	ET	GLCM: Correlation in T2 signal	0.04589
A289D/T/V vs G598V	NET	Correlation in T2 signal	0.04604
A289D/T/V vs G598V	ED	Homogeneity in T2 signal	0.04657
A289D/T/V vs G598V	ED	Bin 5 of T2-FLAIR signal	0.04693
A289D/T/V vs G598V	NET	Bin 1 of Peak Height signal	0.04917
A289D/T/V vs G598V	ET	Bin 4 of relative Cerebral Blood Volume signal	0.04987
A289D/T/V vs R108G/K	ET	GLRLM: Long Run High Grey-Level Emphasis in T2 signal	0.00045
A289D/T/V vs R108G/K	NET	Bin 4 of Peak Height signal	0.00054
A289D/T/V vs R108G/K	ET	GLCM: Homogeneity in T2-FLAIR signal	0.00081
A289D/T/V vs R108G/K	ET	GLRLM: Run Length Non-uniformity in T2-FLAIR signal	0.00085
A289D/T/V vs R108G/K	ET	GLRLM: Run Percentage in T2-FLAIR signal	0.00095
A289D/T/V vs R108G/K	ET	GLRLM: Short Run Emphasis in T2-FLAIR signal	0.00102
A289D/T/V vs R108G/K	ET	GLRLM: Long Run High Grey-Level Emphasis in T2-FLAIR signal	0.00116
A289D/T/V vs R108G/K	ET	GLRLM: Long Run Emphasis in T2-FLAIR signal	0.00179
A289D/T/V vs R108G/K	ET	GLCM: Homogeneity in T2 signal	0.00242
A289D/T/V vs R108G/K	ET	GLCM: Correlation in T2-FLAIR signal	0.00242
A289D/T/V vs R108G/K	ET	GLRLM: Run Percentage in T2 signal	0.00254

A289D/T/V vs R108G/K	ET	GLSZM: Long Zone High Grey-Level Emphasis in T2-FLAIR signal	0.00281
A289D/T/V vs R108G/K	NET	Average T1 signal	0.00292
A289D/T/V vs R108G/K	ET	GLSZM: Zone Percentage in T2-FLAIR signal	0.00305
A289D/T/V vs R108G/K	ET	GLRLM: Long Run Emphasis in T2 signal	0.00355
A289D/T/V vs R108G/K	ET	GLCM: Correlation in T1Gd signal	0.00377
A289D/T/V vs R108G/K	ET	GLCM: Correlation in T1 signal	0.00423
A289D/T/V vs R108G/K	ET	GLRLM: Short Run Emphasis in T2 signal	0.00441
A289D/T/V vs R108G/K	ET	GLCM: Homogeneity in T1Gd signal	0.00444
A289D/T/V vs R108G/K	ET	NGTDM: Complexity in T1Gd signal	0.00488
A289D/T/V vs R108G/K	ED	Bin 5 of Peak Height signal	0.00509
A289D/T/V vs R108G/K	ET	NGTDM: Contrast in T1Gd signal	0.00544
A289D/T/V vs R108G/K	ET	Standard deviation of T2 signal	0.00555
A289D/T/V vs R108G/K	ET	GLRLM: Run Length Non-uniformity in T2 signal	0.00562
A289D/T/V vs R108G/K	ET	GLCM: Dissimilarity in T1Gd signal	0.00571
A289D/T/V vs R108G/K	ET	GLCM: AutoCorrelation in T2-FLAIR signal	0.00576
A289D/T/V vs R108G/K	ET	GLRLM: High Grey-Level Run Emphasis in T2 signal	0.006
A289D/T/V vs R108G/K	ET	GLRLM: Gray-Level Nonuniformity in T2 signal	0.00638
A289D/T/V vs R108G/K	ET	Correlation in T1Gd signal	0.0064
A289D/T/V vs R108G/K	ET	GLCM: Contrast in T1Gd signal	0.00711
A289D/T/V vs R108G/K	ET	GLCM: Correlation in T2 signal	0.00744
A289D/T/V vs R108G/K	ET	GLCM: Variance in T2 signal	0.00759
A289D/T/V vs R108G/K	ET	GLRLM: Gray-Level Variance in T1Gd signal	0.00798
A289D/T/V vs R108G/K	ET	GLCM: AutoCorrelation in T2 signal	0.00808
A289D/T/V vs R108G/K	ED	Correlation in T2 signal	0.00855
A289D/T/V vs R108G/K	ET	GLCM: SumAverage in T2-FLAIR signal	0.0089
A289D/T/V vs R108G/K	ET	GLCM: SumAverage in T2 signal	0.00904
A289D/T/V vs R108G/K	ET	GLRLM: Short Run High Grey-Level Emphasis in T2 signal	0.00986
A289D/T/V vs R108G/K	ET	Solidity	0.01032
A289D/T/V vs R108G/K	ET	Skewness of T2 signal	0.01071
A289D/T/V vs R108G/K	ET	GLCM: Dissimilarity in T2-FLAIR signal	0.01073
A289D/T/V vs R108G/K	ET	GLCM: Variance in T2-FLAIR signal	0.01084
A289D/T/V vs R108G/K	ET	Bin 5 of Local Binary Patterns in Radial Diffusivity signal	0.01149
A289D/T/V vs R108G/K	ET	Kurtosis of T2-FLAIR signal	0.01175
A289D/T/V vs R108G/K	ET	Average Percentage Signal Recovery signal	0.01181
A289D/T/V vs R108G/K	ET	Bin 4 of Peak Height signal	0.01199
A289D/T/V vs R108G/K	ET	GLRLM: High Grey-Level Run Emphasis in T2-FLAIR signal	0.012
A289D/T/V vs R108G/K	ED	Bin 3 of T2-FLAIR signal	0.01381
A289D/T/V vs R108G/K	NET	Average Peak Height signal	0.01537
A289D/T/V vs R108G/K	ET	GLRLM: Long Run Emphasis in T1Gd signal	0.01658
A289D/T/V vs R108G/K	ET	GLCM: Variance in T1 signal	0.01677
A289D/T/V vs R108G/K	ET	GLRLM: Run Percentage in T1Gd signal	0.01749
A289D/T/V vs R108G/K	ET	NGTDM: Contrast in T2-FLAIR signal	0.01895
A289D/T/V vs R108G/K	ET	GLRLM: Long Run High Grey-Level Emphasis in T1 signal	0.019
A289D/T/V vs R108G/K	ET	Bin 5 pf Local Binary Patterns in Fractional Anisotropy signal	0.01954
A289D/T/V vs R108G/K	ET	Homogeneity in T1Gd signal	0.01964
A289D/T/V vs R108G/K	ED	Bin 4 of Peak Height signal	0.01991
A289D/T/V vs R108G/K	ET	Kurtosis of T2 signal	0.02006
A289D/T/V vs R108G/K	ET	GLRLM: Short Run Emphasis in T1Gd signal	0.02014
A289D/T/V vs R108G/K	ET	GLRLM: Run Length Non-uniformity in T1Gd signal	0.02046
A289D/T/V vs R108G/K	ET	Correlation in T1 signal	0.02125

A289D/T/V vs R108G/K	ET	GLSZM: Zone Percentage in T2 signal	0.02214
A289D/T/V vs R108G/K	NET	Bin 2 of Peak Height signal	0.02253
A289D/T/V vs R108G/K	ED	Bin 5 of relative Cerebral Blood Volume	0.02317
A289D/T/V vs R108G/K	ET	Variance in T2 signal	0.02322
A289D/T/V vs R108G/K	ET	NGTDM: Contrast in T2 signal	0.02383
A289D/T/V vs R108G/K	ET	Kurtosis in T1Gd signal	0.02418
A289D/T/V vs R108G/K	NET	Bin 5 of T1 signal	0.02443
A289D/T/V vs R108G/K	ET	Bin 5 of Peak Height signal	0.02481
A289D/T/V vs R108G/K	ET	Average Peak Height signal	0.02532
A289D/T/V vs R108G/K	ET	Variance in T1 signal	0.02572
A289D/T/V vs R108G/K	ET	Skewness in T2-FLAIR signal	0.02578
A289D/T/V vs R108G/K	ET	GLRLM: Short Run High Grey-Level Emphasis in T2-FLAIR signal	0.02632
A289D/T/V vs R108G/K	ED	GLSZM: Short Zone Low Grey-Level Emphasis in T2-FLAIR signal	0.02641
A289D/T/V vs R108G/K	ET	Average T2-FLAIR signal	0.02757
A289D/T/V vs R108G/K	ET	GLSZM: High Grey-Level Zone Emphasis in T2 signal	0.02763
A289D/T/V vs R108G/K	ET	GLRLM: Short Run Low Grey-Level Emphasis in T1 signal	0.02801
A289D/T/V vs R108G/K	ET	GLSZM: Low Grey-Level Zone Emphasis in T1 signal	0.0285
A289D/T/V vs R108G/K	ET	Variance in T2-FLAIR signal	0.02858
A289D/T/V vs R108G/K	ED	Average Peak Height signal	0.02899
A289D/T/V vs R108G/K	ET	GLRLM: High Grey-Level Run Emphasis in T1 signal	0.02956
A289D/T/V vs R108G/K	ET	Bin 2 of Percentage Signal Recovery signal	0.02992
A289D/T/V vs R108G/K	ED	Bin 5 of T1Gd signal	0.03
A289D/T/V vs R108G/K	NET	Bin 3 of T2-FLAIR signal	0.03078
A289D/T/V vs R108G/K	NET	Bin 2 of T2 signal	0.03124
A289D/T/V vs R108G/K	ET	GLRLM: Low Grey-Level Run Emphasis in T1 signal	0.0315
A289D/T/V vs R108G/K	ET	Bin 4 of Percentage Signal Recovery signal	0.03182
A289D/T/V vs R108G/K	NET	Bin 4 of Local Binary Patterns in Fractional Anisotropy signal	0.03301
A289D/T/V vs R108G/K	ET	Bin 5 of Local Binary Patterns in T1Gd signal	0.03317
A289D/T/V vs R108G/K	ET	GLRLM: Short Run High Grey-Level Emphasis in T1 signal	0.03341
A289D/T/V vs R108G/K	ET	GLSZM: High Grey-Level Zone Emphasis in T1 signal	0.03437
A289D/T/V vs R108G/K	ET	Kurtosis in T1 signal	0.03441
A289D/T/V vs R108G/K	ET	Correlation in T2 signal	0.03459
A289D/T/V vs R108G/K	ET	GLSZM: Gray-Level Nonuniformity in T2 signal	0.03559
A289D/T/V vs R108G/K	ET	GLRLM: Gray-Level Nonuniformity in T2-FLAIR signal	0.03565
A289D/T/V vs R108G/K	ED	Bin 1 of Peak Height signal	0.03715
A289D/T/V vs R108G/K	ED	Homogeneity in T2 signal	0.03828
A289D/T/V vs R108G/K	ET	GLSZM: Zone Percentage in T1Gd signal	0.03843
A289D/T/V vs R108G/K	ED	Bin 4 of relative Cerebral Blood Volume signal	0.03889
A289D/T/V vs R108G/K	ED	GLSZM: Low Grey-Level Zone Emphasis in T2-FLAIR signal	0.03925
A289D/T/V vs R108G/K	ET	GLSZM: Large Zone Emphasis in T1 signal	0.04032
A289D/T/V vs R108G/K	ET	Bin 3 of relative Cerebral Blood Volume signal	0.04032
A289D/T/V vs R108G/K	ET	GLRLM: Long Run Emphasis in T1 signal	0.04247
A289D/T/V vs R108G/K	NET	Bin 3 of Percentage Signal Recovery signal	0.04256
A289D/T/V vs R108G/K	ET	Bin 5 of T2-FLAIR signal	0.04275
A289D/T/V vs R108G/K	ET	GLSZM: Short Zone High Grey-Level Emphasis in T1Gd signal	0.04287
A289D/T/V vs R108G/K	NET	NGTDM: Complexity in T2-FLAIR signal	0.04313
A289D/T/V vs R108G/K	ET	GLSZM: Short Zone High Grey-Level Emphasis in T1 signal	0.04399
A289D/T/V vs R108G/K	ET	GLCM: Contrast in T2-FLAIR signal	0.04568
A289D/T/V vs R108G/K	ET	GLRLM: Gray-Level Nonuniformity in T1 signal	0.04596
A289D/T/V vs R108G/K	NET	Standard deviation of T1 signal	0.04629

A289D/T/V vs R108G/K	NET	Average of Percentage Signal Recovery signal	0.04741
A289D/T/V vs R108G/K	ET	GLSZM: Gray-Level Nonuniformity in T1 signal	0.04769
A289D/T/V vs R108G/K	NET	Relative Enhancement (T1Gd - T1)	0.04784
A289D/T/V vs R108G/K	ED	Average relative Cerebral Blood Volume signal	0.04835
A289D/T/V vs R108G/K	NET	Average T1 signal	0.0495
R108G/K vs G598V	ET	Bin 4 of Peak Height signal	0.0089
R108G/K vs G598V	ET	Correlation in Radial Diffusivity signal	0.01539
R108G/K vs G598V	ED	Bin 2 of Fractional Anisotropy signal	0.01604
R108G/K vs G598V	ET	Bin 5 of Local Binary Patterns in T2-FLAIR signal	0.01762
R108G/K vs G598V	ET	Average Peak Height signal	0.01782
R108G/K vs G598V	NET	Solidity	0.01858
R108G/K vs G598V	ET	Bin 3 of relative Cerebral Blood Volume signal	0.01891
R108G/K vs G598V	ET	Bin 2 of T1 signal	0.01916
R108G/K vs G598V	ET	Standard deviation of Percent Signal Recovery signal	0.01926
R108G/K vs G598V	ED	Bin 3 of Local Binary Patterns in T2 signal	0.0195
R108G/K vs G598V	ET	Bin 1 of Local Binary Patterns in T2-FLAIR signal	0.02001
R108G/K vs G598V	NET	Bin 2 of T1 signal	0.02165
R108G/K vs G598V	ET	Bin 4 of T2-FLAIR signal	0.0222
R108G/K vs G598V	ED	Bin 2 of T1 signal	0.02237
R108G/K vs G598V	NET	Correlation in Radial Diffusivity signal	0.02553
R108G/K vs G598V	ET	Average T2-FLAIR	0.02646
R108G/K vs G598V	ED	Standard deviation of Peak Height signal	0.02678
R108G/K vs G598V	ET	GLSZM: Long Zone Low Grey-Level Emphasis in T2 signal	0.0287
R108G/K vs G598V	ED	Standard deviation of T2-FLAIR signal	0.03076
R108G/K vs G598V	ED	Standard deviation of relative Cerebral Blood Volume signal	0.03123
R108G/K vs G598V	NET	Correlation in Apparent Diffusion Coefficient signal	0.03335
R108G/K vs G598V	ED	Bin 5 of T2-FLAIR signal	0.03358
R108G/K vs G598V	ET	Bin 3 of T2-FLAIR signal	0.03419
R108G/K vs G598V	ED	Average T2-FLAIR signal	0.03564
R108G/K vs G598V	ET	Bin 5 of Local Binary Patterns in Radial Diffusivity signal	0.036
R108G/K vs G598V	ET	Bin 2 of T2-FLAIR signal	0.03656
R108G/K vs G598V	ET	Bin 1 of Local Binary Patterns in Fractional Anisotropy signal	0.03794
R108G/K vs G598V	NET	Standard deviation Peak Height signal	0.03829
R108G/K vs G598V	ET	GLRLM: Long Run Low Grey-Level Emphasis in T2-FLAIR signal	0.03883
R108G/K vs G598V	ET	Bin 1 of Peak Height signal	0.03941
R108G/K vs G598V	ET	NGTDM: Contrast in T1Gd signal	0.04009
R108G/K vs G598V	ED	Bin 1 of Fractional Anisotropy signal	0.04024
R108G/K vs G598V	NET	GLCM: Correlation in T2 signal	0.04035
R108G/K vs G598V	ET	Bin 5 of Local Binary Patterns in T2 signal	0.04036
R108G/K vs G598V	NET	GLSZM: Grey-Level Variance in T1 signal	0.0405
R108G/K vs G598V	ED	Bin 3 of Local Binary Patterns in T1 signal	0.04088
R108G/K vs G598V	ED	Relative Enhancement (T1Gd - T1)	0.04092
R108G/K vs G598V	ET	Bin 1 of relative Cerebral Blood Volume signal	0.04275
R108G/K vs G598V	ET	GLRLM: Short Run Low Grey-Level Emphasis in T2-FLAIR signal	0.04353
R108G/K vs G598V	ED	Kurtosis in T1 signal	0.0463
R108G/K vs G598V	ET	Average relative Cerebral Blood Volume signal	0.04654
R108G/K vs G598V	ED	Average T1 signal	0.04721
R108G/K vs G598V	ET	Standard deviation of relative Cerebral Blood Volume signal	0.04806
R108G/K vs G598V	ET	Correlation in Apparent Diffusion Coefficient signal	0.04839
R108G/K vs G598V	NET	Standard deviation of relative Cerebral Blood Volume signal	0.04866

R108G/K vs G598V	NET	Bin 1 of Peak Height signal	0.0493
R108G/K vs G598V	ED	Bin 4 of T2-FLAIR signal	0.04976

Supplementary Table 2: Quantitative Imaging Phenomic features with significant differences between EGFR extracellular domain missense mutants and WT EGFR. ET=enhancing tumor; NET=non-enhancing tumor; ED=peritumoral edematous/invaded region; CTE=complete tumor extent, incorporating all ET, NET, and ED; GLCM=gray-level co-occurrence matrix; GLSZM=gray-level size zone matrix; GLRLM=gray-level run-length matrix; NGTDM=neighborhood grey-tone difference matrix.

EGFR alteration	Tumor sub-region	Feature Observation	*p*- value
R108G/K vs A289D/T/V	NET	higher T1	0.0029
R108G/K vs wt-EGFR	ET	higher Peak Height (measurement extracted from perfusion - DSC-MRI)	0.0276
R108G/K vs wt-EGFR	ED	lower Homogeneity in the Fractional Anisotropy signal	0.0487
A289D/T/V vs wt-EGFR	ED	lower Homogeneity in the Fractional Anisotropy signal	0.0283
R108G/K vs wt-EGFR	NET	higher standard deviation (i.e. more variance) in the Peak Height signal	0.0485
A289D/T/V vs wt-EGFR	NET	higher standard deviation (i.e. more variance) in the Peak Height signal	0.0309
G598V vs wt-EGFR	ET	lower average T1 signal	0.0125
A289D/T/V vs wt-EGFR	ET	lower average T1 signal	0.0081
A289D/T/V vs wt-EGFR	CTE	Major/Minor Axis	0.0149
G598V vs wt-EGFR	ET	higher relative enhancement (T1Gd-T1)	0.0326
A289D/T/V vs wt-EGFR	ET	higher relative enhancement (T1Gd-T1)	0.0374
G598V vs wt-EGFR	ED	higher relative enhancement (T1Gd-T1)	0.0026
A289D/T/V vs wt-EGFR	ED	higher relative enhancement (T1Gd-T1)	0.0441
A289D/T/V vs wt-EGFR	NET	higher relative enhancement (T1Gd-T1)	0.0236
A289D/T/V vs wt-EGFR	CTE	longer Major Axis	0.0064
A289D/T/V vs wt-EGFR	CTE	higher Eccentricity	0.0176

Supplementary Table 3: Select QIP features demonstrating differences between EGFR mutants and WT EGFR. The described feature observations are the ones denoted as statistically significant ($p>0.05$), based on the applied multivariate approach for feature selection (Gaonkar and Davatzikos, 2013) and after selection based on radiographic interpretation. Furthermore, this table denotes the tumor sub-regions in which each of these feature observations were captured, as well as the pairs of EGFR variants that these features were found as statistically significant. Abbreviations: ED=peritumoral edematous/invaded tissue; ET=enhancing part of tumor core; NET=non-enhancing part of tumr core; CTE=complete tumor extent, comprised of all ET, NET, and ED.

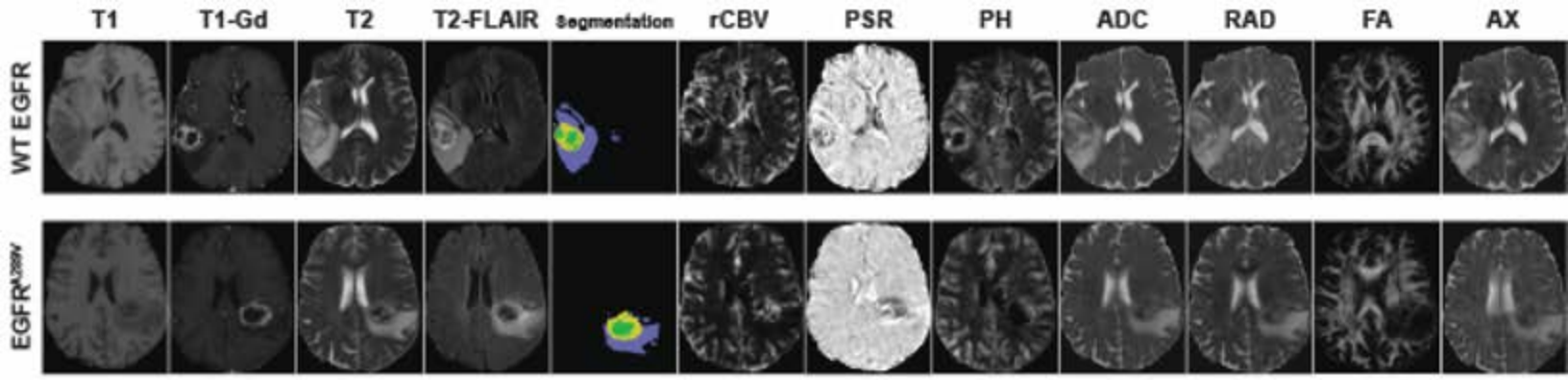

Figure S2. Related to Figure 2. Representative images for the basic and advanced imaging modalities included in the final analyses. Abbreviations: T1Gd=T1 MRI with gadolinium; rCBV=relative cerebral blood volume; PH=peak height; PSR=percentage signal recovery; ADC=apparent diffusion coefficient; RAD=radial diffusivity; FA=fractional anisotropy; AX=axial diffusivity.

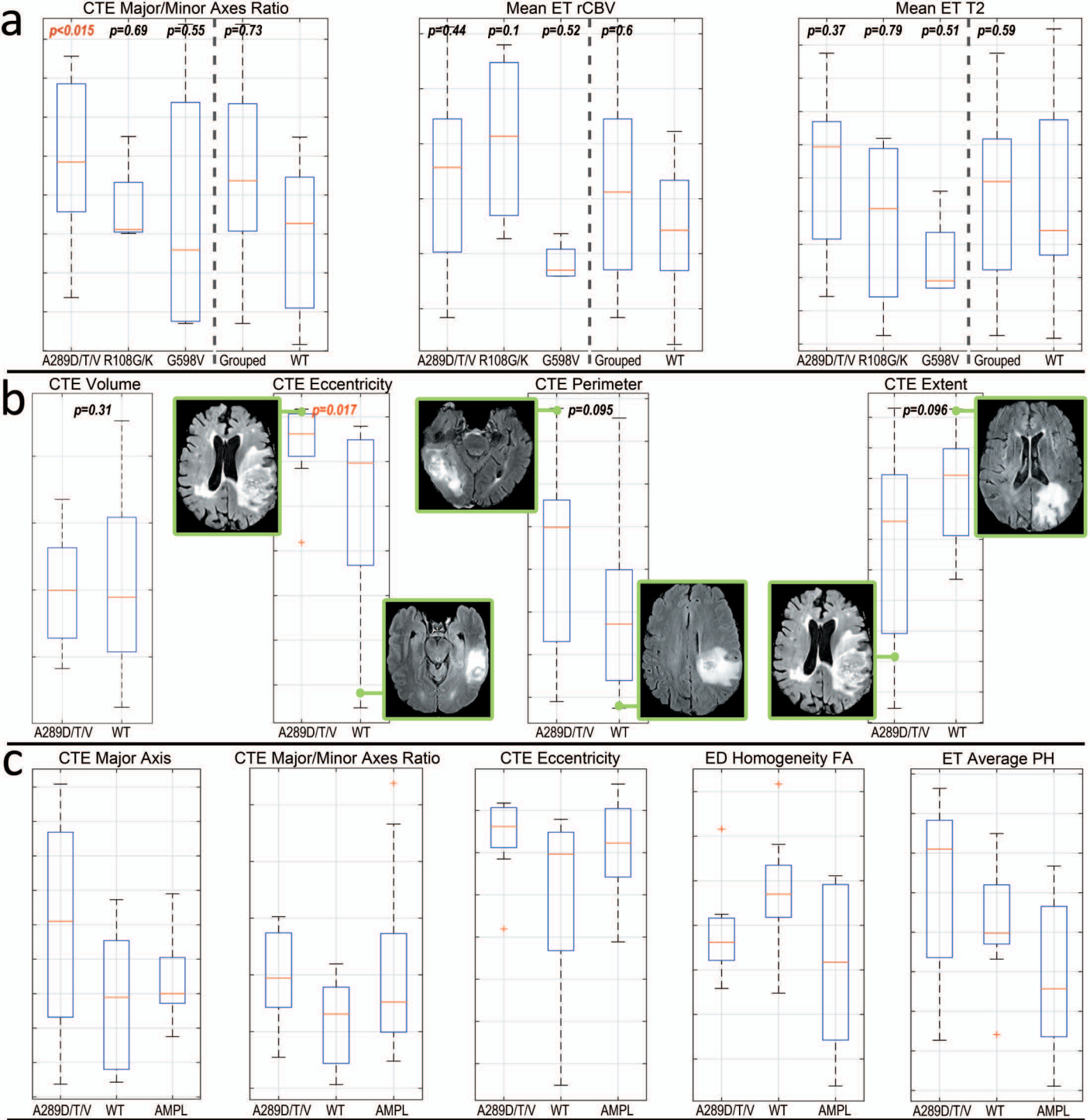

d

	CTE Major Axis	CTE Major/Minor Axes Ratio	CTE Eccentricity	ED Homogeneity FA	ET Average PH
A289D/T/V vs AMPL	0.0844	**0.0086**	**0.0215**	0.3007	**0.0221**
A289D/T/V vs WT	0.7702	0.0605	**0.0375**	**0.0444**	0.1519
WT vs AMPL	0.0669	0.9865	0.4943	**0.0141**	0.0899

Figure S3. Related to Figure 2. (A) Feature comparison across each individual EGFR missense mutation, the grouped mutations, and WT EGFR, for the major: minor axes ratio of the CTE (left), the average rCBV signal in the ET (middle), and the average T2 signal in the ET (right). P-values represent each condition versus WT EGFR. (B) While the volume distribution of the CTE is similar between the $EGFR^{A289D/T/V}$ and the WT EGFR cohorts, the higher eccentricity and perimeter values, combined with lower extent values, in the $EGFR^{A289D/T/V}$ cohort present a picture of more irregularly-shaped tumors, suggestive of more invasive tumors. Insets show representative T2-FLAIR MRI examples of both $EGFR^{A289D/T/V}$ and WT EGFR tumors demonstrating corresponding plotted features. (C) Comparison across $EGFR^{A289D/T/V}$, WT EGFR, and EGFR-amplified patients. $EGFR^{A289D/T/V}$ mutant cases demonstrated distinct distributions from the other two populations, with the exception of the homogeneity in the FA signal of the ED region. (D) Two-sided T test p-values for the features in plotted in (C). Feature definitions: The "Eccentricity" defines the circularity of the assessed shape, i.e. eccentricity value of 0 describes a perfect circle and larger values represent more elongated shapes. The "Perimeter" describes the distance around the boundary of the assessed shape. The "Extent" is the ratio of the area of the assessed shape to the area of its rectangular bounding box. Abbreviations: CTE=complete tumor extent; ET=enhancing tumor; rCBV=relative cerebral blood volume; ED=peritumoral edematous/invaded region; FA=fractional anisotropy; PH=peak height.

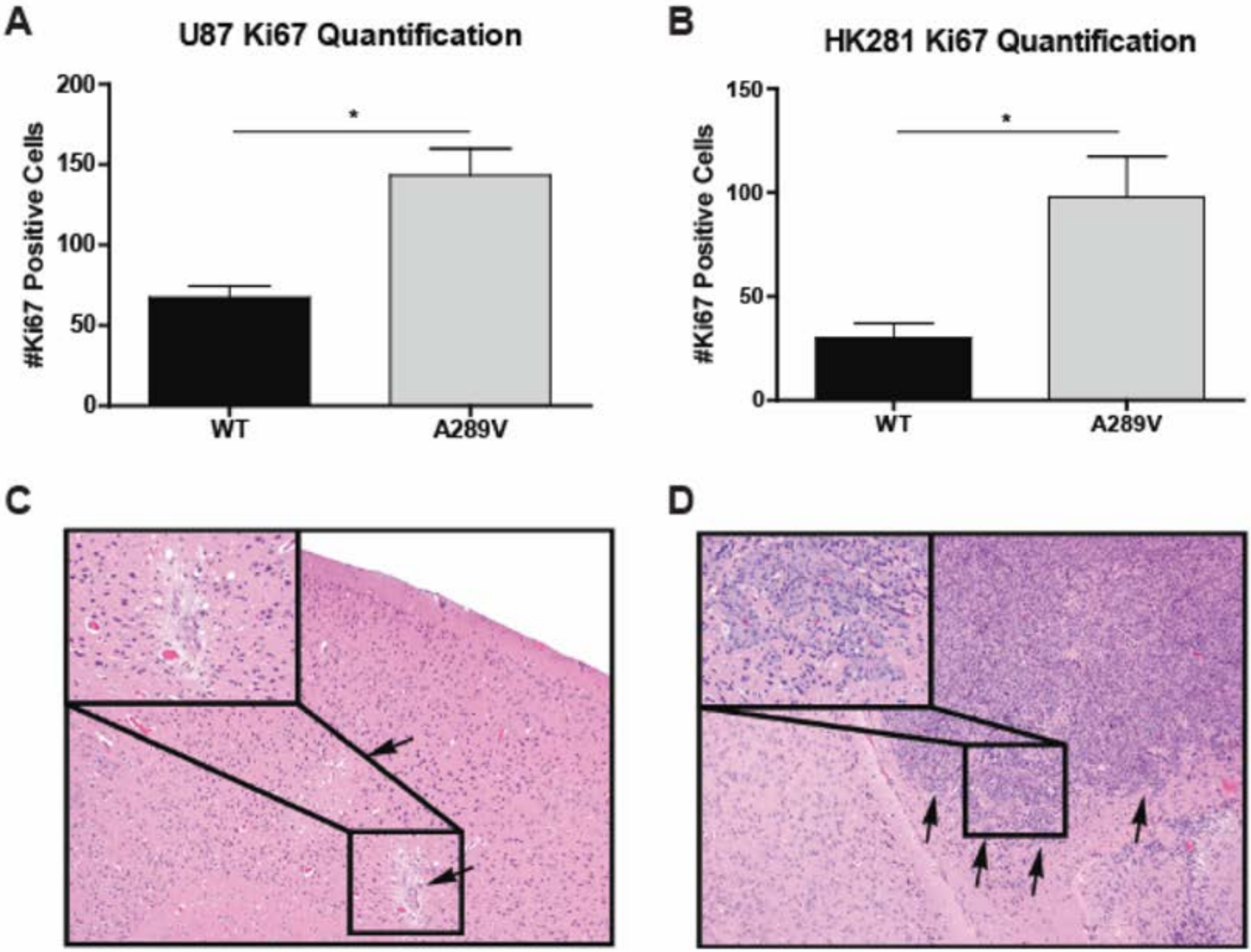

Figure S4. Related to Figure 3. Quantification of Ki67 positive cells from (A) U87 tumors from figure 3B and (B) HK281 tumors from figure 3D. H&E images at Day 14 of animals injected with (C) U87 WT EGFR and (D) U87 EGFRA289V. The WT EGFR demonstrated scar tissue from the needle track and a small focus of tumor cells (arrows and insert). The EGFRA289V missense mutation formed a densely cellular invasive growth effacing and infiltrating unilaterally the frontal cortex (arrows and inset). Magnification 100x, insets 400x.

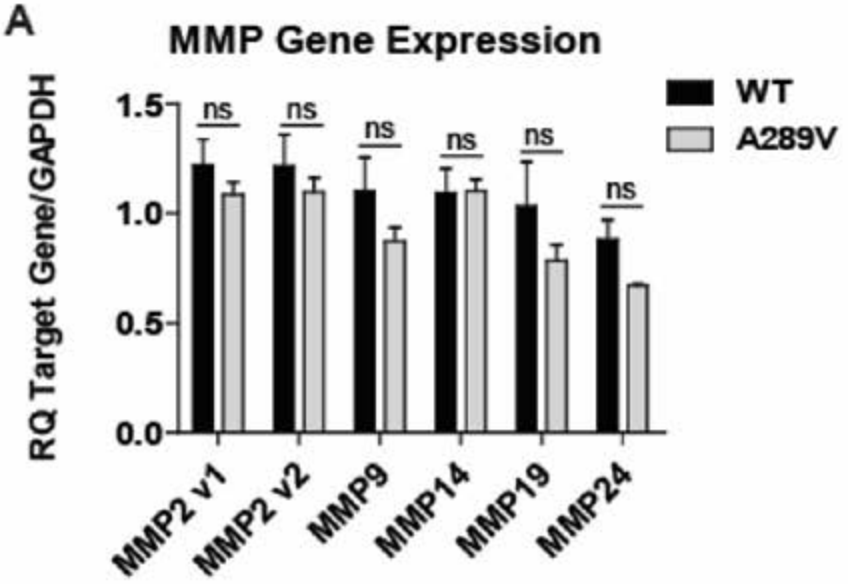

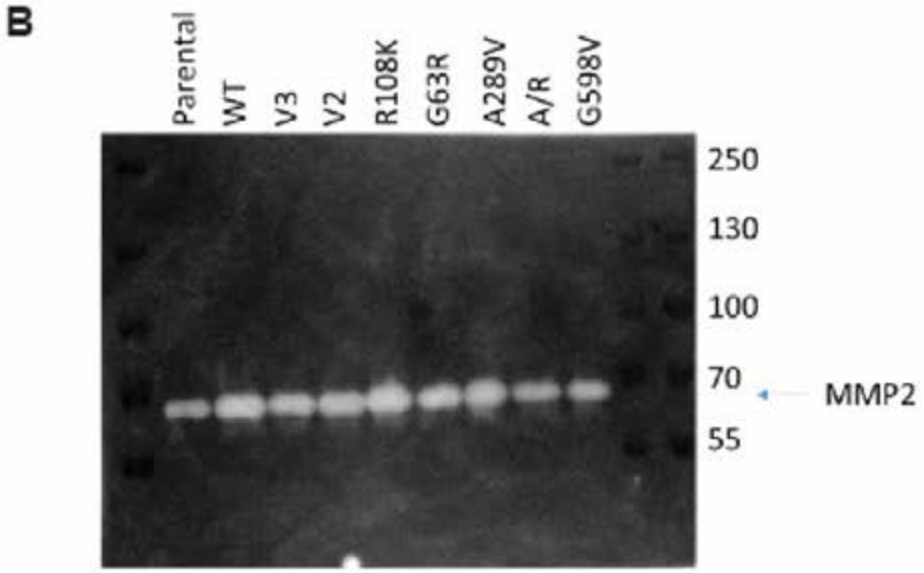

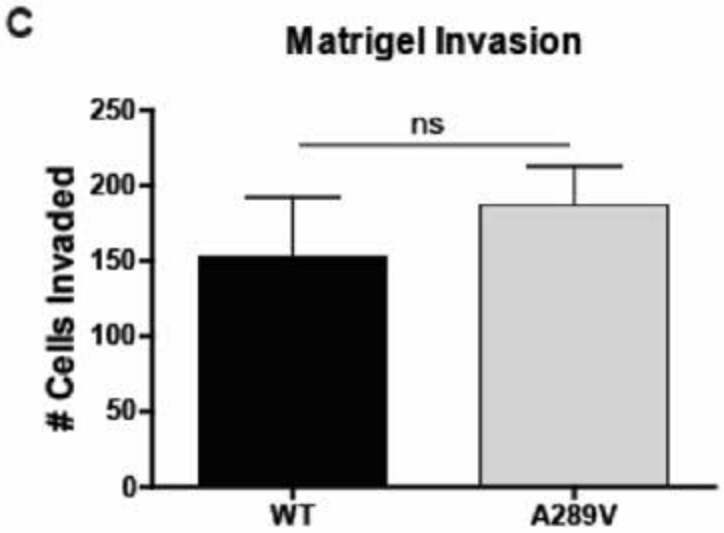

Figure S5. Related to Figure 4. Effect of EGFRA289V on MMP gene expression. (A) Real time quantitative PCR analysis of MMP2, MMP9, MMP14, MMP19, and MMP24 in U87 glioma cells expressing either WT EGFR or EGFRA289V. (B) Gelatin zymogram of concentrated conditioned media from U87 glioma cells expressing the indicated EGFR variant. (C) Quantification of invaded U87 glioma cells was determined using a modified Boyden Transwell chamber assay coated with matrigel. Data shown are fold change gene expression relative to GAPDH. Error bars are standard error of the mean of at least three replicates and represent at least three independent experiments. ns = not significant.

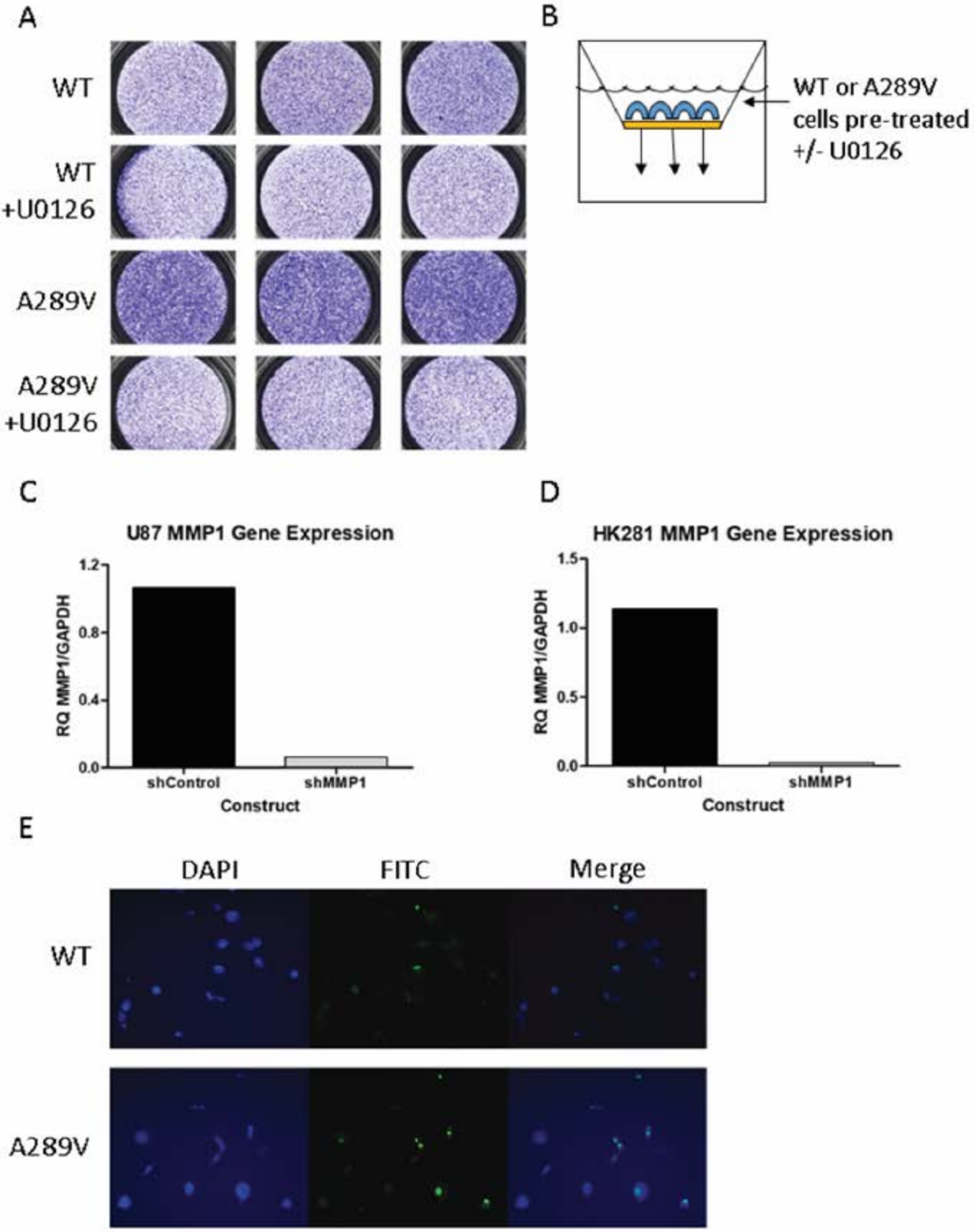

Figure S6. Related to Figure 5. (A) Representative images from Figure 5C showing crystal violet stained HK281 GBM-spheres post-invasion. (B) Schematic of basic experimental set-up using modified Boyden Transwell chambers. Real time quantitative PCR analysis of MMP1 in EGFRA289V expressing (C) U87 glioma cells and (D) HK281 GBM-spheres transduced with shMMP1 or shcontrol. Data shown are fold change gene expression relative to GAPDH. (E) Representative images showing Hoechst and BrdU stained U87 WT EGFR (top) and U87 A289V (bottom) following BrdU incorporation.

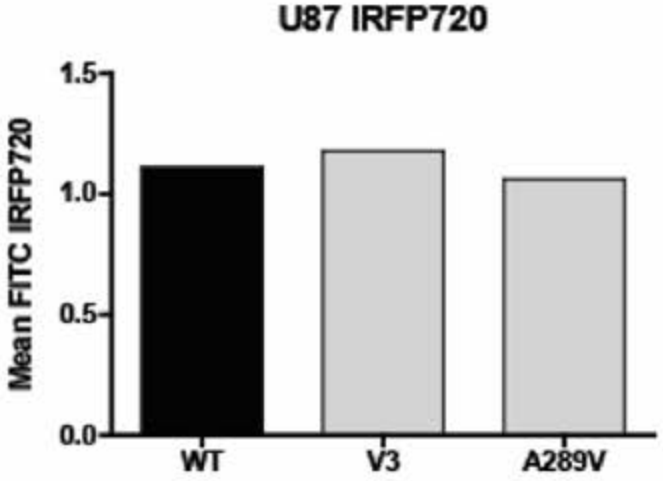

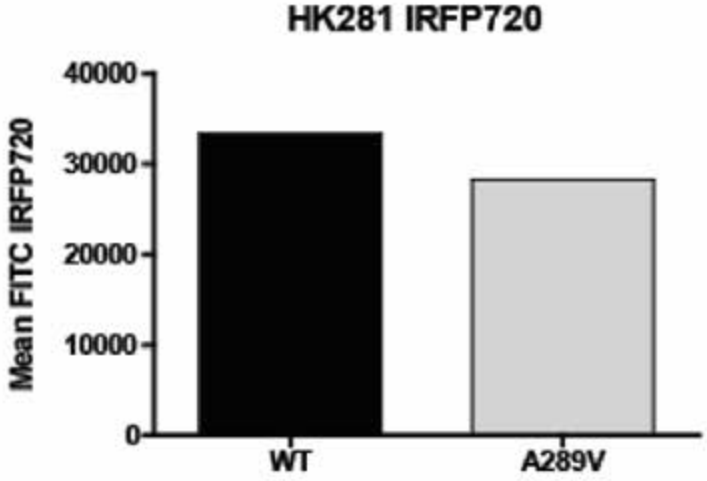

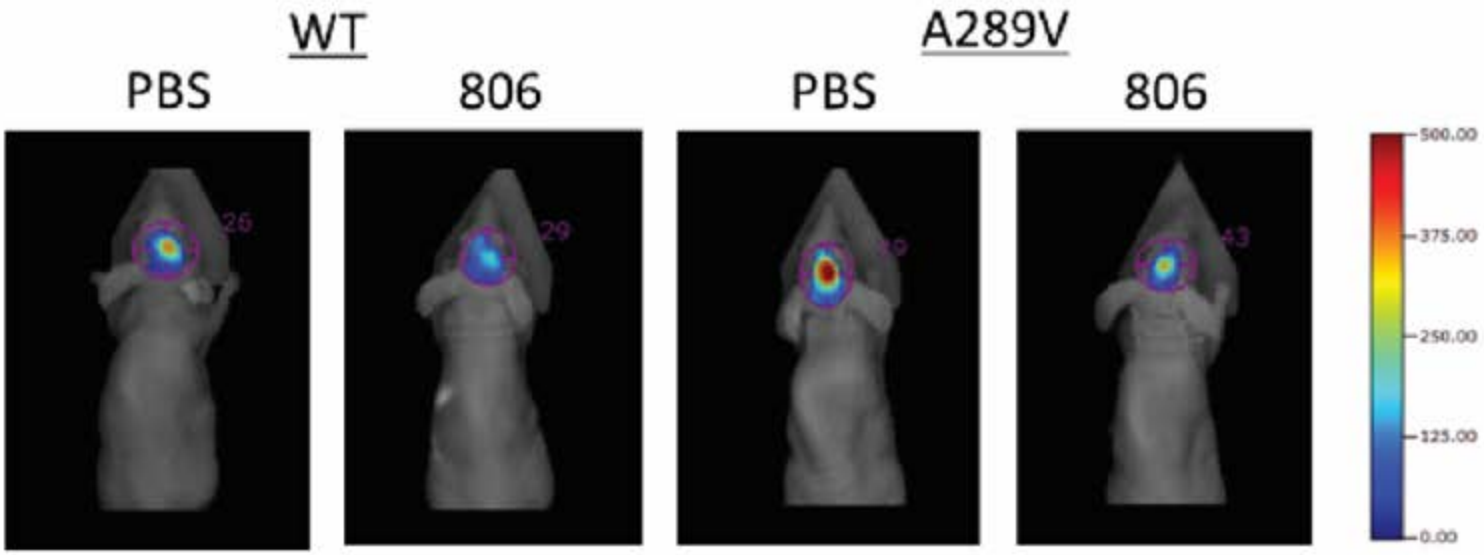

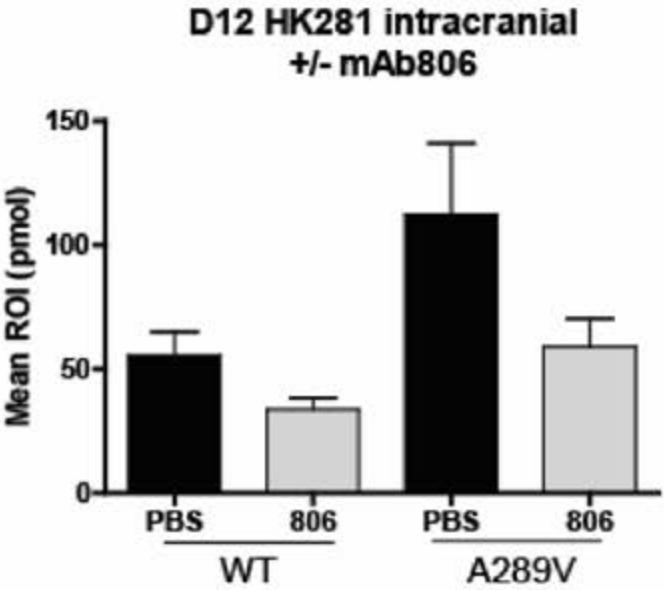

Figure S7. Related to Figure 6. FACS analysis of (A) U87-IRFP720 glioma cells and (B) HK281-IRFP720 GBM-spheres expressing WT EGFR, EGFRvIII, or EGFRA289V. (C) Representative images of HK281-IRFP720-expressing tumors as detected by fluorescence molecular topography (FMT) in Athymic nude mice as described in figure 6. (D) Quantification of FMT signal intensity on day 12 post-implantation for each region of interest.

	Dimensions (pixels)	Spatial Resolution (mm^3)	Slice Spacing (mm)	TI (ms)	TR (ms)
T1	192x256x192	0.976x0.976x1	1	950	1760
T1Gd	192x256x192	0.976x0.976x1	1	950	1760
T2	208x256x64	0.938x0.938x3	3		4680
T2-FLAIR	192x256x64	0.938x0.938x3	3	2500	9420
DSC-MRI	128x128x20	1.72x1.72x3	3		2000
DTI	128x128x40	1.72x1.72x3	3		5000

Supplementary Table 4: Patient MRI specifics.

Primer Name	Forward	Reverse
MMP1	GGTCTCTGAGGGTCAAGCAG	AGTTCATGAGCTGCAACACG
MMP2 v1	GGAGTACTGCAAGTTCCCCT	TCAGTGGTGCAGCTGTCATA
MMP2 v2	GGAGTACTGCAAGTTCCCCT	TCAGTGGTGCAGCTGTCATA
MMP9	GAGACTCTACACCCAGGACG	GAAAGTGGGGAAGACGC
MMP14	GCTGCCTACCGACAAGATTG	TTCATCGCTGCCCATGAATG
MMP19	CAGCCTCGTTGTGGCCTAGA	ACCAGCCTGCACCTCTTGGA
MMP24	GAACCTGTGGGCAAGACCTA	TGACAACCAGAAACTGAGCG
GAPDH	AAATCCCATCACCATCTTCCAGGAGC	CATGGTTCACACCCATGACGAACA

Supplementary Table 5: Real time PCR primer sequences.
Abbreviations: MMP, Matrix Metalloproteinase; GAPDH, glyceraldehyde-3-phosphate dehydrogenase.